Single-Molecule Transistor from Graphene Nanoelectrodes and Novel Functional Materials From Self-assembly

Qizhi Xu

Submitted in partial fulfillment of the

requirements for the degree of

Doctor of Philosophy

in the Graduate School of Arts and Sciences

COLUMBIA UNIVERSITY

2017

ABSTRACT

Single-Molecule Transistor from Graphene Nanoelectrodes and Novel Functional Materials From Self-assembly

Qizhi Xu

This thesis introduces a new strategy to fabricate single molecular transistor by utilizing the covalent chemistry to reconnect the molecule with the electroburnt graphene nanogap. We studied the effect of coupling chemistry and molecular length on the efficiency of reconnection between the molecule and the graphene. With this technique, we are also able to observe the Coulomb Blockade phenomenon, which is a characteristics of single-electron transistors. The high yield and versatility of this approach augur well for creating a new generation of sensors, switches, and other functional devices using graphene contacts. This thesis also introduces a new type of organic single-crystal p-n heterojunction inspired from the ball-and-socket shape-complementarity between fullerene and contorted dibenzotetrathienocoronene (c-DBTTC). We studied the influence of temperature, pressure, and time on the self-assembly process of contorted dibenzotetrathienocoronene on the as-grown fullerene crystals. We also utilized fluorescence microscopy to investigate the charge transfer in this type of p-n heterojunction. Finally, this thesis introduces one-dimensional and two-dimensional programming in solid-state materials from superatom macrocycles. We find that the linkers that bridges the two superatoms determine the distance and electronic coupling between the two superatoms in the macrocycle, which in turn determines the way they self-assembled in the solid-state materials.

The thesis is composed of four chapters. The first chapter introduces why we are in-

terested in molecular transistors and new functional materials, and what has been done so far. The second chapter described the approach we developed to assemble single molecule into circuits with graphene electrodes. The third chapter details the method to fabricate the organic single-crystal C_{60}-DBTTC p-n heterojunction, which is of great importance to understand their charge transfer process. The last chapter introduced a new series of super-atom macrocycles and their self-assembly into solid-state materials with electron acceptor tetracyanoethylene.

This page is intentionally left blank

Contents

List of Figures

List of Tables

Acknowledgement

First, I would like to thank my advisor Porf. Colin Nuckolls, who advised and supported me for the past five years. He is always patient and encouraging to me. Whenever I had questions or came across a problem, he was there to help me. Without his support, this work couldn't be finished. I feel so fortune to conduct my doctoral studies under his supervision. His research insights and entrepreneurial spirit has impacted my view of science and life.

Second, I would like to thank my committee members: Prof. Jonathan Owen, Prof. James Hone, Prof. Kenneth Shepard and Prof. Yuan Yang. I really appreciate them for being my committees and giving me insightful comments.

Third, I would like to thank my collaborators: Prof. Delphine Bouilly, Prof. Philip Kim, Prof. Alexandra Velian, Giovanni Scuri, Dr. Yu Zhong, Dr. Ying Wu. Delphine worked together with me for three years in Nuckolls group and taught me a lot of things, including physics, coding and so on, which is of great importance to my research. Prof. Philip Kim gave us many insightful advices on the molecular transistor project. Alexandra collaborated with me on the superatom project, she is always willing to give me a hand and we had a lot insightful discussions. Yu is a really nice and knowlegdable labmate, we had so many discussions and he taught how to use various techniques. And I also appreciate my other collaborators' hard-work and their helpful advices.

I also would like to thank all the members in Nuckolls group. They make the lab in such a good atmosphere and they are always kind and helpful. Especially, I want to thank my colleagues, who are also my friends, Jaeeun, Boyuan, Yan, Tracy and Tianren. They make my life in Columbia with a lot of fun and I really enjoyed the time spending with them.

I also want to thank my friends in chemistry department: Yihui, Fanghao, Yunyao and so on. We spent a great time together in Columbia and also had a lot of useful academic discussions.

Last but not least, I want to thank my family and my boyfriend Wenjie. They are so supportive to me and try their best to help me. My brother is my role model in my life and he is always there to help me whenever I need. Besides, he gave me a great many advices on physics and mathematics. Wenjie also provided me with a lot of help in coding, which saved me so much time on dealing with the experiment data. Their love is also my motivation to go forward.

For my family.

Chapter 1

Introduction

1.1 Motivation

The Moore's law [1], which was brought up by Moore in 1965, has dominated the advancement of semiconductor industry since then. It states that the number of transistors on a integrated circuit will double every two years or so. As can be seen in Figure 1.1, the number of transistors on a microprocessor chip produced by Intel has followed this trend for decades, which is mainly due to scaling down the transistors on the integrated circuits.[2] The exponential advancement of the semiconductor industry leads to the miniaturization of electronic devices, such as computers and smartphones, which contributes a lot to the economic growth in the last few decades and makes our life more convenient and intelligent. However, the pace of advancement of microprocessor chips slowed down and finally was announced to be at its end last year despite great efforts made by researchers. This is because the dimension of the transistor is approaching the limit of the silicon complementary metal-oxide-semiconductor

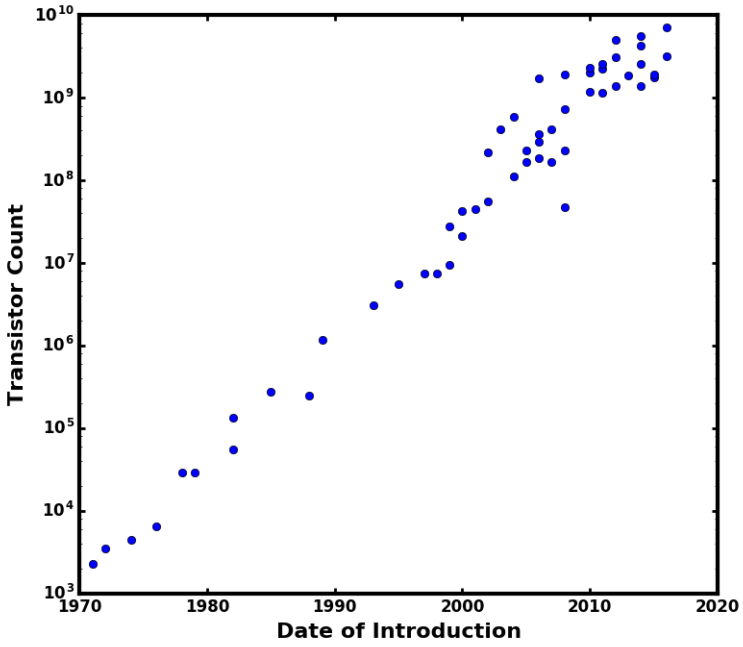

Figure 1.1: Transistor number on a microprocessor chip produced by Intel versus the year introduced.

(CMOS) and other issues, such as the heat problem, came up as the dimension decreases.[2]

In order to continue scaling down the transistor and maintain the huge semiconductor market, three strategies have been brought up by researchers: More Moore, More than Moore and Beyond CMOS. More Moore is defined as an attempt to further develop advanced CMOS technology and reduce the associated cost by exploiting new design or incorporating new materials in the circuits, such as gate-all-around structure, indium antimonide (InSb)[3–5] and indium gallium arsenide (InGaAs)[6]. However, despite vigorous devotion by researchers, there exists a size limit of 2-3 nm in this circuits, in which there are about ten atom across, At this small scale, the device is no longer reliable. Moreover, the transistors would suffer

from the problem of heating effects and high cost. As a consequence, the strategy More than Moore, which emphasizes the functionality and the applications of electronics, drew more and more attention. A great many studies has been conducted to incorporate new functional components in the electronics, such as sensors[7–11], radio frequency devices[12–15], flexible display [16–20] and bio-chips[9, 21–25]. Beyond CMOS proposed a alternative way to design logic circuits, such as tunneling junction devices[26–28], spin-based electronics[29–32] and molecular electronics[33–36], which is thought to be able to replace silicon CMOS technology.

1.2 Single-molecule transistor

As mentioned previously, molecular electronics has long been considered to be the fundamental building blocks of the ultimate mininaturization circuits[34, 37, 38], because single molecules are the smallest chemical stable structures. It possess the merits of small size, high speed, self-assembly and easy-functionality. Due to the nanoscale size of single molecules, the physical properties of the molecular electronics falls in a regime where quantum mechanics effects dominates. As a consequence, it's of great importance to investigate how the electron transport in single-molecule transistors, which is the basic structure going to be discussed in the next chapter. Fortunately, a great many studies of single-molecule electronics has been done, such as graphene quantum dots[39], carbon nanotubes[40], small conjugated molecules[41–43]. Generally speaking, the electron transport through the molecule junction can be categorized into two different processes depending on the coupling strength between electrodes and the molecule.[44] When the molecule is strongly coupling to electrodes, the transport occurs through direct tunneling process in which the electron transport elastically

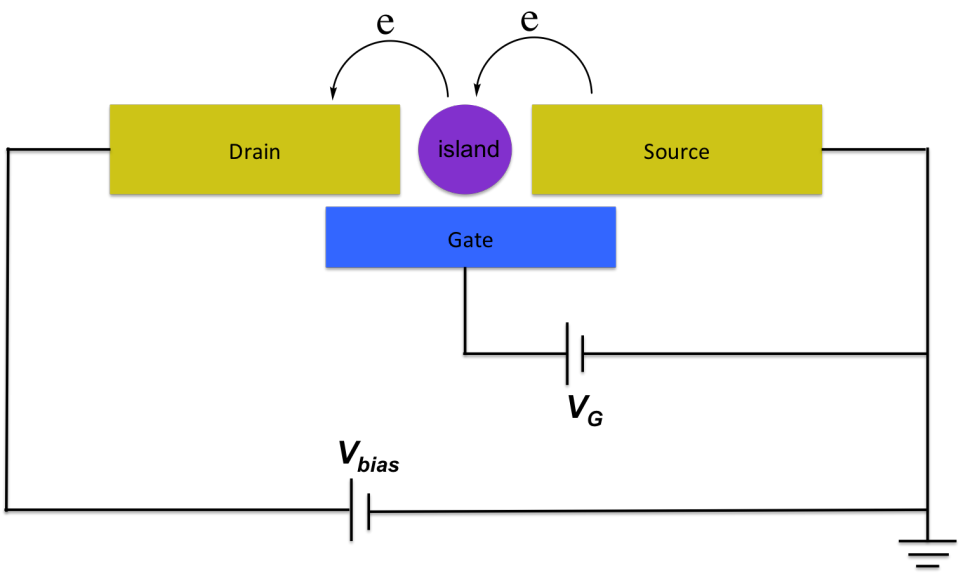

Figure 1.2: The single-electron transistor is composed of three terminals: source, drain and gate. The island is weakly coupled to the source and drain electrodes; and capacitively coupled to the gate electrode. The electron tunnels from the source electrode to the island and then to the drain electrode. The gate electrode can control the electron transport by tuning the energy alignment.

through the junction. In contrast, when the coupling between the molecule and electrodes is weak, the transport of electron in the junction is governed by the single-electron tunneling process, which would result in Coulomb Blockade phenomena. When a gate electrode is added to the system, it could further control the transport of electrons in the system. And this kind of transistor is also known as the single-electron transistor (SET).

Figure 1.2 showed the schematic of a single-electron transistor with the island representing the conducting molecule. There are three terminals in the transistor: drain, source and gate. The source and drain electrodes are weakly coupled to the island and gate electrode

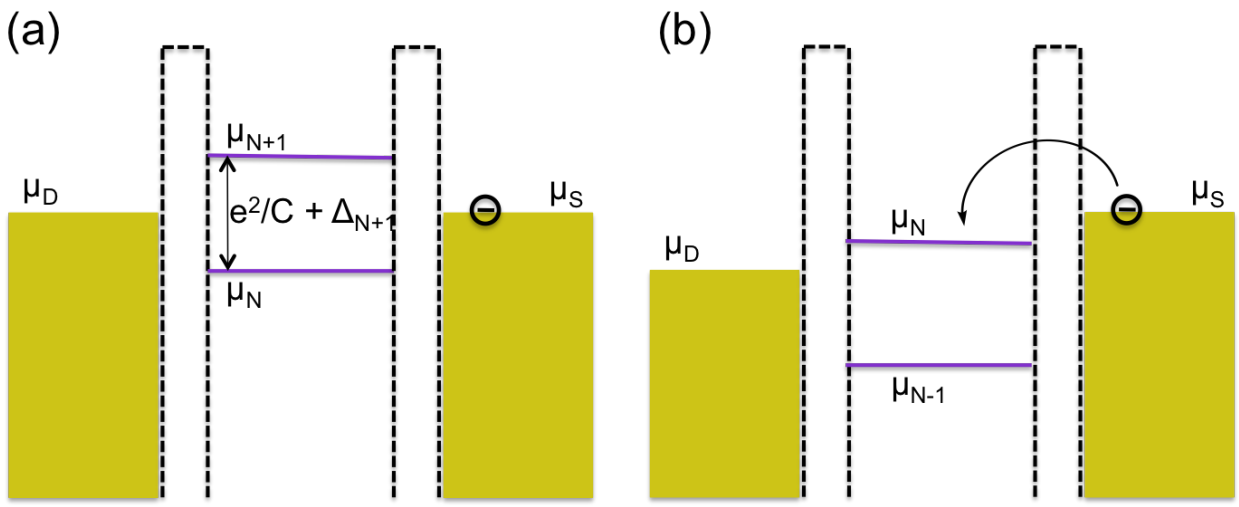

Figure 1.3: (a) The chemical potential of the island lies outside that of source and drain. No electron can tunnel through the island. (b) The chemical potential of the island lies within that of source and drain. The electron can tunnel through the island.

is capacitively coupled with the island. When one electron tunnels through the barrier from the source electrode to the island, the associated energy change of the island is

$$E_c = e^2/C$$

where: e is the charge of one electron, C is the Capacitance of the island.

This energy change of the island is defined as the charging energy. In order to observe the single-electron tunneling effect, the temperature need to be low enough that it satisfies the condition $e^2/C >> k_B T$. The chemical potential spacing of the island with N and N+1 electron is given by

$$\Delta\mu_{N+1} = e^2/C + \Delta_{N+1}$$

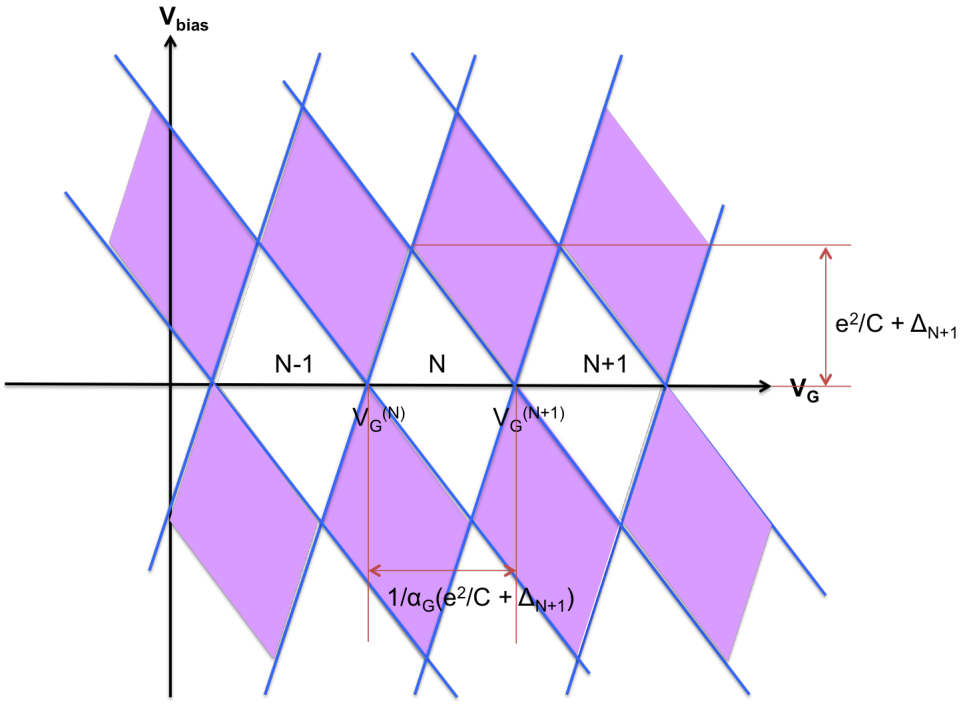

Figure 1.4: The current is blocked inside the white diamond shaped regions. Single electron tunnels in the purple diamond regions. The addition energy E_{add} can be obtained by extracting the height of the diamond. And the difference of the neighboring white diamonds touch points is $\Delta V_G^{(N+1)} = \frac{1}{e\alpha_G} E_{add}$)

where: $\Delta_{N+1} = \epsilon_{N+1} - \epsilon_N$ is the energy spacing of the island.

By varying the voltage of the gate electrode, the chemical potential of the island can be tuned(see Figure 1.3). When the chemical potential of the island lies within the electro chemical potential of source/drain electrodes, the electron can tunnel through the island(see Figure 1.3b). Otherwise, the tunneling of the electron is not allowed(see Figure 1.3a).

The current-voltage plot as a function of the gate voltage is characterized with Coulomb

diamonds (see Figure 1.4), which is multiple, parallel diagonal interfaces defining diamond-shaped regions. The diamond region corresponds to the situation where the electron is blocked. From the graph, the addition energy $E_{add} = \Delta\mu_{N+1} = \Delta_{N+1} + e^2/C$ can be obtained by extracting the height of the diamond, i.e. the energy separation between $V_{bias} = 0$ and the top (or bottom) of the diamond. And the difference of adjacent diamond touching point in the V_G axis is given by $\Delta V_G^{(N+1)} = \frac{1}{e\alpha_G}(\Delta_{N+1} + e^2/C)$, where α_G is the gate coupling parameter.

Since the size of the molecule is in the nanoscale, special techniques are needed to place single molecule between the electrodes. So far, a few techniques has been developed to construct the electrode-molecule-electrode junction. The first technique used widely is the scanning tunneling microscope (STM) breakjunction (see Figure 1.5a).[47–49] The gold tip of the STM immersed in the target molecule solution is pulled away from the substrate and a gold-molecule-gold junction forms in the closed circuit. The conductance of the molecule thus could be obtained by repeating this process by thousands of times. The second technique is the conducting probe atomic force microscope (AFM) (see Fig 1.5b).[50, 51] The conductance of the molecule can be calculated by obtaining the tunnel current between the tip and the self-assembled molecules on the substrate. Even though these two techniques are able to obtain statistic data in a short time, they suffered from the shortcoming of transient nature and lacking gate electrode, which prevents their application in the solid-state electronics. The third technique is the mechanically controllable break-junction (see Fig 1.5c).[52] The metal wire on the flexible substrate is elongated until break by increasing the bend of the substrate. The fourth technique is the angle evaporation technique (see Fig 1.5d)[41, 45], in which the metal electrodes separated by few nanometers can be fabricated when the

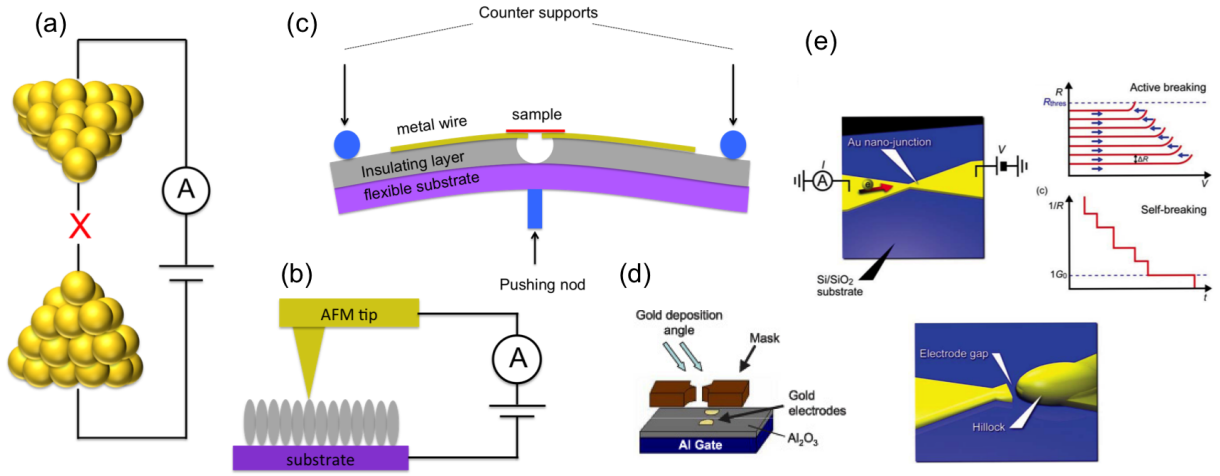

Figure 1.5: (a) STM-breakjunction, the break junction is created by pulling the gold STM tip away from the gold substrate. (b) Conducting probe AFM, conducting AFM tip scans the substrate with self-assembled molecules. (c) Mechanically controllable breakjunction, gaps form when the metal wire on the flexible substrate is elongated until break by increasing the bend of the substrate. (d) Angle evaporation technique , the electrodes separated with few nanometers are deposited via angle evaporation with a shadow mask. [45] (e) Electromigration method, the gap forms in a metal wire under a feed-back controlled voltage ramp process. [46]

tilt angle evaporation is exploited with a shadow mask. The last technique is the electromigration method (see Fig 1.5e).[46, 53] Small gaps form due to the migration of atoms when a controllable bias voltage is applied. Due to the stability of the electromigration method, it has been widely used to build up solid-state molecular electronics.

The electrode material is another important factor needed to be considered in constituting the molecular electronics because it determines the efficiency and reproducibility.[58] The noble metal, such as gold, were exploited widely in the techniques discussed above due to their noble properties. However, high mobility of gold makes it unstable at ambient temperature.[59] In contrast, the carbon materials, such as the carbon nanotubes (CNTs) [55, 57] and graphene [54, 56, 60–62], give higher stability and have been exploited as the electrodes to constitute three-terminal transistors. Besides, the molecule can anchor to the carbon material based electrodes through multiple ways, such as covalent chemistry [54, 55, 57, 61] and π-π interaction [56, 60, 62]. Moreover, this nanoscale carbon electrodes could also reduce the screening effect of the gate electrode.

The carbon materials based electrodes can be fabricated with a top down strategy, in which the nanogap can be created by reactive ion etching within e-beam defined window (see Figure 1.6 a and b) [54, 55, 61] or through a feedback-controlled electric breakdown process (see Figure 1.6c) [56, 60, 62]. The molecular electronics with carbon nanotubes as electrode have also been fabricated with a bottom-up method, in which carbon nanotube electrodes were covalently attached to the molecule in the solution and then transferred onto the substrate for subsequent electrical studies (see Figure 1.6d) [57]. Compared with the e-beam lithography based process, the nanogap fabricated with the feedback-controlled electroburning technique has the advantage of higher reproducibility and smaller size. As

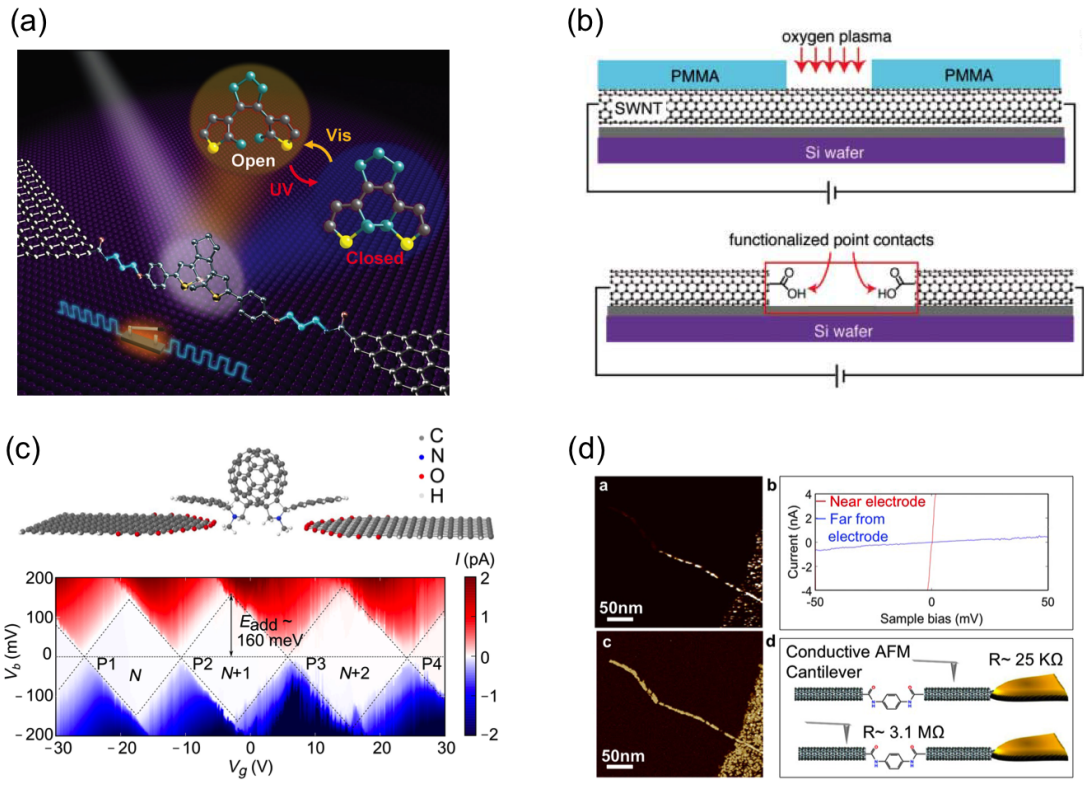

Figure 1.6: (a) Graphene point contacts formed by oxygen plasma etching with standard e-beam lithography process [54] (b) Carbon nanotube electrodes formed by oxygen plasma etching with standard e-beam lithography process [55] (c) Graphene nanoelectrodes fabricated with feedback-controlled electric breakdown method [56] (d) CNT/molecule/CNT junctions formed through solution-processable self-assembly [57]

a consequence, the single-molecule transistor discussed in the next chapter exploits the graphene nanogap created with feedback-controlled electroburning as the electrodes.

As mention previously, the size of the gap between the fabricated electrode is of great importance because molecules couldn't fit in if the separation of electrodes is too large. However, the nanogap size is too small that it couldn't be resolved in direct imaging techniques, such as AFM [60, 63]. In order to obtain the gap size of the as-fabricated graphene electrodes, Simmons model [64] has been exploited to estimate the gap size. Simmons model assumes that electrons transport only through tunneling between two similar electrodes separated by a thin insulating layer. The insulating layer is considered to be a rectangular barrier with height ϕ_0. When bias voltage applied is in a intermediate range, the current density between the electrodes is given by the following equation:

$$J = (\frac{e}{2\pi h d^2})[(\phi_0 - \frac{eV}{2})[-\frac{4\pi d}{h}(2m)^{\frac{1}{2}}(\phi_0 - \frac{eV}{2})^{\frac{1}{2}}] - (\phi_0 + \frac{eV}{2})[-\frac{4\pi d}{h}(2m)^{\frac{1}{2}}(\phi_0 + \frac{eV}{2})^{\frac{1}{2}}]]$$

where: e - charge of electron; m - mass of electron; h - Planck's constant; d - gap size
From the equation, we noticed that the dependence of the current density on bias voltage is determined by the barrier height ϕ_0 and the gap size d. As a consequence, considering the cross-section area as a prefactor, the gap size could be estimated by fitting the obtained curve of current as a function of bias voltage.

1.3 Organic semiconducting molecules

In the past two decades, a great variety of researches have been focusing on organic electronics because they possess several advantages. [65, 66] Firstly, new functionality can be

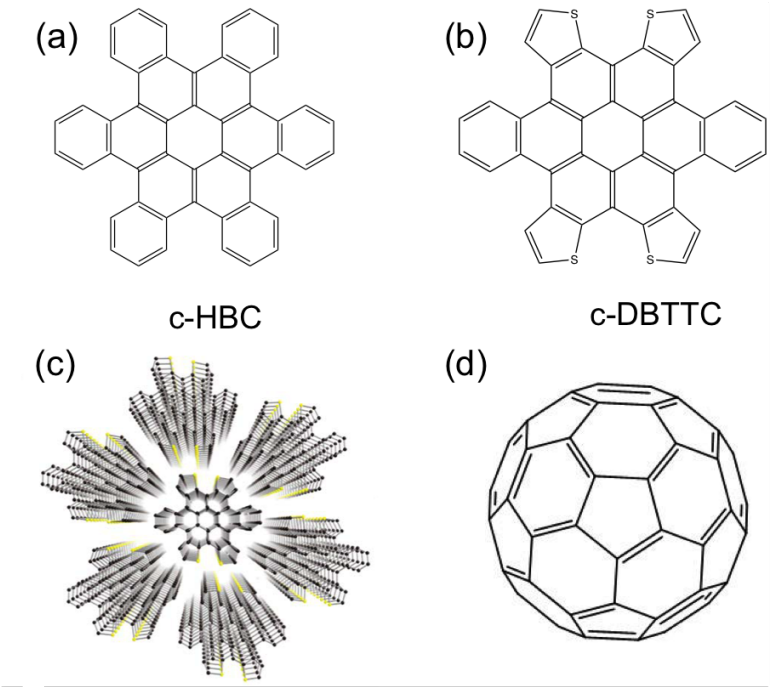

Figure 1.7: (a) contorted hexabenzocoronene (c-HBC) (b) contorted dibenzotetrathienocoronene (c-DBTTC) (c) Hexagonal columnar packing of c-DBTTC crystal grown from horizontal vapor phase transport [76] (d) fullerene

incorporated into the electronics due to the versatility of molecule design. Besides, organic electronics have the merit of flexibility, which allows the production of flexible electronics. Moreover, the fabrication process of organic electronics is simple and low-cost, such as inkjet printing [67]. Up to now, organic electronics with diverse functionality has been fabricated, including solar cells [68, 69], radio-frequency devices [70–72], sensor [73], transistors [74, 75], organic light-emitting devices (OLEDs) [16, 17].

Due to the devotion of many researchers, numerous molecules have been synthesized and constitute the immense library of organic semiconducting materials. [66] They are usu-

ally classified into two categories by their molecular weight: polymers and small molecules. Compared with polymers, small molecules are usually easier to purify and form crystalline film, which in turn results better performance in devices. Depending on the type of charged carriers, the organic semiconductors are classified as p-type or n-type. It's easier for hole injecting than electron injecting for p-type semiconductors, so they are also known as hole transport. Common p-type small molecules includes acenes, coronene, oligoacenes and their derivatives. [66] Hexabenzocoronene (HBC) (see Fig 1.7a) and their derivatives, as a kind of coronene, has drawn great attention due to their unique disk-shaped structures. [77] As a consequence, they tends to form two-dimensional column structures via π-π interaction between molecules. For example, contorted dibenzotetrathienocoronenes (c-DBTTC) (see Fig 1.7b) is a tetrathiophene-fused version of contorted HBC (c-HBC) and it displays hexagonal columnar arrangement after crystalizing (see Fig 1.7c). [76] Similarly, n-type semiconductors transport electrons in the devices, including fullerene (see Fig 1.7d) [78, 79] and its derivatives, perylene diimides [68, 75] and so on. As one of the earliest organic materials been studied, fullerene presents high electron mobility and single crystals of fullerene with different packings and morphologies can be synthesized easily.[79, 80]

P-n heterojunctions, as the elementary building blocks of semiconductor electronic devices, forms at the interface between p-type and n-type semiconducting materials. A large variety of optoelectronics based on p-n heterojunctions has been fabricated, such as LEDs [82, 83] and solar cells [68, 69]. Whether the p-n heterojunction forms good connection plays an important role in the performance of the opoelectronics.[84] According to previous studies in HBC/C_{60} interfaces, the shape-complementarity of this p-type/n-type heterojunctions has a great effect on their electronic coupling and charge transfer rate.[81] As shown in Fig 1.8,

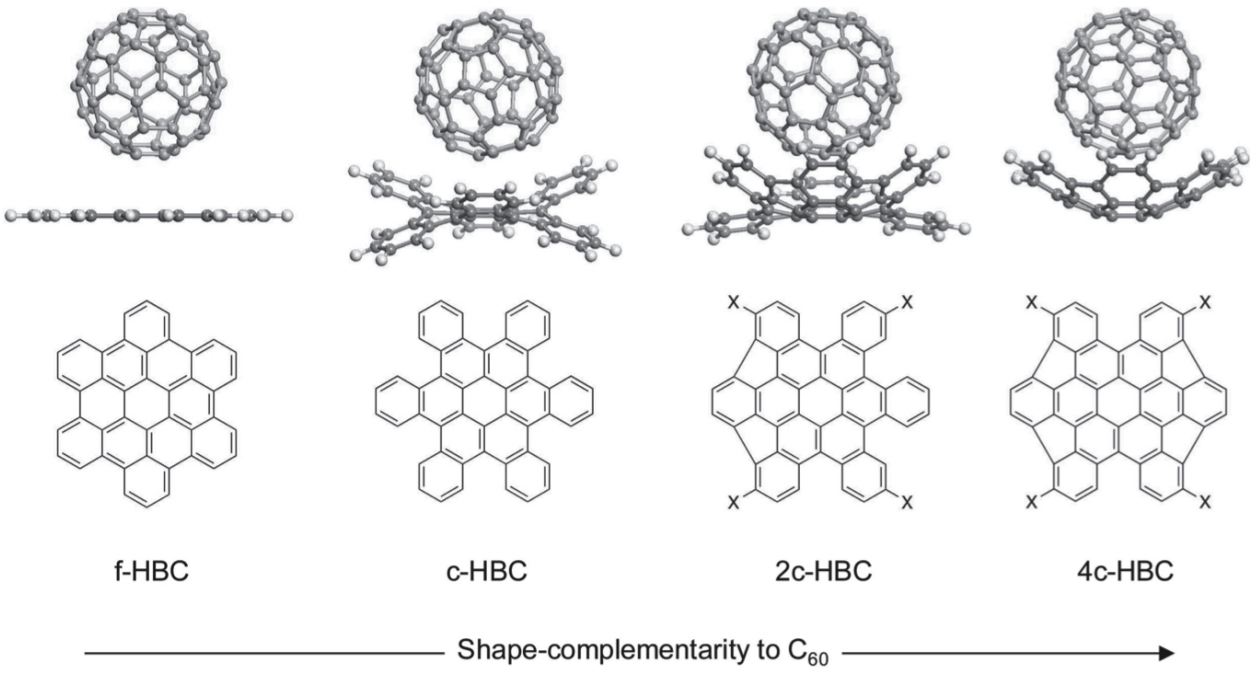

Figure 1.8: Chemical structures (bottom) of HBC molecules with varying degrees of contortion and their shape-matching to fullerene (top). [81]

the degree of shape-complementarity increases as the contortion of the molecule increases, which promotes their self-assembly and charge transfer.

1.4 Nanoscale building blocks: superatom

Nanoscale molecular clusters, which is also known as superatoms, have been exploited as fundamental building blocks for various solid-state functional materials [85–92] and drawn great attentions due to several advantages. Firstly, molecular clusters with discrete, well-

defined structure could be prepared independently with high atomic precision. Besides, the properties and functionality of individual clusters can be easily tuned through molecule design. Moreover, the three-dimensional solids assembled from molecular clusters exhibit excellent electronic, thermoelectric and phononic properties, which attributes to collective properties of individual building blocks.[93] Consequently, the composition design of the superatoms and how to assemble these nanoscale building blocks into novel materials with multi-functionality have been the focus of reseachers. [90] So far, several strategies have been used to assemble superatoms into three-dimensional materials, such as electrostatic interaction [88], hydrogen bonding and shape-complementarity [91].

As one of the electron rich clusters, $Co_6Se_8(PEt_3)_6$ (Figure 1.9A) and its derivatives, have been widely used as the atomic component and incorporated into functional solid-state materials with different strategies. As shown in Figure 1.9B, $[Co_6Se_8(PEt_3)_6][C_{60}]_2$ solid with the CdI_2 structure type could be formed via electrostatic interaction after the electron transfer from the cluster to the electron acceptor fullerene. [88] The as-synthesized solid presents collective electric properties and magnetic ordering, compared with superlattices made from nanocrystals. Van der Waals material through self-assembly from fullerene and $Co_6Se_8(PEt_2phen)_6$, which is shape-complementary to the fullerene, were also reported (See Figure 1.9C). [91] This unique material could even be mechanically exfoliated into sheets, like traditional van der Waals materials, which are potential alternative channel materials for next-generation electronics. In addition, the $Co_6Se_8(PEt_3)_6$ cluster could further being used to synthesize simple molecules, like diatomic and linear triatomic molecules by programming the ligand of the cluster (See Figure 1.10). [94]

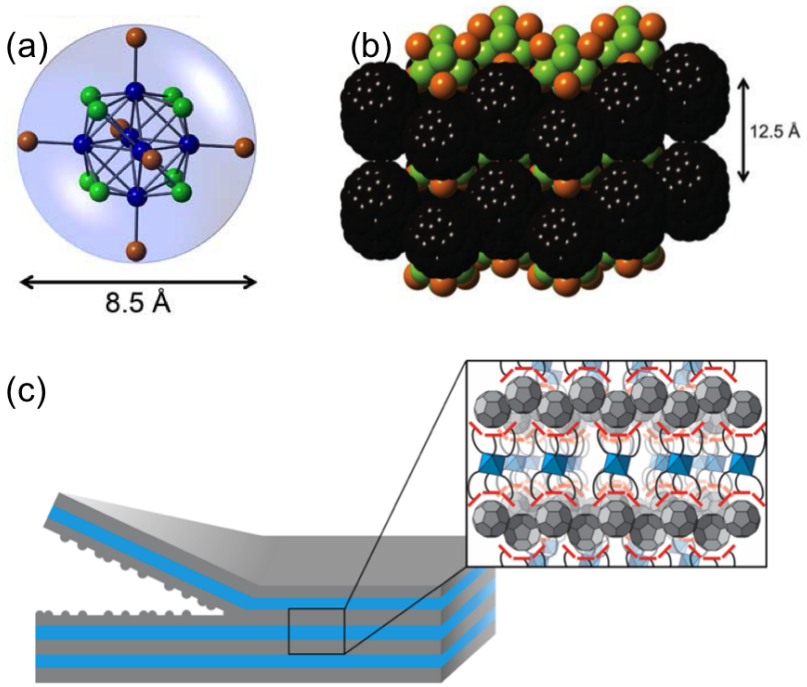

Figure 1.9: (a) Structures of $Co_6Se_8(PEt_3)_6$ cluster [88] (b) Crystal packing of $[Co_6Se_8(PEt_3)_6][C_{60}]_2$ [88] (c) Van der Waals materials made from $Co_6Se_8(PEt_2phen)_6$ and C_{60} [91]

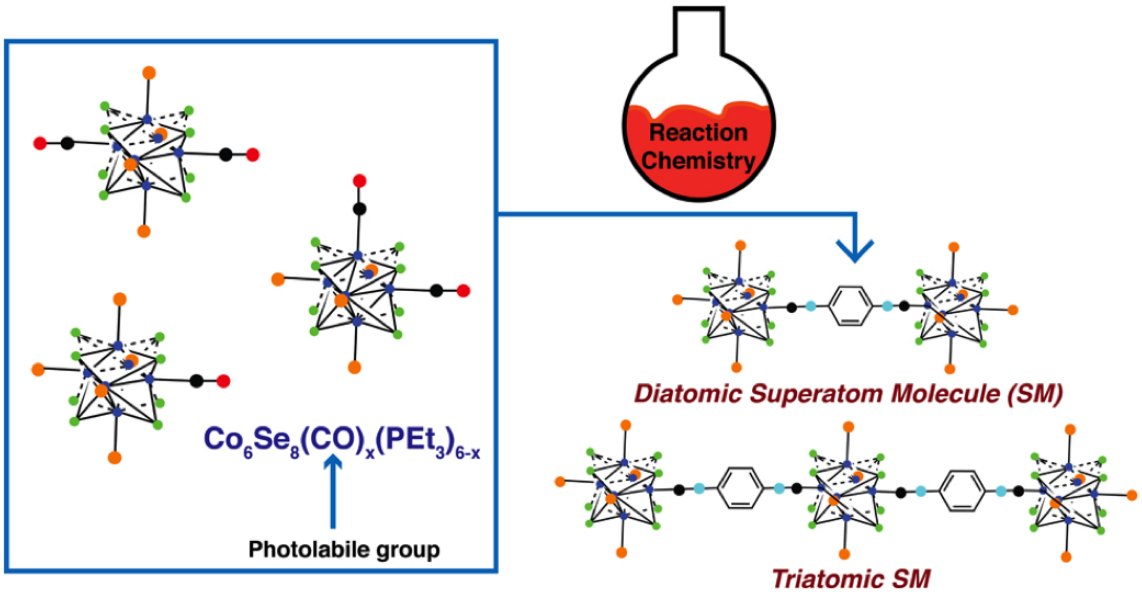

Figure 1.10: Schematics showing the synthesis of diatomic and triatomic superatom molecules from $Co_6Se_8(PEt_3)_6$ [94]

1.5 Outline

In the second chapter, I'm going to present a single molecular transistor fabricated through covalent chemistry to graphene nanoelectrodes. In the third chapter, I'll discuss the single-crystal p-n heterojunction inspired by the ball-and-socket interface between fullerene and contorted dibenzotetrathienocoronenes. In the fourth chapter, I want to introduce a new series of solid-state materials self-assembled from $Co_6Se_8(PEt_3)_6$ superatom.

Chapter 2

Single Electron Transistor with Single Aromatic Ring Molecule Covalently Connected in Graphene Nanogaps[1]

2.1 Introduction

This chapter describes a robust platform to create graphene nanogap electrodes and bridge them covalently with individual molecules. Molecules have long been considered as fundamental building blocks for the assembly of ultraminiaturized electronic circuits[33, 34, 37, 44, 95, 96]. Molecular electronics has the capacity to harness the immense library of chemical reactions and molecular structures to target functionality, such as sensors, emitters and switches[34, 37, 54, 97–99]. A major issue limiting the development of molecular

[1]This chapter is based on a work submitted Nano Letters.

electronic circuits is in their fabrication, as it remains a challenge to accurately position and connect individual molecules in solid-state, electrical architectures. Single-molecule electrical circuits have been obtained using break junctions[48, 100], allowing statistically-robust measurements of molecular conductance. However, the transient nature of these junctions limits their applicability in complex architectures and sensors. Other approaches have been used to connect individual molecules between nanoscale-separated leads in solid-state devices, including gold leads made from electromigration[53, 101–103] and carbon nanotube or graphene leads etched by reactive ion etching[55, 61, 104–108] or sputtering[109]. However, the size resolution and reproducibility of the fabricated nanogaps have remained challenging, leading to low yields in forming molecularly-reconnected devices. Recently, a method was introduced to fabricate extremely small gaps in graphene devices using feedback-controlled electroburning[110–112] and this method was used to assemble single-molecule transistors with non-covalent attachment to the bridging molecules longer than 1 nm[56, 60, 62, 113–115].

Here, we use reaction chemistry to purposely attach individual conductive molecules to the oxidized edges of electroburnt graphene nanogaps. The shape and size of the graphene nanogaps, combined with optimized reaction chemistry on the graphene edges, enables exceptionally high connection yields for ultrashort molecular bridges (up to 40%). It allows extremely short molecules (as short as 0.6 nm in length) to be chemically connected into the electrical circuit, as demonstrated by the successful reconnection with 1,4-diaminobenzene (1Ph) and 4,4'-diaminobiphenyl (2Ph) molecules. We monitor the reconnection by an increased conductance across the nanogap accompanied by gate-dependent single-electron tunneling features. Using this robust covalent connection platform, we are able to show that

the yield of reconnection is dependent on the nature of the molecule and can be optimized by varying the reaction conditions for the coupling chemistry. This approach provides a powerful platform to build stable single-molecule transistors from targeted graphene-edge reaction chemistry.

2.2 Formation and covalent reconnection of graphene nanogaps

We fabricate single-molecule transistors following three successive steps: (1) fabrication of graphene transistors, (2) electroburning of graphene channels and (3) reaction chemistry for molecular reconnection. We first fabricate graphene devices from few-layer exfoliated graphene flakes in a two-terminal configuration, with top-contact source and drain electrodes, which were micro-fabricated using standard lithography and metal evaporation techniques. We use a degenerately-doped silicon substrate as a common back gate, which was isolated from the graphene channel with a 285-nm layer of thermal silicon dioxide (see details on device fabrication in the Experimental Section). As expected for few-layer graphene channels, the devices showed a metallic behavior with minimal gate dependence (see Figure 2.1), which is ideal to form nanoelectrodes.

We etch nanogaps in the graphene channels using a feedback-controlled electroburning method (illustrated in Figure 2.2a) in ambient conditions that was inspired from a study by Prins and coworkers.[60] We apply a voltage ramp to a graphene device while measuring the corresponding current up to the point where the current starts to decrease. This negative differential conductance occurs from a reduction in channel width due to Joule-heating-

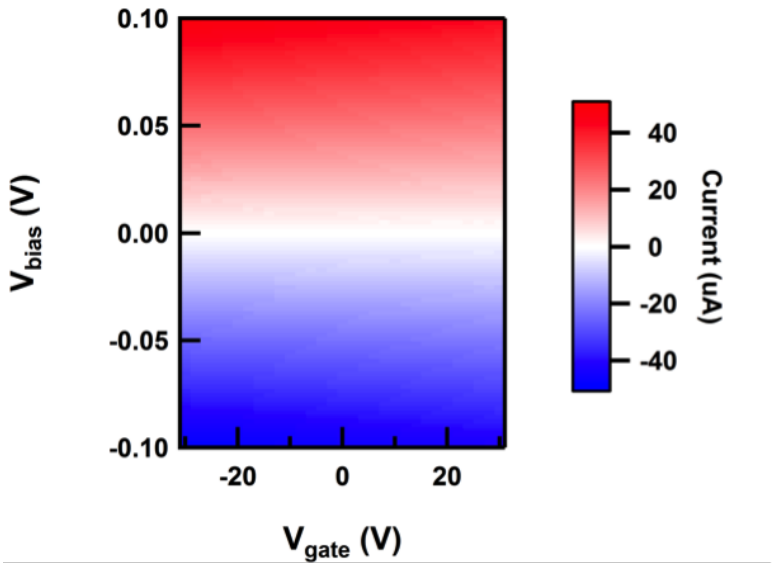

Figure 2.1: Current map of a few-layer graphene device as a function of drain-source bias (V_{bias}) and gate bias (V_{gate}), measured at room temperature in vacuum before electroburning. All devices at this stage show similar characteristics with negligible dependence of the current on gate bias.

induced combustion of the graphene channel edges[60, 116]. A feedback loop monitors the current at each voltage step and opens the circuit abruptly as soon as the negative differential conductance is detected. Using this method, it is possible to create controlled, incremental burning to precisely control the channel width. The current-voltage ramp is repeated multiple times (see Figure 2.2a) until the two sides of the graphene channel become disconnected and separated to form the nanoscale gap.

Ideally, this electroburning process occurs at approximately the midway point between the source and drain electrodes because this position corresponds to the point where the temperature profile due to Joule heating is higher, due to minimal heat dissipation into the

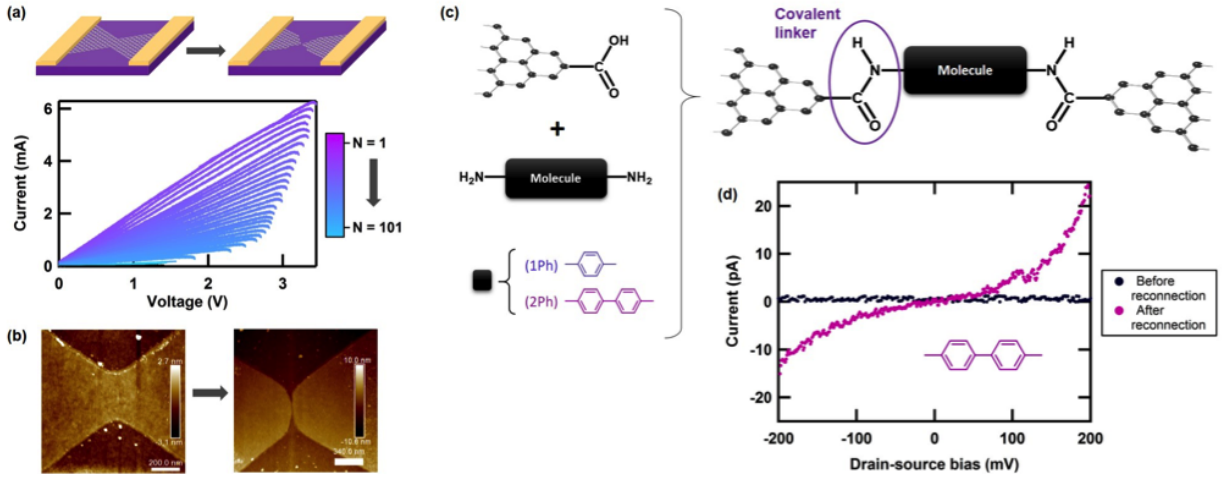

Figure 2.2: (a) Gaps are etched in graphene constrictions using a feedback-controlled electroburning process: N successive current-voltage traces are abruptly interrupted at the onset of a negative differential conductance, indicating shrinking of the constriction width. The process is repeated until the two graphene electrodes are separated. (b) Atomic force microscopy images of a graphene constriction before and after electroburning, showing the smooth round-off shape of electroburnt graphene electrodes with a gap length minimal in the center. (c) Reaction chemistry of short diamine molecules on the oxidized edges of graphene electrodes, leading to single-molecule circuits connected with covalent amide bonds as the contacts. Two diamine molecules were used in this study, *i.e.* 1,4-diaminobenzene (1Ph) and 4,4'-diaminobiphenyl (2Ph). (d) Current-voltage characteristics at 0 V gate bias and room temperature, showing negligible current across the nanogap at low bias and a significant increase in conductance after reconnection with a diamine molecule.

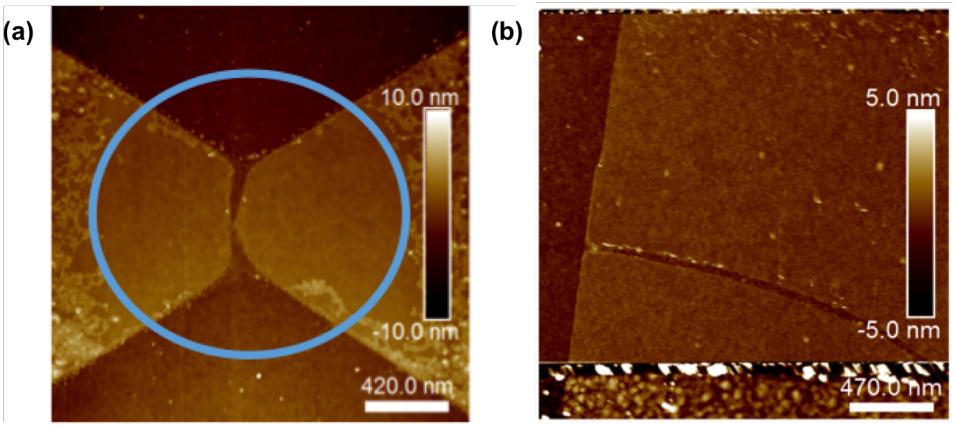

Figure 2.3: (a)AFM image of a device after electroburning, exhibiting a nanogap etched in the center of the graphene bowtie pattern and a circular area around the nanogap were resist residues that are annealed through Joule heating. (b)AFM image after electroburning of a device without the additional lithography step to constrict the channel in a bowtie shape. The electroburning region extends from one side of the channel to one of the electrodes, so that the source and drain leads are never disconnected.

electrodes (see the atomic force microscopy (AFM) image in Figure 2.3a). In many instances, the burning of the graphene starts from the edges of the sheets to progress towards the center until the channel is sectioned into two parts. This has been visualized in situ by Barreiro and coworkers[116]. However, we found that the electroburning process on graphene channels of random widths and shapes requires many thousands of current-voltage traces to disconnect the graphene leads, and often led to misshapen or partially-burnt graphene channels (see Figure2.3b). To improve this method so that it can support the subsequent chemistry described below, we implemented an additional lithography step before the electroburning to shape the graphene so that it has a 500 nm-wide constriction in the center of the channel

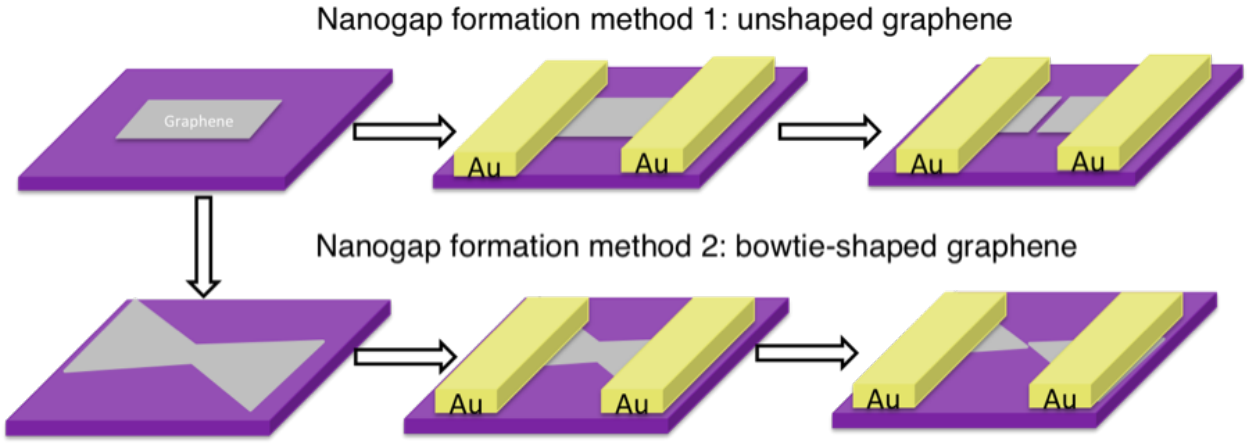

Figure 2.4: In Method 1 (top), devices are fabricated using graphene flakes as exfoliated, with a typical width between 2 and 10 μm. In Method 2 (bottom), exfoliated graphene flakes are first patterned in a bowtie shape using lithography and reactive ion etching (RIE). Subsequent steps for both methods include deposition of source and drain metallic microelectrodes, followed by electroburning to open a gap in the graphene channel.

(see Figure 2.2b).[63, 117, 118] Using this approach, we obtained a substantial increase from 30% to 88% in the ratio of successful gap formation in the center of the constriction (see Figure 2.4 and Table 2.1).

The right panel of Figure 2.2b shows a typical nanogap obtained from a bowtie-shaped graphene channel. Both electroburnt graphene electrodes exhibit a smooth round-off shape at the end, in that the sides of the electrodes display a larger separation between them compared to the center. The minimal separation length between the electrodes was too small to be precisely resolved in the AFM images, in particular due to the few-layer thickness of the flakes: while top layers were found to have a larger separation than the bottom ones,

	Number of devices tested	Number of nanogaps	Yield of nanogap formation
Unshaped graphene (method 1)	125	38	30%
Bowtie-shaped graphene (method 2)	96	84	88%

Table 2.1: (a) Number of devices tested with and without bowtie-shaping of the graphene channel, followed by the (b) number and (c) yield of these devices exhibiting a successful nanogap after electroburning, as assessed from electrical measurements and atomic force microscopy. Shaping a constriction in the bowtie channel dramatically increases the yield of successful nanogap formation.

it turns out that the shortest nanogap is difficult to access with the AFM tip due to the finite tip radius. However, we estimated the gap size of the electroburnt nanogap by fitting the tunneling current by using the Simmons model[63, 64, 110](see Figure 2.5). The gap size we estimated from the simulation is on the order of d = 0.91nm with a barrier height ϕ_0 = 1.07 eV, which demonstrated the ultrashort nanogap formed through the electrical breakdown. Unless when characterizing this tunneling current at high bias, we kept the source-drain bias in the low-bias range because nanogap edges tend to become unstable under high electric field.[117] Open nanogaps exhibit either no current or tunneling current in a ± 1.5V drain-source bias range and the drain-source current is independent of the gate voltage (see examples in Figure 2.6a-b). In some cases, we measure either Ohmic current-voltage traces (see Figure 2.6c), indicating devices that are not properly or fully etched, or gate-dependent Coulomb blockade features (see Figure 2.6d), indicating there is a remaining island that connects the graphene electrodes[39, 119]. We excluded devices exhibiting these two signatures from subsequent analysis.

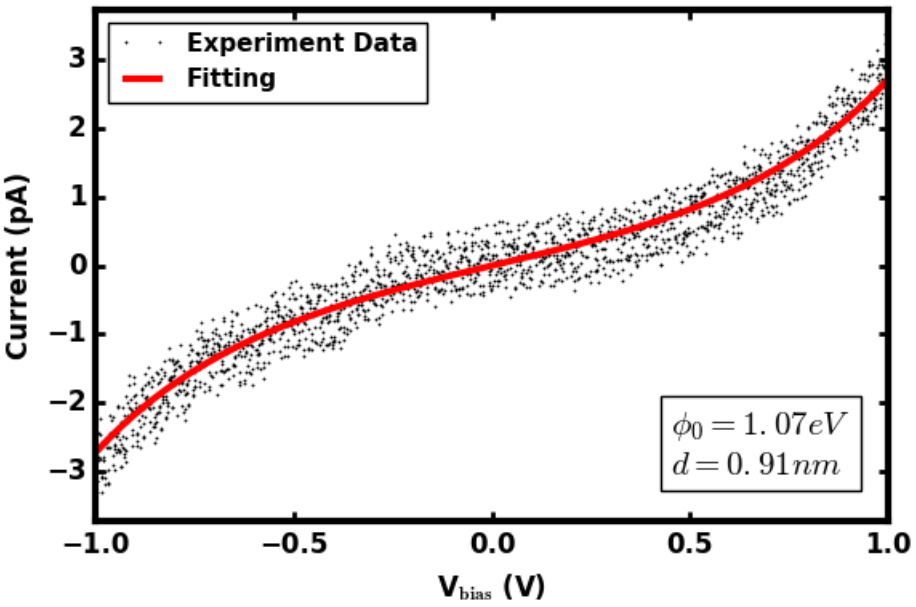

Figure 2.5: The tunneling current in a nanogap after electroburning but before reconnection is adjusted with the Simmons model. In this example, we find an estimated gap size of d = 0.91 nm and a barrier height ϕ_0 = 1.07 eV.

In all cases, the electroburning was done in air, so that the Joule-heat induced oxidation process forms carboxylic acid groups (-COOH) on the edges of the etched graphene.[114, 120] In the experiments that follow, we take advantage of this chemical functionality on the edge of the resulting graphene electrodes to covalently bridge the nanogaps with molecules, as illustrated in Figure 2.2c. Short molecules with good electron delocalization within the molecular backbone were used in this study, in particular 1,4-diaminobenzene (1Ph) and 4,4'-diaminobiphenyl (2Ph), which are 0.6 nm and 1 nm in length from nitrogen atom to nitrogen atom. These molecules are a good point of comparison because they have been well studied in STM-break junctions.[47] After the reconnection reaction, we characterized all devices using

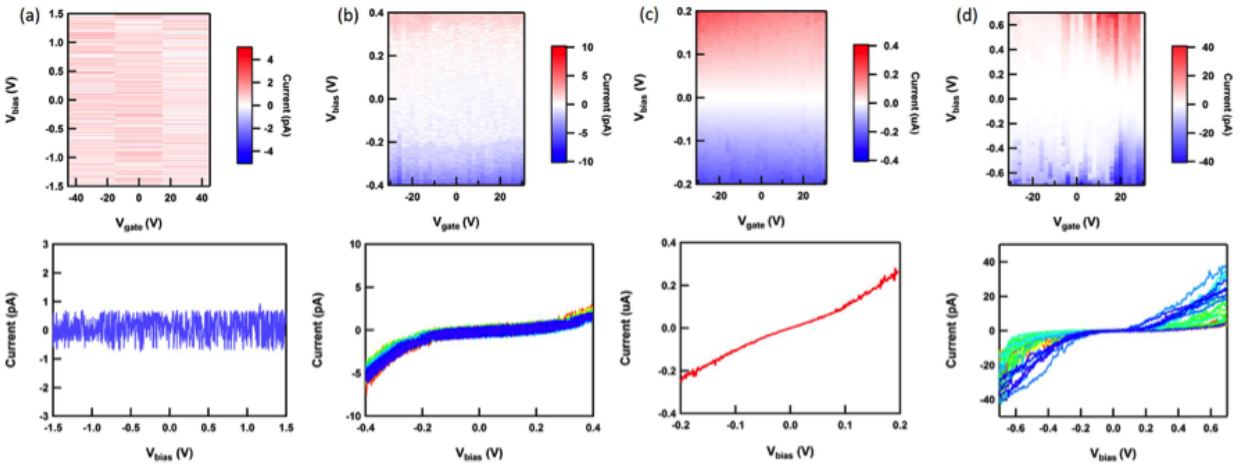

Figure 2.6: (a/b) Two possible signatures for successful nanogap formation: either no current is measured after electroburning (as in panels a) or pA-amplitude tunneling current is measured, exhibiting negligible dependence on gate bias (as in panels b). (c) Signature obtained with shorted nanogap: μA-range, ohmic current-voltage indicating partial electroburning, in which the two graphene leads are not disconnected, (d) Occasional Coulomb blockade signature obtained after electroburning (before reconnection chemistry), indicating a residual graphene island between the two main graphene leads.

gate-modulated two-terminal electron transport in vacuum. A number of devices were found to exhibit a significant increase in electrical conductance compared to that measured at low bias across the nanogap before reconnection, as illustrated in Figure 2.2d. We observed no such conductance increase after immersing the devices in a solution containing either only the diamine, or only the coupling agent 1-ethyl-3-(3-dimethylaminopropyl)carbodiimide (EDC) (see Figure 2.7), indicating that the current increase is related to the covalent reaction of diamine molecules. We studied the single-molecule nature of these transistors by character-

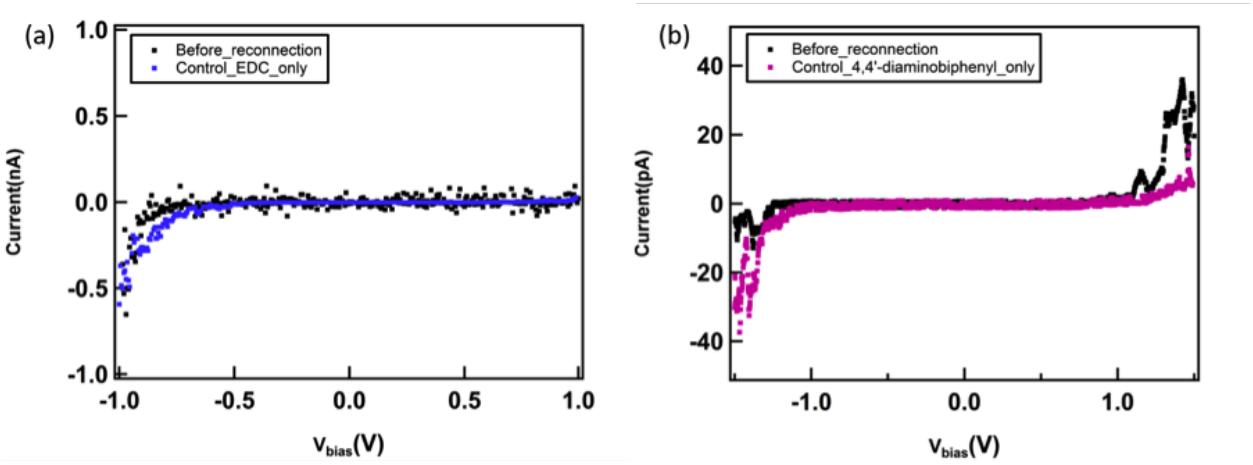

Figure 2.7: (a) Current as a function a drain-source bias, before and after reaction with only EDC (no diamine molecule); (b) Same before and after reaction with only the 4,4'-diaminobiphenyl molecule (no EDC activating agent). In both cases, no conductance increase is observed in any measured device.

izing the experimental dependence of the conductance increase with the coupling chemistry, molecular length, and gate voltage. We discuss the results from varying each of these parameters in the sections that follow.

2.3 Effect of coupling chemistry and molecule length

We used reaction chemistry that targets the carboxylic acid functional groups that adorn the graphene edges in the electroburnt region to form covalent amide bonds with a molecule terminated by two amine groups. We performed the condensation reaction between the carboxylic acid groups on the graphene edges and the amine groups on the termini of the

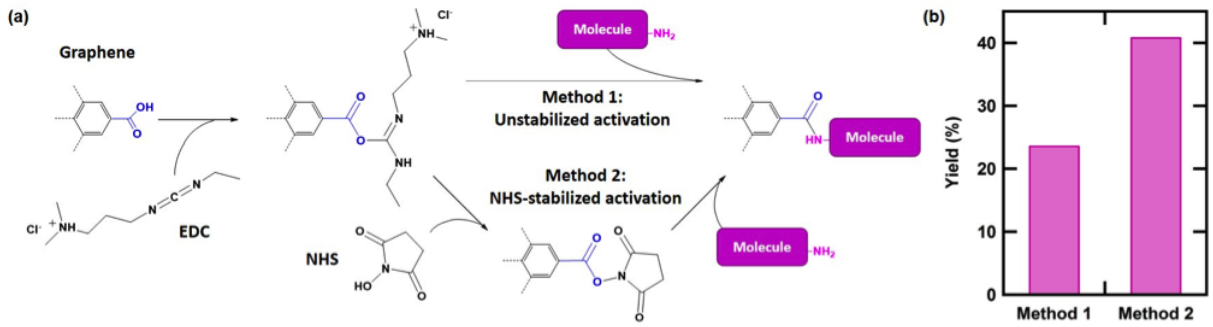

Figure 2.8: (a) Carboxylic acid groups formed on the edge of the graphene nanogaps are reacted in solution with the EDC activating agent. In Method 1 (Non-stabilized coupling), the activated carboxylic acid group reacts immediately with the diamine molecule already present in the solution. In Method 2 (NHS-stabilized coupling), the NHS molecule is used to stabilize the activated carboxylic acid group, resulting in an enhanced probability of amine binding. (b) Fraction of reconnected devices using the two different coupling protocols with 4,4'-diaminobiphenyl molecules.

molecule using two different protocols illustrated in Figure 2.8a. In the first reaction, labelled "unstabilized activation", the diamine and the EDC activating agent are introduced simultaneously to react with the COOH-functionalized graphene nanogap.[55, 61] To obtain a successful coupling, the diamine molecule must interact with the carboxylic acid site that has been transiently activated by the EDC group. In the second protocol, labelled "NHS-stabilized activation", the activation of carboxylic acid group with EDC is stabilized by the N-hydroxysuccinimide (NHS) group before introduction of the diamine[57]. This reaction was optimized recently for reacting a monoamine molecule to a single carboxylic acid functional group on the sidewall of a carbon nanotube[121]. We found the yield of reconnection

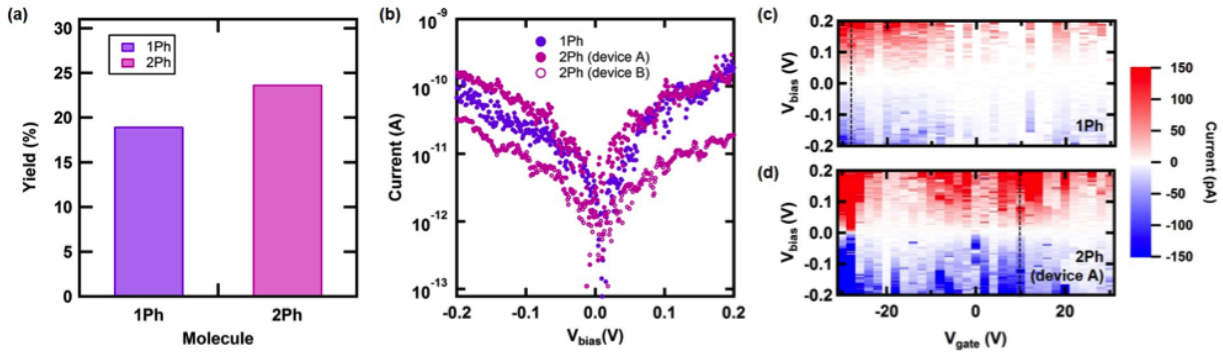

Figure 2.9: (a) Yield of reconnection obtained with 1Ph and 2Ph molecules using the same coupling chemistry (Method 1). (b) Current-voltage curves obtained for devices reconnected with 1Ph and 2Ph molecules, at gate bias optimizing alignment of energy levels (see panel c and d). Both coupling methods were used. Two different devices reconnected with the 2Ph molecule are shown here to illustrate the observed dispersion in conductance between devices. (c/d) Complete mapping of the current as a function of $[V_{bias},\ V_{gate}]$, at room temperature, for two of the devices in panel b (additional data in Figure 2.10). Dotted lines indicate the value of V_{gate} used in panel b.

to be significantly improved when stabilizing the activated carboxylic acid before reaction with the diamine molecules, as illustrated in Figure 2.8b. The results on the graphene gaps are consistent with prior studies on solution phase coupling using EDC in combination with NHS.[122] In particular, we report a reconnection yield of 41% using the 2Ph molecule, which is unprecedentedly high for such a short nanometer-scale molecular bridge[55].

To further study these single-molecule junctions, we connected graphene nanogaps using two different molecules: 1,4-diaminobenzene (1Ph) and 4,4'-diaminobiphenyl (2Ph), respectively 0.6 nm and 1.0 nm long between the two amine groups. We studied the effect of the

length of the molecule on the success rate of the reconnection reaction on graphene nanogaps, defined as the fraction of devices showing an increase in conductance with gate dependence after reaction chemistry. Figure 2.9a compares the yield of reconnection obtained in an ensemble of devices exposed to the 1Ph and 2Ph molecules. The fraction of nanogaps successfully reconnected by a molecule was measured at 19% for 1Ph molecules and 24% for 2Ph molecules, when each is coupled using Method 1. The higher success rate for the longer molecule is due to the longer molecule having a greater chance to match the electrode-to-electrode distance somewhere in the width of the nanogap. The smooth round-off shape of the electroburnt graphene electrodes makes them adapted to reconnect molecules of different lengths, which makes it a universal template.

Electrical current (I) versus drain-source bias voltage (V_{bias}) characteristics at a fixed gate voltage (V_{gate}) are presented in Figure 2.9b for three different devices reconnected with either the 1Ph molecule (purple) or the 2Ph molecule (pink). Each device exhibits a strong gate dependence, as illustrated in Figure 2.9 c and d showing complete current characteristics as a function of $[V_{bias},\ V_{gate}]$. In order to compare the conductance between different devices, current-voltage curves were extracted from a complete $[V_{bias},\ V_{gate}]$ mapping of the current, at the gate potential showing maximal transmission across the junction - or, in other words, at the best alignment between the electronic states of the molecule and the electrodes (see dotted line in Figure 2.9 c and d). No correlation was observed between the electrical conductance curves and the coupling chemistry used (Method 1 or 2), as expected since the final graphene-molecule-graphene construct is the same regardless of the use or not of NHS stabilizer. Details and additional data are provided in Fig. S7 in the Supporting Information. As shown in Figure 2.9b, we report comparable electrical signatures from

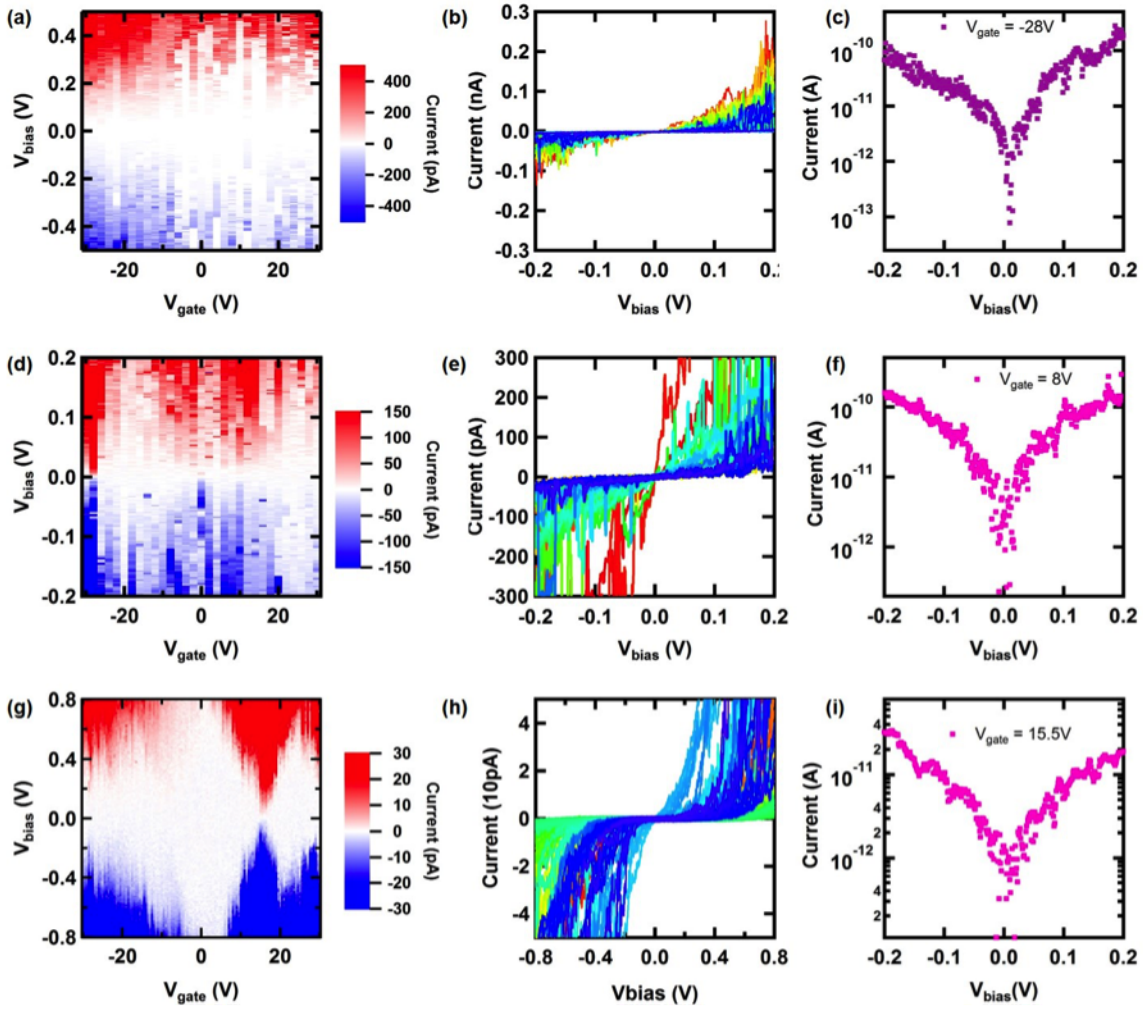

Figure 2.10: (a) Full electrical characteristics showing the current as a function of drain-source bias and gate bias [V_{bias}, V_{gate}] for a device reconnected with a 1Ph molecule, at room temperature. (b) Individual current-voltage curves at different gate bias, going from -30V (red) to +30V (blue). (c) Current-voltage curve (amplitude) extracted at -28V which corresponds to the optimal transmission in the [-30V, 30V] gate bias range. (d/e/f) Same for a 2Ph device at room temperature (2Ph device A). (g/h/i) Same for a 2Ph device cooled down at 100K (2Ph device B). All measurements were done in vacuum (P $< 1e^{-4}$ Torr).

devices made of 1Ph and 2Ph molecules, which is explained by two reasons: First, as expected in any single-molecule measurements, there is a significant dispersion in the conductance values between different devices made of the same molecule, as illustrated in Figure 2.9b with two different 2Ph devices. A similar dispersion is obtained when sampling thousands of individual molecules using break-junction measurements[48, 123], which produces some overlap between 1Ph and 2Ph devices when taking a limited number of individual current-voltage traces. Second, absolute conductance values of the three devices in Figure 2.9b are comprised in a $10^{-6} - 10^{-5} G_0$ interval, as calculated at $V_{bias} = 0.2$ V, where $G_0 = 2e^2/h$ is the quantized conductance unit with e and h are electron charge and the Plank constant, respectively. This is 2-3 orders of magnitude lower than the conductance measured for these molecules in amine-gold junctions[124], which suggests the contribution of a large contact resistance. The nature of this contact resistance is discussed in the following section.

2.4 Nature of the transport across covalent contacts

The analysis of this contact resistance is particularly informative. The contact resistance we obtain for these covalent bonds on graphene (see Figure 2.11) is significantly higher ($> 100 M\Omega$) than those reported for Au-NH2 contacts ($\sim 1 M\Omega$) with similar molecules[48]. It is however comparable to that reported by Zhu and coworkers using amide bond contacts with carbon nanotube electrodes.[57] The high contact resistance measured in the present study suggests a significant break of conjugation at the carbonyl site of in the covalent amide bonds, preventing the delocalization of the electronic wave function between graphene electrodes and the molecular backbone. This result contrasts with break junction

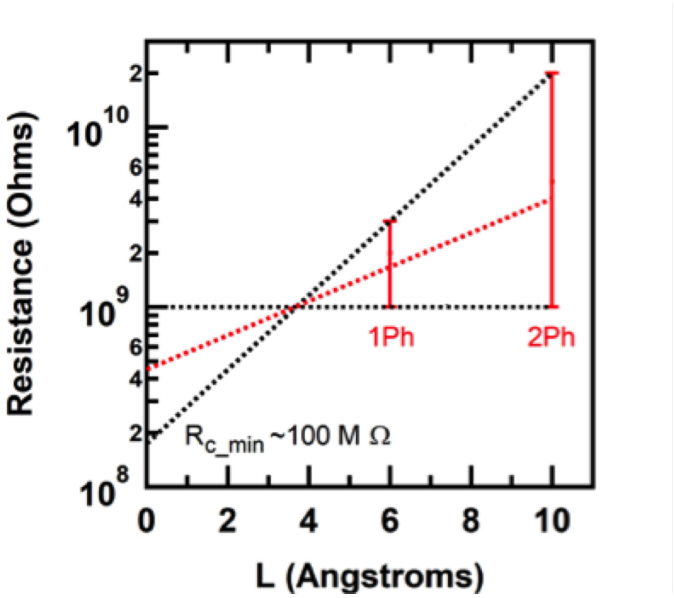

Figure 2.11: Range of resistance values for 1Ph and 2Ph (red bars) obtained from the slope of current-voltage curves in Figure 2.9b and Figure 2.13. Dotted lines illustrate various possible linear adjustments of the resistance values as a function of molecule length L, considering the minimum, average (red) and maximum slopes allowed by the range of resistance values. Dotted lines are extrapolated to L=0 to estimate the contact resistance Rc $>$ 100 MΩ.

experiments and theoretical calculations obtained on N-phenylbenzamide molecules, showing strong electronic delocalization and conductance across the central amide bond[125, 126]. The difference likely stems from the solid-state nature of the present junctions: either the fixed position and spacing of the graphene electrodes and the oxide surface prevent the relaxation of the molecular bridge in a conformation favorable for graphene-molecule coupling, or the electroburnt graphene edges present a significant amount of disorder and defects in the vicinity of the reconnected area that increases the contact resistance between the graphene sheets and the molecular bridge.

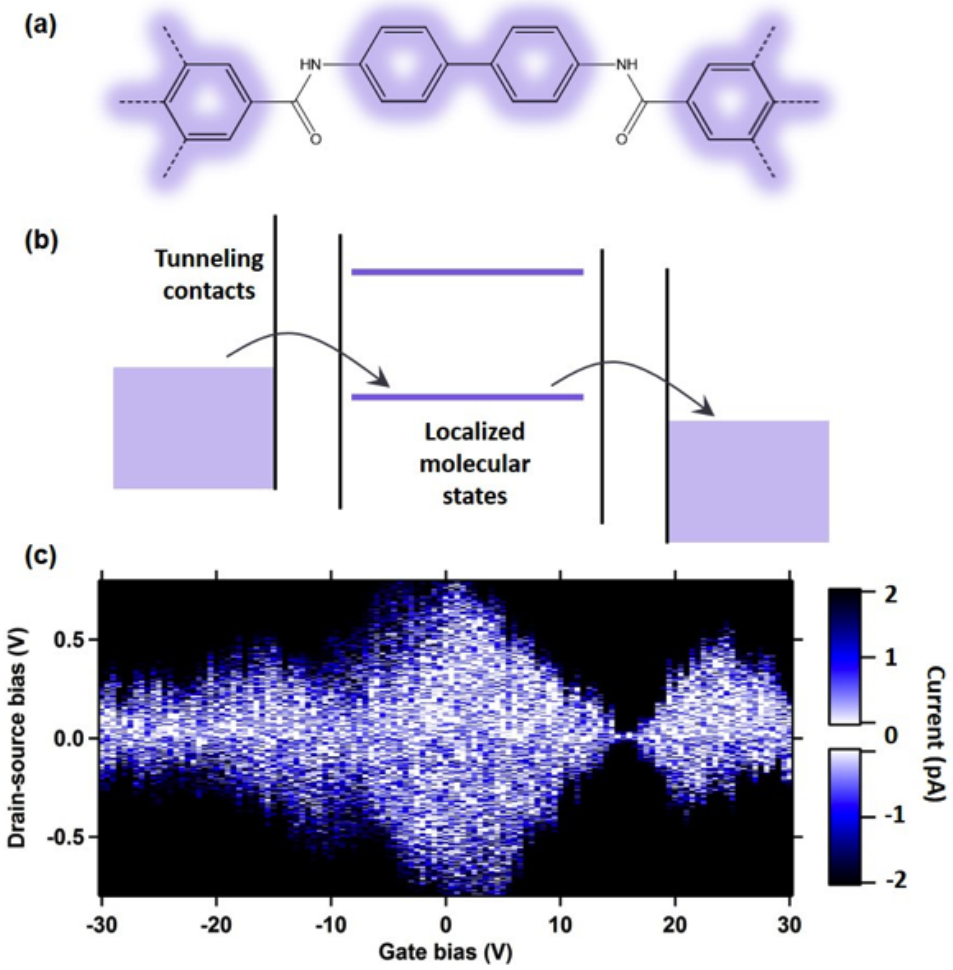

Figure 2.12: (a) Representation of the wave function localization due to the break of conjugation across the contacts. (b) Diagram of single-electron tunneling across discrete electronic states isolated between two tunneling barriers. (c) Transporting current across a device reconnected with the 2Ph molecule as a function of the bias voltage and gate voltage, measured at 100K, showing Coulomb blockade diamonds indicative of localized electronic states in the junction.

The break of electronic conjugation at the contacts suggests the confinement of discrete molecular orbitals between the contacts (as represented in Figure 2.12a), which may result in single-electron tunneling in charge transport measurements across the junction, as schematized in Figure 2.12b. To verify this hypothesis, we measured the dependence of the conductance of reconnected devices with gate bias at low temperatures. Figure 2.12c displays an example from a 2Ph-reconnected device measured in vacuum at 100 K, showing a 2D plot of the electrical current as a function of the drain-source bias (V_{bias}) and gate bias (V_{gate}). The striking feature of the plot is the multiple, parallel diagonal interfaces defining diamond-shaped regions with suppressed electrical conductance inside the diamond regions. These features are a typical signature of the Coulomb blockade effect in single-electron transistors[41, 42, 114, 127, 128], whose appearance indicates the presence of small conducting island that can be charge up to allow only single electron transport. Electrons can transfer across the junction only when one or more of the electronic states of the molecule align within the energy separation between the source and drain electrodes, resulting in diamond-shaped domains representing a range of [V_{bias}, V_{gate}]. In the diamond region, electron conductance is blocked because the source and drain energy separation lies between electronic states of the molecule.

The shape and size of Coulomb diamonds are linked to the energy of the molecule's electronic levels and its electrostatic coupling to the electrodes. The height of each diamond, i.e. the energy separation between $V_{bias} = 0$ and the top (or bottom) of the diamond, is defined as the addition energy E_{add}, which consists of the energy separation between the corresponding electronic levels in the molecule ($\triangle E$) plus the charging energy E_C due to Coulomb interactions between the electron and the electrostatic environment.[129] The

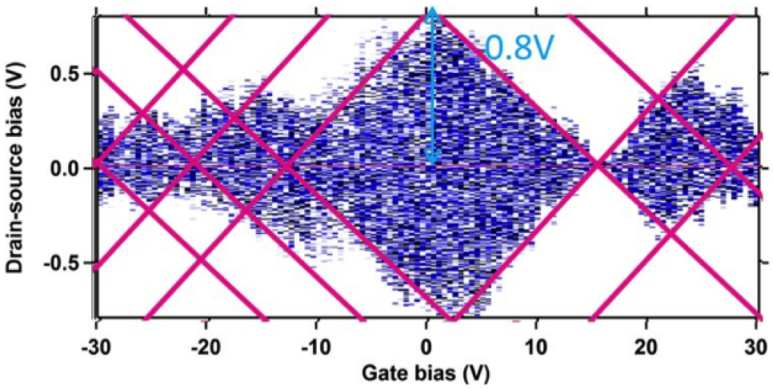

Figure 2.13: Same data with Figure 2.12b (in inverted colors for clarity) superimposed with the corresponding Coulomb diamond structure, revealing 4 distinct diamonds. The addition energy corresponds to the height of a diamond. For the large central diamond, we find an addition energy $E_{add} = 0.8$ eV and between 0.2 and 0.4 eV for the smaller ones.

heights of diamonds in Figure 2.13 c correspond to addition energies between $E_{add} \sim$ 0.2-0.8 eV (see Figure 2.13), which is consistent with studies on other comparably-small, nanometer-scale single-electron transistors in the literature[42, 60, 116, 127]. As expected, it contrasts with Coulomb blockade measurements on larger structures, like carbon nanotube quantum dots, where addition energies are on the order of the meV.[130] The observed addition energies of 0.2 - 0.8 eV in Figure 2.12 c are definitely smaller that the HOMO-LUMO gap of the free-standing 2Ph molecule or bridge ($\sim$ 4eV, see Figure 2.14 and Table2.2. This is actually a recurrent observation in single-molecule transistors [56, 62]. This phenomenon is usually explained by renormalization corrections of the electronic spectrum by $\sim$ 3 - 4eV[62] or by attributing the observed addition energies to transitions between deeper, denser HOMO levels rather than the HOMO-LUMO gap [56]. Because of the high-energy separation and

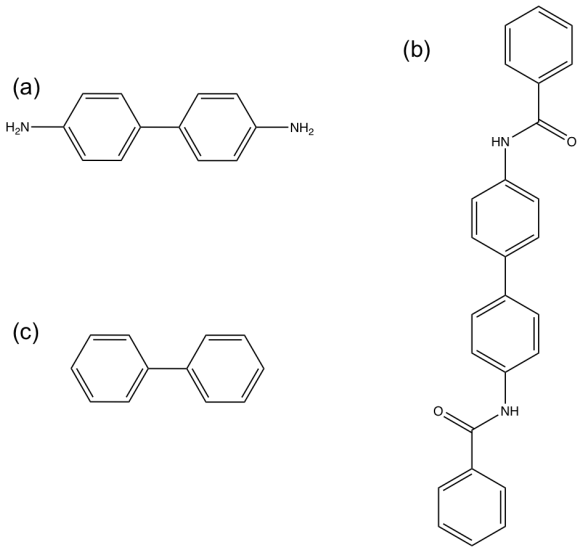

Figure 2.14: Molecules used in the DFT calculations: (a) 4,4'-diaminobiphenyl (2Ph), (b) N,N'-4,4'-biphenyldiyldibenzamide and (c) biphenyl.

small molecular size in our single-molecule devices, the Coulomb diamond structure can be distinguished even at room temperature in some of the devices (see Figure 2.9 c and d, as well as Figure 2.10), as reported for comparable ultra-confined quantum dots and single-molecule transistors [60, 131]. From the biggest Coulomb diamond, we are able to calculate the gate coupling parameter $\alpha = 0.027$ which is consistent with similar work such as Mol *et al* [62], who report α parameters of 0.006-0.04 for electroburnt graphene electrodes on 300nm SiO_2. This single-molecule tunneling signature was only seen in devices showing conductance increase after the reaction chemistry, and initial measurements of the corresponding nanogaps prior to the chemistry displayed no gate dependence (see Figure 2.6 a-b). The appearance of single-electron transport features supports the tunneling nature of the covalent contacts in these solid-state junctions.

Energy Levels (eV)	(a)	(b)	(c)
LUMO+3	1.802	-0.370	0.868
LUMO+2	0.494	-0.402	0.056
LUMO+1	0.333	-1.130	-0.072
LUMO	0.252	-1.342	-0.703
HOMO	-4.474	-5.391	-6.047
HOMO-1	-5.549	-6.413	-6.768
HOMO-2	-6.359	-6.801	-6.789
HOMO-3	-6.390	-6.817	-7.415
HOMO-4	-7.658	-6.857	-9.009

Table 2.2: Theoretical energy levels in eV of molecules in Figure 2.14

2.5 Conclusion

This chapter describes a new method to assemble single molecule circuits with graphene electrodes. The electrodes are formed through an electroburning process optimized by patterning graphene channels in a bowtie shape. This insures that the breakdown induced by the electroburning occurs cleanly in the middle of the device. Using this technique, we were able to create nanoscale gaps in high yields that are terminated with carboxylic acid groups. We explored and optimized covalent chemical reactions to reconnect the nanogaps with diamine-terminated molecules and found that single-molecule circuits can be achieved in high yields using an NHS-stabilized activation strategy. In these single-molecule devices, we observed Coulomb blockade as well as dependence with molecule length. The high yield and versatility of this approach augur well for creating a new generation of sensors, switches, and other functional devices using graphene contacts.

2.6 Experimental section

2.6.1 Fabrication of graphene devices

Few-layer graphene flakes were mechanically exfoliated and transferred on degenerately-doped silicon substrates with a 285-nm thermal silicon oxide layer. A grid of alignment marks with 50 μm pitch was added using electron beam lithography (Nanobeam nB4, PMMA A4 495k + A6 950k) and electron beam metal evaporation (Angstrom, 1 nm Ti + 25 nm Au). Optical microscopy imaging (Nikon LV100) and Raman spectroscopy (Renishaw inVia micro-Raman, 532nm laser wavelength) were used to map the position of isolated few-layer graphene flakes with respect to the alignment grid and assess their thickness/number of layers. Electron beam lithography was employed a second time (PMMA A4 495k + A2 950k) to pattern electrodes with channel lengths of 2 μm, then metallic source/drain electrodes (1 nm Ti + 20 nm Pd + 50 nm Au) were deposited using electron-beam evaporation. .

2.6.2 Formation of graphene nanogaps

We used feedback-controlled electroburning as described by Prins *et al*[60] to produce graphene nanogaps. The electroburning process was conducted in ambient atmosphere and temperature inside a Lakeshore TTP4 probe station, and goes as follows: A voltage ramp is applied to the source-drain electrodes while recording the corresponding source-drain current I(V). Each data point is monitored to detect the onset of negative differential conductance ($\triangle I = I_{max} - I_{current} > \triangle I_{threshold}$), at which point the voltage is brought back abruptly to zero. This process is repeated until the device resistance reaches 1 MΩ. Devices were then

imaged in atomic force microscope (AFM, Bruker Dimension) and electrically probed in vacuum (see details below) to confirm the opening of a nanogap. Devices showing incomplete gap formation, i.e. showing ohmic conductance and/or gate dependence, were submitted a second time to electroburning and re-characterized with AFM and vacuum electrical probing.

In order to improve the yield of nanogap formation and to control the nanogap position, a constriction was first shaped in the center of the graphene devices, before starting the electroburning process. A third step of electron beam lithography (PMMA A6 950k) was executed to expose the graphene surrounding a 500 nm-wide constriction shape, which was then etched using oxygen reactive ion etching (250 mTorr O_2, 50W).

2.6.3 Reconnection chemistry

Diamine molecules were attached to the oxidized graphene edges by a condensation reaction of their respective NH_2 and COOH moieties in amide bonds. Two different diamine molecules were used in this study: 1,4-diaminobenzene (Sigma-Aldrich) and 4,4'-diaminobiphenyl (Fluka), leading respectively to the monophenyl (1Ph) and biphenyl (2Ph) molecular bridges. Two versions of the coupling protocol were used (see Figure 2.8). In Method 1 (unstabilized activation), 10μM to 100mM of diamine molecule and 1mM COOH-activating agent 1-ethyl-3-(3-dimethylaminopropyl)carbodiimide (EDC, Thermo Scientific) were mixed in 2mL anhydrous pyridine (Sigma-Aldrich). Substrates were immersed 24h in this solution, then rinsed with clean pyridine and dried using a flow of N_2. In Method 2 (NHS-stabilized activation), substrates were first immersed in a solution of 1mM EDC and 1mM N-hydroxysuccinimide (NHS, Sigma-Aldrich) in anhydrous dimethylformamide (DMF, Sigma-Aldrich) for 15 min. After rinsing in clean DMF, substrates were then immersed in

a solution of 100 μM diamine in pyridine for 30 min and rinsed in clean pyridine, isopropyl alcohol, acetone and dried with a flow of N_2.

2.6.4 Electrical measurements

Current-voltage measurements were realized in a vacuum cryogenic probe station (Lakeshore TTP4), with 10 μm-tip beryllium-copper probes for the drain and source connections and a conductive chuck to apply gate potential. Computer-controlled source units were used to apply DC potentials (Yokogawa 7651 for source-drain bias and Keithley 2400 for gate bias). Current measurements were acquired using a current preamplifier (Stanford Research System SR570) and a digital multimeter (Keysight 34401A). All device measurements were performed in vacuum (P $< 1e^{-4}$ Torr), either at room temperature or at 100 K using liquid nitrogen cooling.

2.6.5 Tunneling current fitting

According to the Simmons model[64], the dependence of current density J on bias voltage V is characterized with two parameters: the barrier height ϕ_0 and the gap size d:

$$J = (\frac{e}{2\pi h d^2})[(\phi_0 - \frac{eV}{2})[-\frac{4\pi d}{h}(2m)^{\frac{1}{2}}(\phi_0 - \frac{eV}{2})^{\frac{1}{2}}] - (\phi_0 + \frac{eV}{2})[-\frac{4\pi d}{h}(2m)^{\frac{1}{2}}(\phi_0 + \frac{eV}{2})^{\frac{1}{2}}]]$$

where: e - charge of electron; m - mass of electron; h - Planck's constant.

We optimized the barrier height and gap size by fitting the experimental tunneling current data, with cross-sectional area size considered as a prefactor.

2.6.6 DFT calculations

Quantum chemical calculations were performed using Jaguar, version 8.2, Schrodinger, Inc., New York, NY, 2013.[132] All geometries were optimized using the B3LYP functional and the 6-31G** basis set.

Chapter 3

Single-Crystal P-N Heterojunction Inspired by Ball-and-Socket Motif[1]

3.1 Introduction

This chapter describes a novel single-crystal p-n heterojunction at nanoscale inspired by the ball-and socket motif between fullerene and contorted dibenzotetrathienocoronene (c-DBTTC). In the past few decades, organic electronics have received world-wide interest due to the merits of low-cost, high-flexibility and light-weight. [65, 66] Besides, the organic materials, such as the small molecules and polymers, allow numerous molecule designs, which promotes the improvement of the device performance and diversity of functionality. With the efforts devoted by researchers, organic electronics with different functionalities has been fabricated, including solar cells [68, 69], sensor [73], transistors [74, 75], organic light-emitting

[1]This work is an unpublished work collaborating with Dr. Yu Zhong and Dr. Ying Wu

devices [16, 17]. As the elementary building block in the sophisticated integrated circuits, p-n heterojunctions, forming at the interfaces between p-type and n-type semiconductors, play an important role not only in inorganic electronics [133–135], but also in organic electronics [68, 82, 83]. However, there are only a few studies reported on organic single-crystal p-n heterojunctions, which provides a basic platform to investigate charge transport between p-type and n-type semiconductors and photoelectric conversion in the devices. [136]

Due to the fragile properties of organic semiconductor, traditional strategies used to fabricate inorganic p-n heterojunction is not appropriate for organic materials. As a consequence, new techniques are needed to construct organic single-crystal p-n heterojunctions. Due to various noncovalent interactions between organic semiconductors, such as π-π interactions, hydrogen bonding and electrostatic interactions, researchers have reported a few bottom-up self-assembly processes [137], including vapor-phase synthesis [84, 138] and solution [139] method. In order to form single-crystal p-n heterojunctions, we first need to select two semiconducting materials that satisfies the following requirements: first, there is strong intermolecular interactions between them; second, they have similar lattice constants. [140–142] According to previous studies, there exists strong π-π interaction between fullerene and hexabenzocoronene due to the ball-and-socket shape-complementarity. [81] Similar shape-matching occurs also in fullerene and derivatives of hexabenzocoronene, such as c-DBTTC. [76] Besides, the energy diagram of fullerene and DBTTC matches each other so that there should be efficient charge transfer between them. [143]

Since there are numerous studies on the controllable synthesis of C_{60} nanocrystal both in solution and directly on the substrate, [78, 79, 144] and c-DBTTC has a tendency to form two-dimensional columnar stacking structure [81], we decided to adopt a two-step self-

assembly strategy to fabricate single-crystal C_{60}-DBTTC heterojunction at nanoscale. We first synthesized the fullerene nanocrystals using the droplet-pinned crystallization method and then selectively grew c-DBTTC single-crystals from gas phase with the physical vapor transport crystallization method. We varied the growth condition of c-DBTTC to study the morphology change of the C_{60}-DBTTC heterojunction and also characterized it with different techniques. In addition, we used fluorescence microscopy to study the charge transfer in this heterojunction.

3.2 Fullerene needle crystal growth

Directly growth of C_{60} needle crystals was conducted with a modified droplet-pinned crystallization method reported by Li *et al* [78] (as shown in Figure 3.1A). We first dissolved C_{60} powder in m-xylene to make 0.4mg/mL solution. 20 μL C_{60} solution was drop-casted on the 1×1 cm Si/SiO_2 wafter with a 0.4×0.4 cm pinner in the center. Needle crystals formed after leaving the wafer in the petri dish overnight, as shown by the scanning electron microscope (SEM) image in Figure 3.1B. The needle crystal is characterized with diameter ranging from hundred nanometers to few micrometers and length ranging from few micrometers to hundred micrometers. We obtained the infrared (IR) spectrum of the C_{60} crystal before annealing (see Figure 3.2A) and found that the absorption peak at 770 cm^{-1} belongs to m-xylene and peaks at 1180 cm^{-1}, 1426 cm^{-1} are typical peak of C_{60} [80], which indicates that the C_{60} is a solvated structure with m-xylene trapped in the lattice. Because the as-grown C_{60} crystals need to be subjected to high temperature for c-DBTTC crystallizing, we conducted a mild heat treatment of C_{60} crystals to remove m-xylene solvated in the

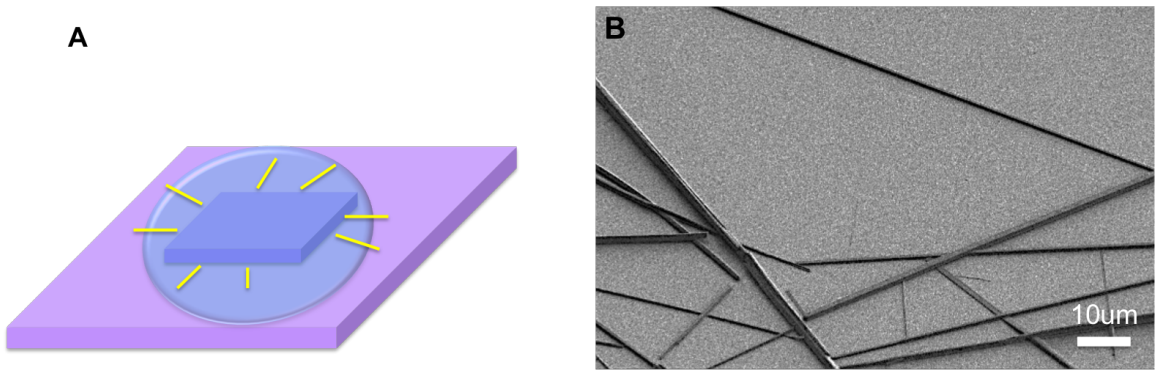

Figure 3.1: (A) Schematics showing the growth of C_{60} with the droplet-pinned crystallization method. (B) SEM image of C_{60} needle crystals after annealing at 60 ^{o}C for 10h (inset: zoom in image of the same nanorods) Scale bar: 2 μm

structure. The removal of m-xylene was done by heating the sample at 60 ^{o}C for 10h under vacuum. By comparing the IR spectrum after annealing (see Figure 3.2B), we found that was the intensity of peak at 770 cm^{-1} almost disappeared, which represents the successful removal of m-xylene.

3.3 Self-assembly of c-DBTTC on C_{60}

The pretreated as-grown C_{60} crystals on the substrate were then used as the template for selective crystallization of c-DBTTC crystals from the gas phase using the horizontal physical vapor transport crystallization method. As shown in Figure 3.3). The c-DBTTC powder was placed in a boat at the center of a tube furnace and the substrate with C_{60} was placed in the downstream side of the tube. The whole crystallization process was conducted under argon flow, which protects the C_{60} from oxidation. By varying the distance of the substrate

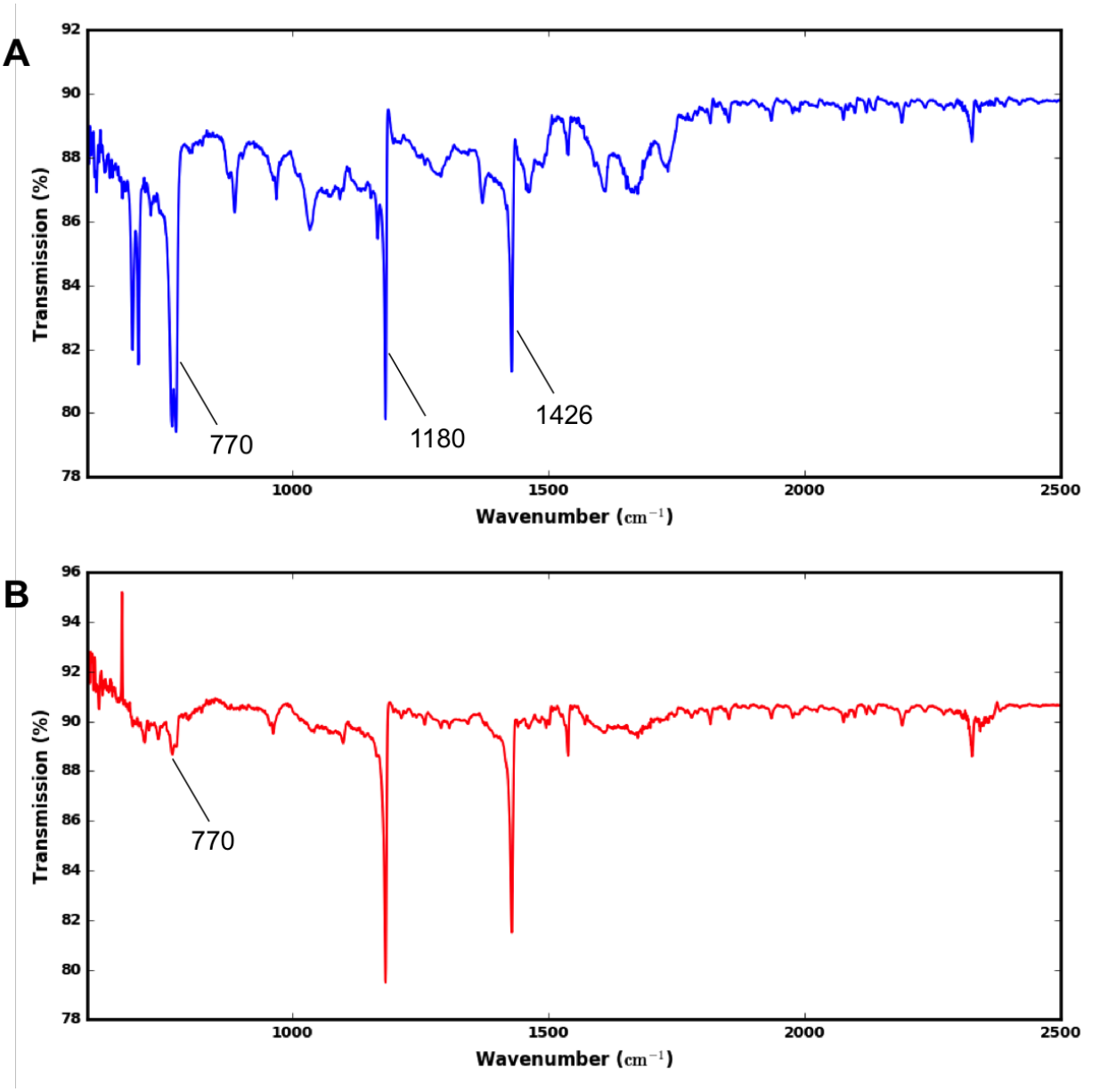

Figure 3.2: (A) The IR spectrum of C_{60} before annealing. The peak at 770 cm^{-1} indicates the existence of m-xylene.Peaks at 1180 cm^{-1}, 1426 cm^{-1} are typical peak of C_{60}. (B) IR spectrum of C_{60} after annealing at 60 ^{o}C for 10h, the peak intensity at 770 cm^{-1} greatly reduced, indicating removal of m-xylene.

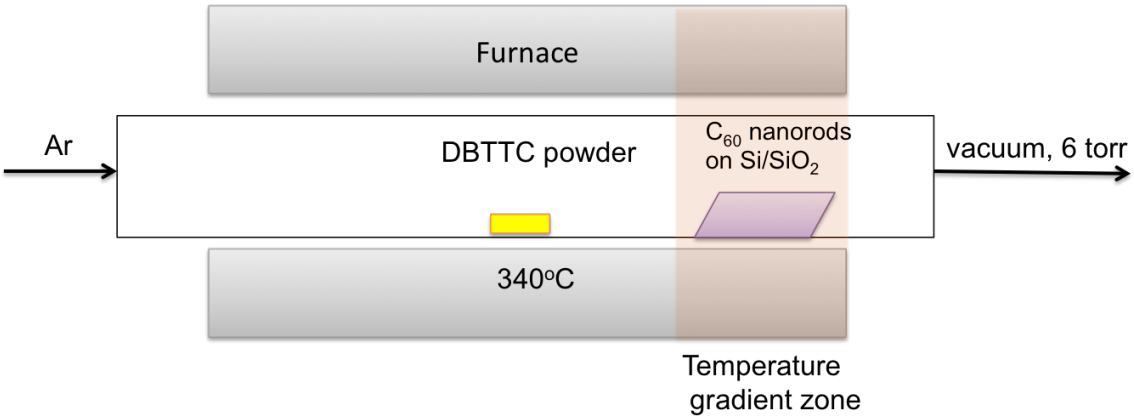

Figure 3.3: Schematics showing the horizontal physical vapor transport crystallization of c-DBTTC. The c-DBTTC powder was placed in a boat at the center of a tube furnace. The C_{60} crystals on Si/SiO_2 substrate was placed in the downstream side of the tube within a temperature gradient zone. The growth was conducted at 340 ^{o}C under Ar protection.

from the edge of the furnace, we are able to control the crystallization temperature of c-DBTTC. We first did a control experiment to monitor if there is any morphology change of C_{60} crystals by not adding c-DBTTC powder in the system. We placed two substates with C_{60} crystals in the lowest and the highest temperature, respectively, and then raised the temperature of the furnace to 340 ^{o}C for 6h. We checked the morphology of the C_{60} crystals at both temperature and found that they were still very smooth without any protrusions, as can be seen in SEM images in Figure 3.4 A and B. Then we monitored the c-DBTTC crystal growth by varying the growth conditions: temperature, time and pressure. The results are discussed separately as follows.

We first investigated influence of crystallization temperature on the selectively growth of c-DBTTC on C_{60} crystals. We ran the crystallization experiments by placing the substrate

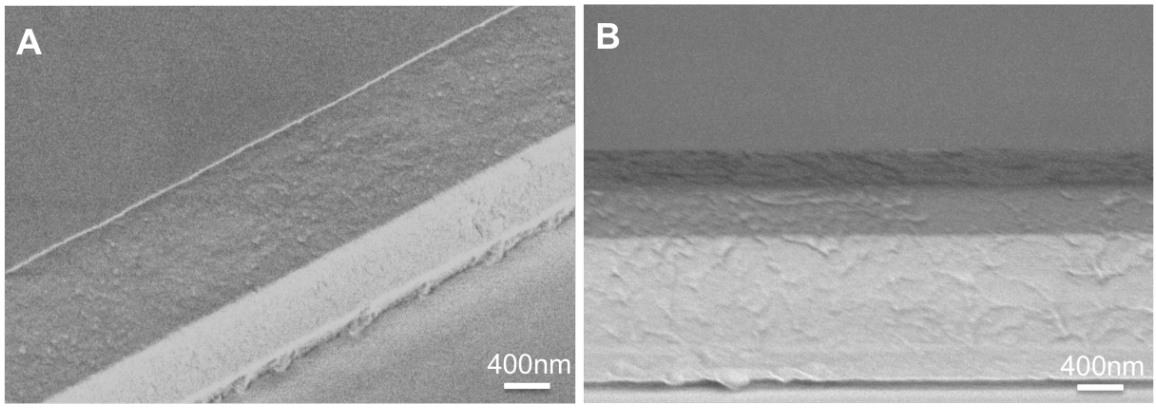

Figure 3.4: (A) Morphology of C_{60} needle crystals after control experiment without adding c-DBTTC powder at 165 ^{o}C (the lowest crystallization temperature). (B) Morphology of C_{60} needle crystals after control experiment without adding c-DBTTC powder at 260 ^{o}C (the highest crystallization temperature). Scale bar: 400nm

with C_{60} at four different temperatures: 165 ^{o}C, 205 ^{o}C , 240^{o}C and 260 ^{o}C. And the growth time is 6h under 6 torr. As can be seen from SEM images in Figure 3.5, nanoplates of c-DBTTC were selectively grown on the surface of C_{60} crystals by exploiting the C_{60} crystal as template. The selective growth of c-DBTTC on C_{60} needle crystal at nanoscale indicated the formation of C_{60}-DBTTC p-n heterojunction due to the ball-and socket shape-matching between them. Comparing the images at different crystallization temperatures, we found that the morphology and amount of c-DBTTC crystals both changed a lot. At 165 ^{o}C , there are a few small triangle-shaped nanoplates of c-DBTTC grown on the C_{60} crystal and most of them are grown perpendicular to surface of the needle crystal. When the temperature increased to 205 ^{o}C, the amount and thickness of c-DBTTC nanoplates increased and the nanoplates are still perpendicular to surface of the needle crystal. When the temperature

increase to 240^{o}C, the amount and thickness of c-DBTTC nanoplates further increased and they almost covered the whole surface of C_{60} crystal. However, the c-DBTTC nanoplates were not too much that they couldn't grown perpendicular to surface of the C_{60} needle crystal any more. When the temperature increased to 260 ^{o}C, c-DBTTC nanowires started to self-assembled on C_{60} crystals and they covered the whole C_{60} crystal. As a consequence, 240^{o}C $\sim$ 260 ^{o}C is a threshold temperature for the morphology change of c-DBTTC crystal grown on the C_{60} crystal. The reason that the morphology of c-DBTTC crystals changed from nanoplate to nanowire is: as the crystallization temperature increased, the nucleation rate decreased and crystal growth rate increased, which promotes to form long nanowires.

We then studied the effect of growth time on the C_{60}-DBTTC heterojunction formation. We carried out the crystal growth of c-DBTTC at 205 ^{o}C at 6 torr for 2 h, 4 h, 6 h and 8 h. As shown in Figure 3.6, when the growth time increased, the amount of c-DBTTC nanoplates gradually increased and the nanoplates became thicker. As a result, by controlling the crystallization time, we can easily tuned the amount and thickness of c-DBTTC nanoplates on the C_{60} crystals. We then continued to investigate the influence of pressure on the morphology of c-DBTTC crystal formation at the same crystallization temperature. From the above results, we found that the growth time affects number of crystals a lot, but only slightly change in the morphology of crystals, *i.e.*, the crystal wouldn't change from a nanoplate to a nanowire. So in order to have comparable of c-DBTTC crystals on the C_{60} crystal, we varied the crystallization time together with the pressure. Because the higher the pressure, the slower the crystallization rate, we extended the crystallization at high pressure for a longer time and shorten that of low pressure. As can be seen in Figure 3.7A, when the pressure is 5 torr, a layer of c-DBTTC crystals formed and covered the whole surface of

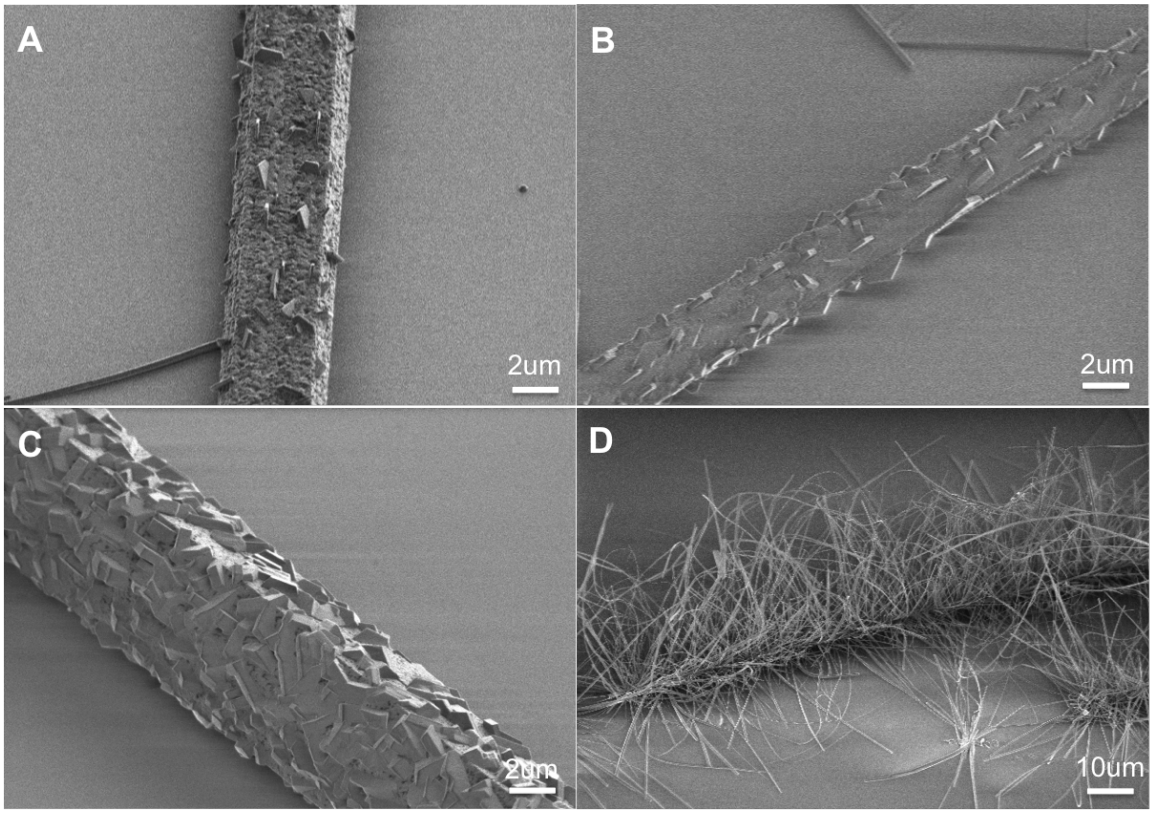

Figure 3.5: c-DBTTC grown on C_{60} needle crystals at different temperatures at 6 torr for 6h: (A) 165 ^{o}C , (B) 205 ^{o}C, (C) 240^{o}C, (D) 260 ^{o}C. Scale bar: 2um

a C_{60} crystal. Compared with c- DBTTC nanoplates grown at 6 torr (as shown in Figure 3.7B), they are much smaller and condenser that it's difficult to distinguish one by one. This is because lower pressure gives higher nucleation rate, which leads to smaller crystals and larger amounts of crystals. In contrast, when the pressure increased to 7 torr, the c-DBTTC nanoplates became thinner and larger, which could also be called as DBTTC flake (as shown in Figure 3.7C). Consequently, we are able to control the size and thickness of DBTTC nanoplates by varying the crystallization pressure.

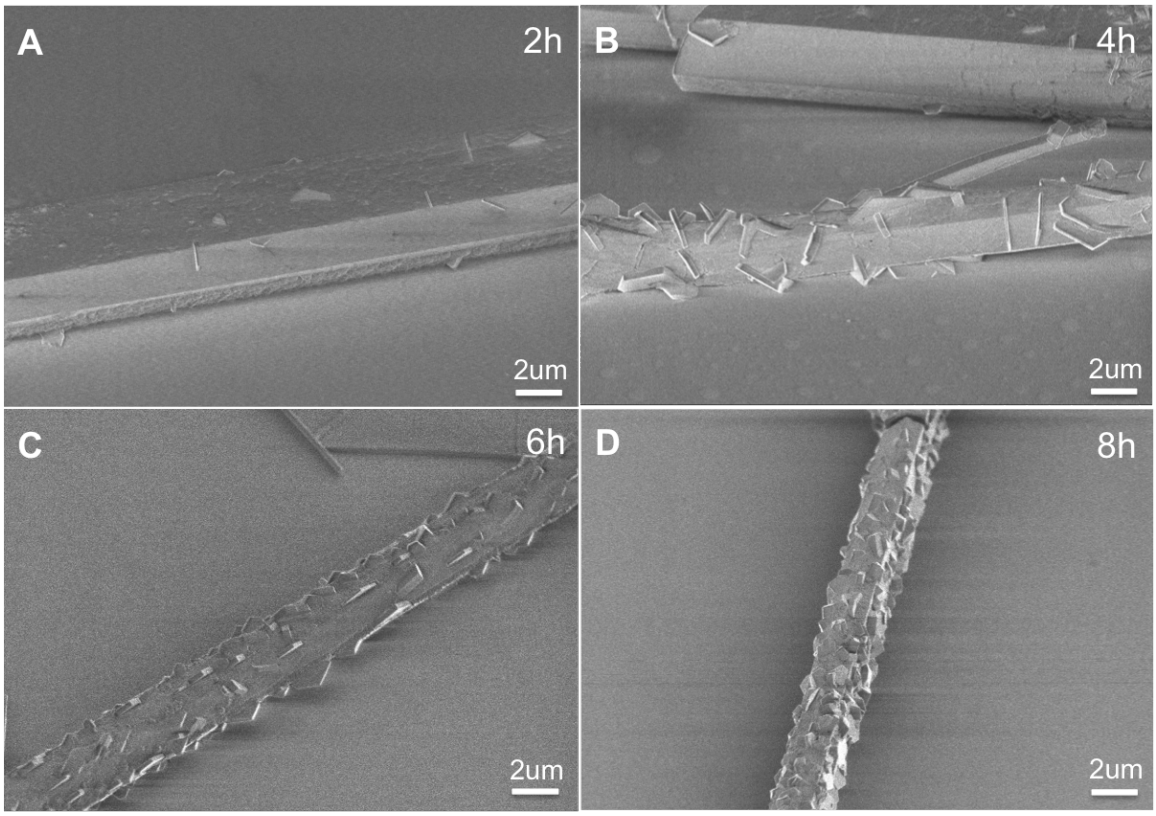

Figure 3.6: DBTTC grown on C_{60} needle crystals for different time at 205 ^{o}C under 6 torr: (A) 2h , (B) 4h, (C) 6h, (D) 8h. Scale bar: 2μm

From the above results, we demonstrated that c-DBTTC crystals could be selectively grown on C_{60} needle crystals using the vapor-phase synthesis method, which is due to the formation of ball-and socket interfaces between c-DBTTC and C_{60}. We also varied the crystallization conditions of c-DBTTC and found that the morphology and the amount of c-DBTTC crystals on the C_{60} crystal can be tuned.

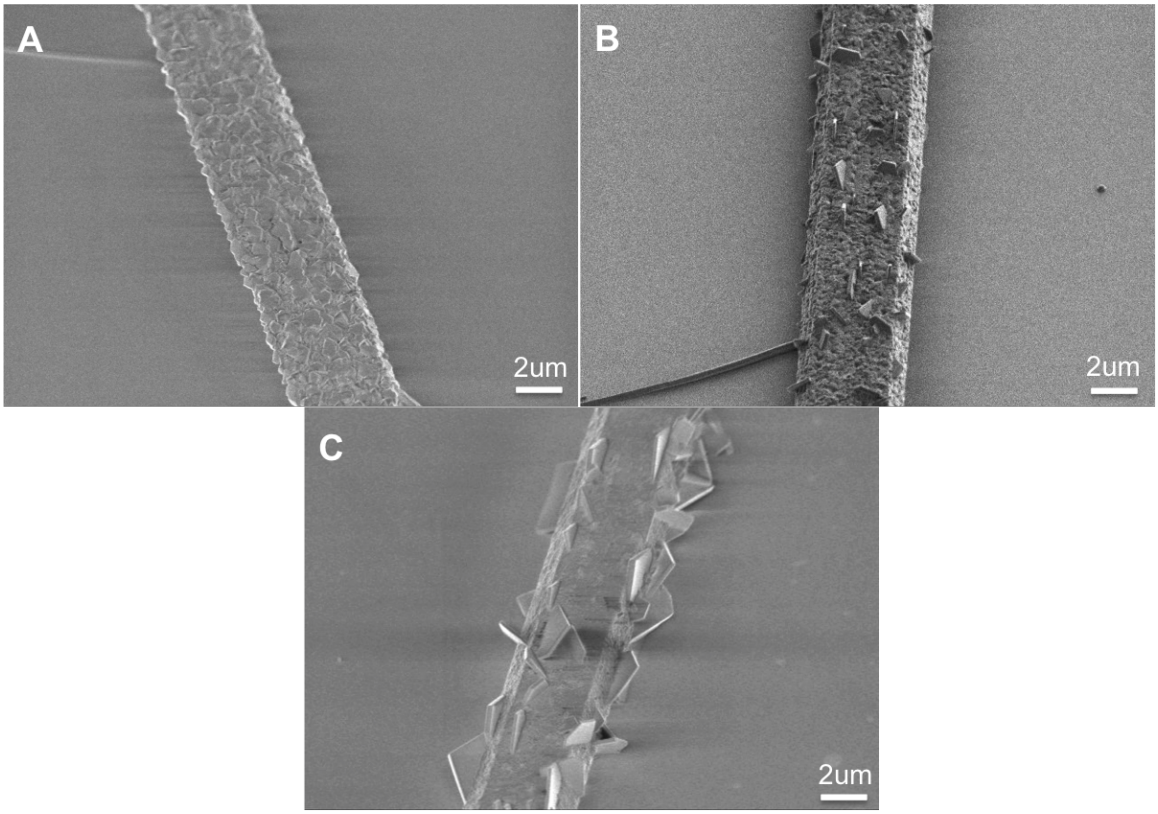

Figure 3.7: DBTTC grown on C_{60} needle crystals at different pressure at 165 ^{o}C: (A) 5 torr for 4h , (B) 6 torr for 6h, (C) 7 torr for 12h. Scale bar: 2μm

3.4 Raman spectrum of C_{60}-DBTTC heterostructure

To further confirm the formation of C_{60}-DBTTC heterojunction, we exploited the Raman microscope to obtain the vibration spectrum of the heterostructure with an excitation wavelength at 532nm. Firstly, we obtained the Raman spectrum of C_{60} crystals after annealing. From the spectrum (as shown in Figure 3.8A), we noticed that it has a strong peak at 1468 cm^{-1}, which corresponds to the $A_g(2)$ pentagonal pinch mode of C_{60}. [80] The slightly in-

clined baseline is due to the weak luminescence of C_{60} crystals.[145] Then we obtained the spectrum of c-DBTTC crystals (as shown in Figure 3.8B), it presents a strong vibration peak at 1344 cm^{-1}. Besides, the inclined baseline indicated that there is strong luminescence of DBTTC crystals. We then obtained the Raman spectrum of the C_{60}-DBTTC heterojunction (as shown in Figure 3.9A). From the spectrum, we observed the peak locating at 1468 cm^{-1}, which belongs to the C_{60} nanorods. And the peak at 1344 cm^{-1} belongs to c-DBTTC, which demonstrates the self-assembly of c-DBTTC crystals on the C_{60} crystal at nanoscale.

According to the above discussion, we knew that the 1344 cm^{-1} is the characterizing peak of c-DBTTC crystal and the strong 1468 cm^{-1} peak is attributed to C_{60} in the heterojunction (as shown in Figure 3.9 A). We then conducted a Raman mapping to investigate the distribution of c-DBTTC on C_{60}-DBTTC heterostructure. The dashed square in the microscope image (as shown in Figure 3.9B) showed area we selected to map. We first obtained the full spectra in the region shown in the Figure 3.9B). Then we extracted the intensity at 1468 cm^{-1} as a function of coordinates [X,Y] and plotted graph by setting the coordinates X and Y as horizontal and vertical axes, respectively, (as shown in Figure 3.9C). From the Figure 3.9C, we could clearly distinguish the location of the C_{60} crystal and the width of the nanorod is about 7 μm. Similarly, the Figure 3.9D is the graph showing the intensity at 1344 cm^{-1} as a function of coordinates [X, Y]. From the graph, we noticed that the distribution of c-DBTTC crystals overlaps with the C_{60} crystal, which demonstrating the selectively crystallization of c-DBTTC crystals by utilizing the C_{60} as nucleation sites. Moreover, the intensity of the vibration at 1344 cm^{-1} is not uniform, which indicates that the c-DBTTC was not evaporated on the C_{60} crystals but crystallized into single-crystals.

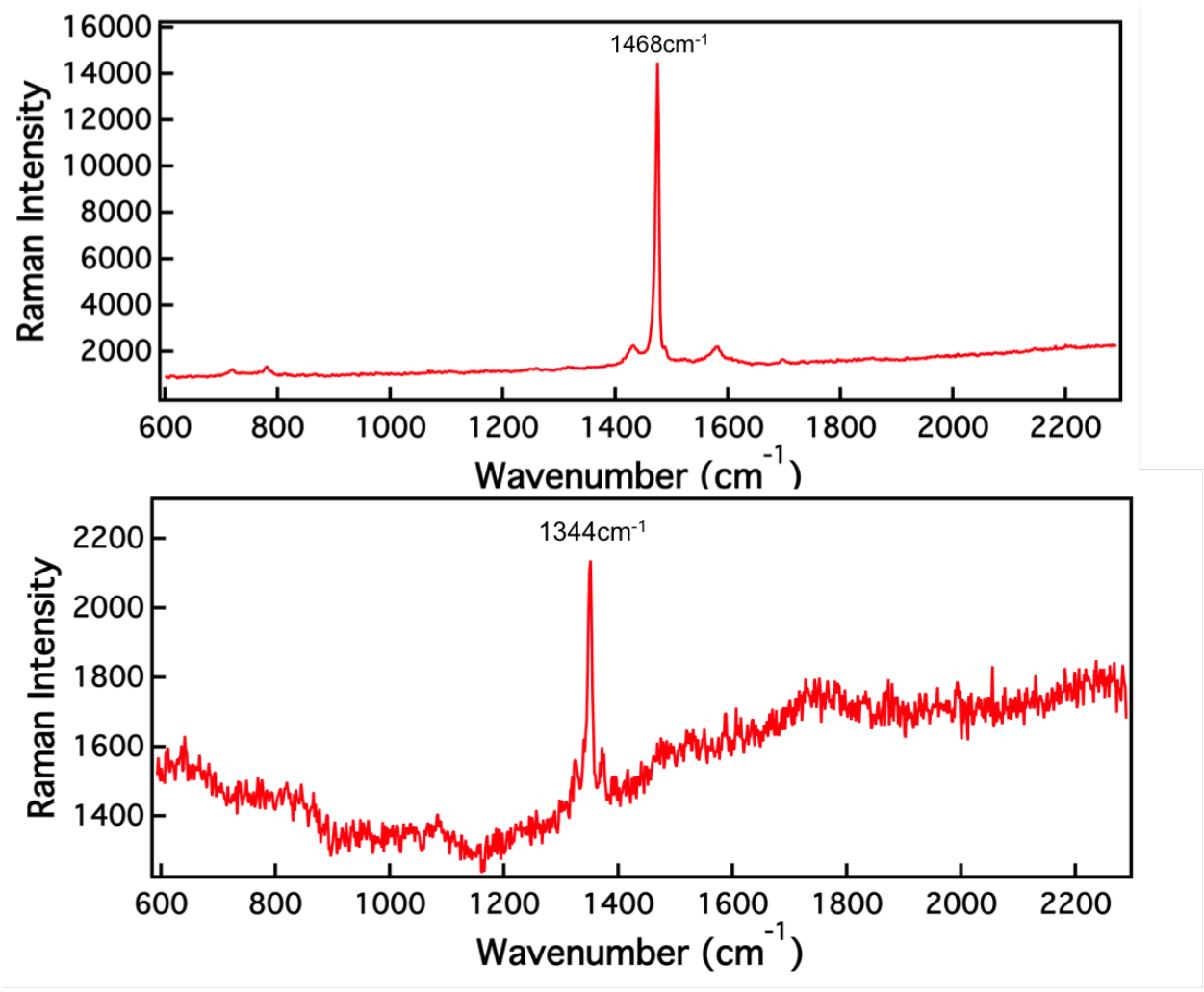

Figure 3.8: (A) Raman spectrum of C_{60} crystals (B) Raman spectrum of c-DBTTC crystals

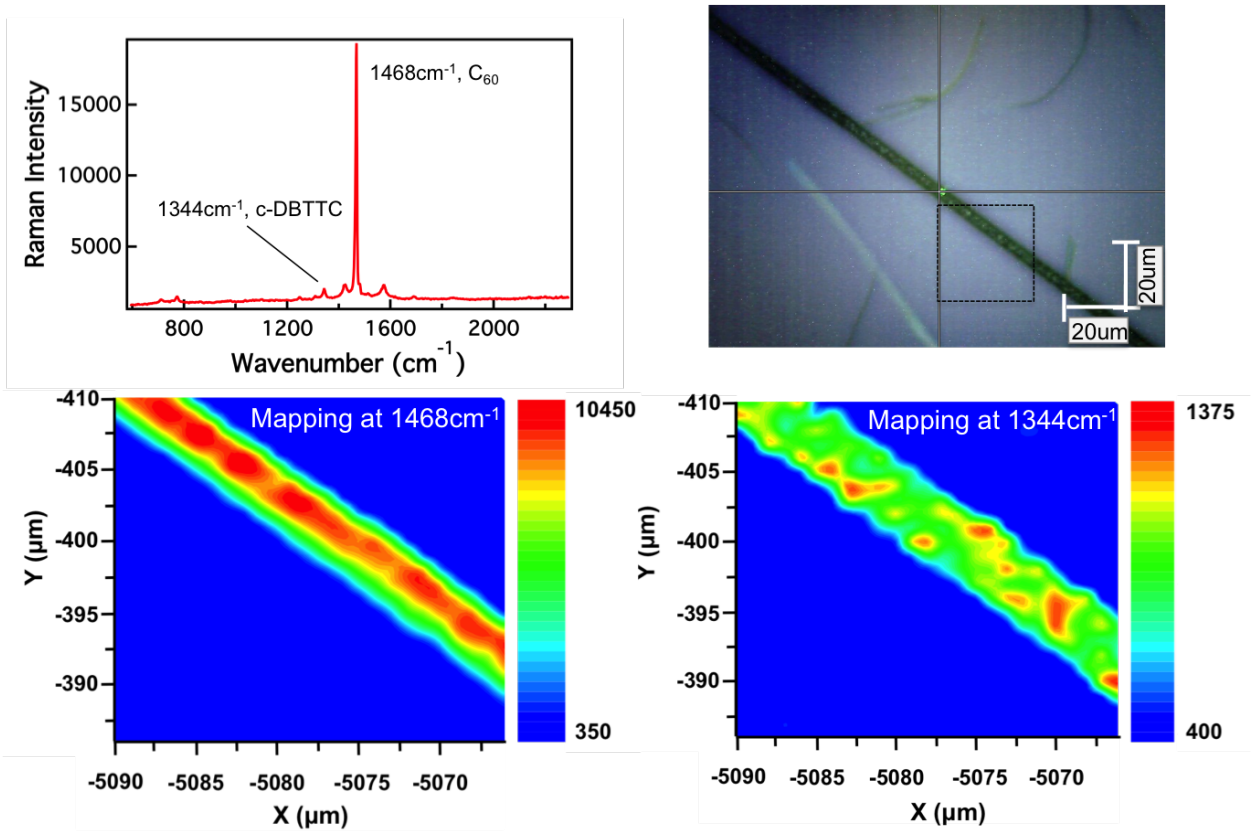

Figure 3.9: (A) Raman spectrum of C_{60}-DBTTC heterstructure (B) Microscope image of the C_{60}-DBTTC heterostructure for Raman mapping (C) Raman intensity at 1468cm^{-1} as a function of coordinates [X,Y] (D) Raman intensity at 1344cm^{-1} as a function of coordinates [X,Y].

3.5 Charge transport in C_{60}-DBTTC heterostructure

Having demonstrated the synthesis of C_{60}-DBTTC p-n heterojunctions, we then investigated if there is charge transport at the interface of p-n heterojunctions. Figure 3.10A shows energy diagrams of C_{60} and c-DBTTC.[143, 146] From energy diagrams, we knew the lowest unoccupied molecular orbital (LUMO) energy of c-DBTTC molecule is $\sim$ -2.3 eV and the LUMO energy of fullerene is $\sim$ -4.2 eV. So electrons excited to the LUMO level of c-DBTTC is possible to transfer to that of C_{60}. To verify the charge transport at C_{60}-DBTTC heterojunctions, we conducted the fluorescence microscopy experiment. As been mentioned above, the DBTTC showed strong luminescence upon excitation. If charge transfer happens at the interfaces, then the fluorescence intensity of the c-DBTTC would greatly reduce. We studied both heterostructures of c-DBTTC nanowires and nanoplates on C_{60} crystals (as shown by SEM images in Figure 3.10 B and D, respectively). When the c-DBTTC naonwires were assembled on the C_{60} crystal, the nanowires shows strong fluorescence upon excitation wavelength at 490nm (see Figure 3.10C), which demonstrated that c-DBTTC crystal is a strong fluorescent semiconductor and the charge transfer at the interfaces with C_{60} is not enough to quench the fluorescence. However, when we excited the c-DBTTC nanoplates/C_{60} crystals heterostructures with the same wavelength, we didn't observe any fluorescence in the region covered by the c-DBTTC nanoplates (see Figure 3.10E) , which means that the fluorescence of c-DBTTC nanoplates were fully quenched. This is because the electron in the HOMO level got excited to the LUMO level and then transferred to the LUMO level of C_{60} crystals. Consequently, the possibility of radiative transition were greatly reduced and the intensity of fluorescence was much weaker. The charge transport existing in the C_{60}-DBTTC

heterojunctions makes this heterostructure a potential candidate for opoelectronics.

3.6 Conclusion

This chapter described a novel organic single-crystal p-n heterojunction prepared by exploiting the ball-and-socket shape-complementarity between C_{60} and c-DBTTC molecules. By varying the crystallization conditions, *i.e.*, temperature, time and pressure, we are able to tune the morphology and amount of c-DBTTC crystals on the C_{60} crystal. Moreover, the Raman spectroscopy was used to verify the single-crystal synthesis of c-DBTTC on C_{60} crystals. We also demonstrated that there is charge-transport between C_{60} and c-DBTTC by observing the fluorescence quenching phenomenon of c-DBTTC. This unique C_{60}-DBTTC heterostructure is a promising candidate for photoelectric conversion.

3.7 Experimental section

3.7.1 C_{60} needle crystals growth

C_{60} needle crystals were grown using the modified droplet-pinned crystallization method reported by Li *et al.* Firstly, we dissolved the C_{60} powder (Sigma Aldrich) in m-xylene (Sigma Aldrich) with the sonicator to prepare 0.4mg/mL solution. Then we filtered the C_{60} solution with a microfilter and drop-casted 20 μL solution on to a cleaned 1×1 cm degenerately-doped silicon substrate with a 285-nm thermal silicon oxide layer with a 0.4×0.4 cm pinner in the center. The substrate was left overnight in a glass petri dish under ambient temperature and C_{60} needle crystals formed on the substrate. We placed the substrate with C_{60} needle

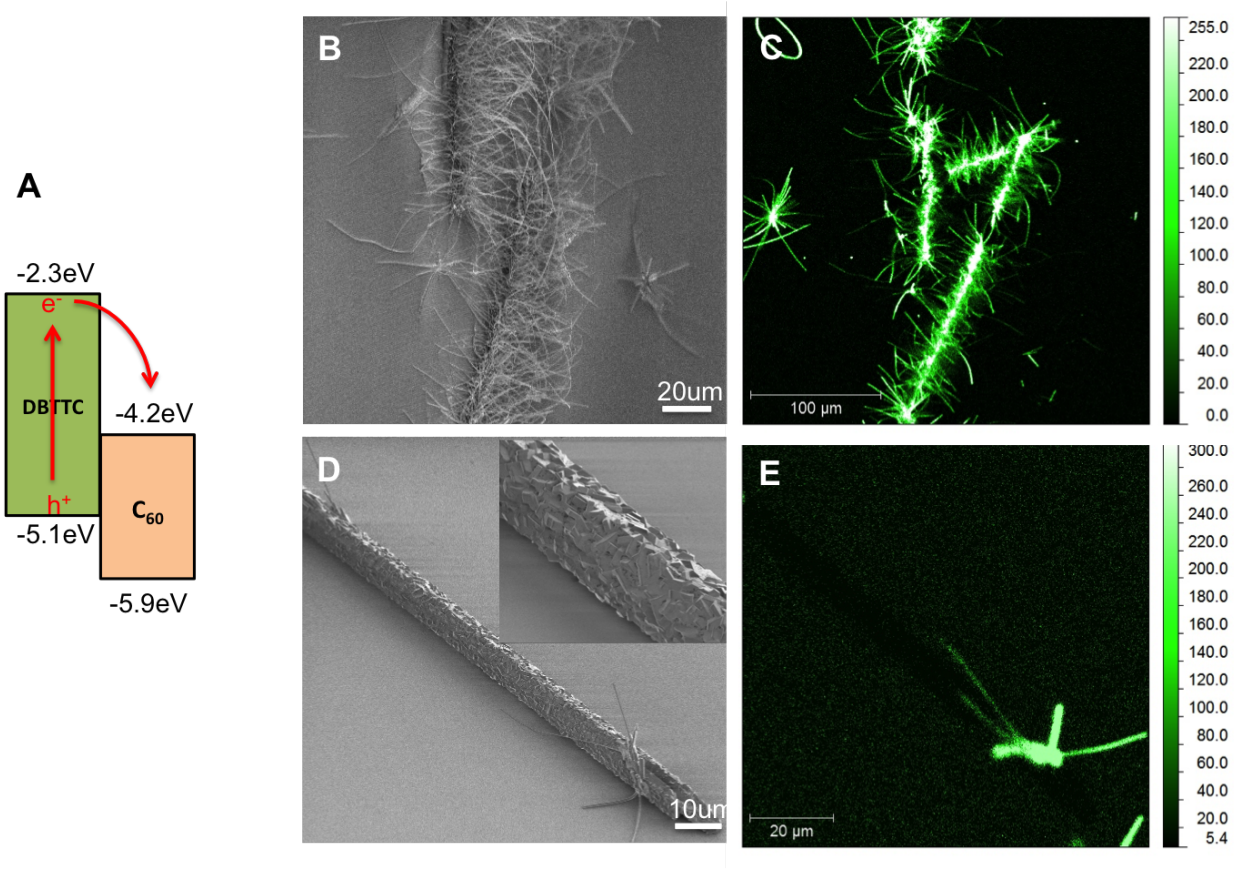

Figure 3.10: (A) The LUMO and HOMO energy of c-DBTTC are -2.3 eV and -5.1 eV; the LUMO and HOMO energy of C_{60} are -4.2 eV and -5.9 eV, which allows charge transfer between them. (B) SEM image of c-DBTTC nanowires on C_{60} crystal, scale bar: 10 μm (C) Fluorescence image of the same C_{60}-DBTTC heterostructure (B), scale bar: 20 μm (D) SEM image of c-DBTTC nanoplates on C_{60} crystal, scale bar: 20 μm. (E) Fluorescence image of the same C_{60}-DBTTC heterostructure (D), scale bar: 100 μm.

crystals in a tube furnace and heated up to 60 ^{o}C under vacuum (P: $\sim$ 460 mtorr) for 10h to remove the m-xylene in the C_{60} crystals.

3.7.2 c-DBTTC synthesis

The c-DBTTC molecule was synthesized by following previous work [76]. Briefly, the 6,13-pentacenequinone precursor reacted with triphenylphosphine and carbon tetrabromide via the Ramirez reaction to produced 1,1,8,8-tetrabromobisolefin. Then 1,1,8,8-tetrabromobisolefin reacted with 4,4,5,5-Tetramethyl-1,3,2-dioxaborolane yield bisolefin skeleton through Suzuki-Miyaura coupling reaction. The bisolefin skeleton was then photocyclized to produce DBTTC via the Katz-modified Mallory photocyclization.

3.7.3 Self-assembly of C_{60}-DBTTC heterojunction

The c-DBTTC crystals were selectively grown on C_{60} crystals from the gas phase using the physical vapor transport crystallization method. We first weighed 0.5mg c-DBTTC powder and placed in a boat at the center of the tube furnace. Then we placed the C_{60} on substrate in the downstream side of the tube furnace. The c-DBTTC crystallization was conducted under Ar flow and the pressure was adjusted to a desired value (5 torr, 6 torr, 7 torr) with a controllable gas valve. Then the furnace was heated up to 340 ^{o}C in 20 min and kept at 340 ^{o}C for a certain time (2h, 4h, 6h, 8h).

3.7.4 Characterization

The infrared spectra were obtained with the PerkinElmer FT-IR Spectrum 400. The SEM images were taken with the Hitachi s-4700 SEM. The fluorescence images were obtained with the Leica TCS SP5 confocal microscope. The Raman spectrum were conducted with the Renishaw inVia micro-Raman microscope.

Chapter 4

One-dimensional and two-dimensional Programming in Solid-State Assembly[1]

4.1 Introduction

This chapter describes a new series of macrocyclic dimers (Figure 4.1A) of superatoms synthesized from $Co_6Se_8(PEt_3)_4(CO)_2$ clusters and how the subtle differences in the coupling between them has drastic changes in the solid state assembly with electron acceptors. Superatoms have been exploited as nanoscale building blocks for solid-state materials [85–92], due to the merits of ready-preparation, and atomic-precision control. Besides, solid-state materials made from them exhibit emergent collective properties, such as unusual phononic [93], electronic [88], and magnetic properties [88, 89]. Moreover, the degree of tunability of the superatoms because of the large synthetic diversity available to them makes them attractive

[1]This work a collaborative work with Dr. Alexandra Velian.

components to be incorporated in solid-state materials. [90] For example, $Co_6Se_8(PR_3)_6$ is an electron rich cluster which has each of its cobalt sites associated with a phosphine ligand. [88] $Co_6Se_8(PR_3)_6$ in combination with electron acceptors, such as fullerene of similar size, can self-assembled into crystalline, solid-state materials that displays emergent electronic and magnetic properties.[88] In addition, a method to differentiate the position and the type of ligands that adorn the Co_6Se_8 superatom has been discovered and utilized to synthesize diatomic and triatomic superatom molecules.[94] This allows us to study, for the first time, how these unsymmetrically substituted building blocks will behave in the solid state. Here, we create and study a series of macrocyclic dimers (cis-$Co_6Se_8(PEt_3)_4[\mu$-$(Ph_2P)_2X]_2$ (**1**-$(Ph_2P)_2X$, X = NH, CH_2, C≡C, Figure 4.1B) that feature two superatoms formed into a macrocycle from a cis-disubstituted superatom precursor. We find that the linkers that bridges the two superatoms determine the distance and electronic coupling between the two superatoms in the macrocycle. The coupling is the strongest in **1**-$(Ph_2P)_2NH$ and the weakest in **1**-$(Ph_2P)_2C{\equiv}C$. With the charge transfer strategy introduced previously, we assembled the as-synthesized macrocyclic dimers into solid state materials with the well-known electron acceptor tetracyanoethylene (TCNE) [147–150]. We find that when the macrocyclic dimers used have the superatoms within their vdW radius, they form one-dimensional chains that assemble into layered materials. When the superatoms are separated so that the superatoms are now held outside of the vdW radius, two-dimensional sheet formed and they are held together by non-specific electrostatic attraction to form layered materials.

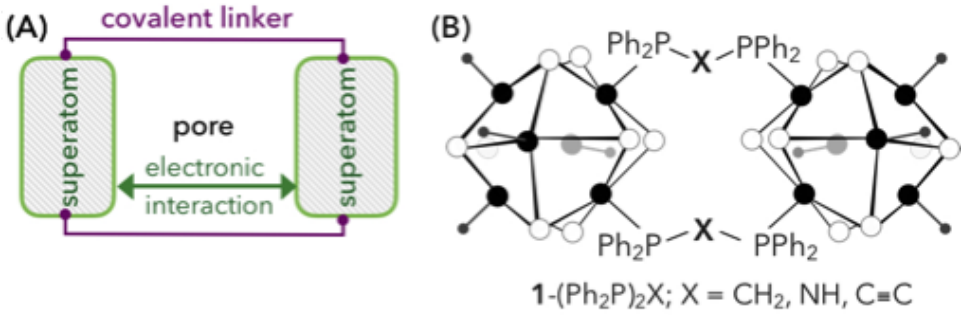

Figure 4.1: (A) Schematic of two superatoms in macrocycle where the distance and nature of the bridge determines the coupling between the subunits (B) Structure of superatom macrocycles cis-$Co_6Se_8(PEt_3)_4[\mu$-$(Ph_2P)_2X]_2$ (**1**-$(Ph_2P)_2X$; X = CH_2, NH, C≡C). Black filled circles: Co; hollow circles: Se; small grey filled circles: PEt3.

4.2 Synthesis of macrocyclic dimers

The three superatomic macrocycles **1**-$(Ph_2P)_2X$ were synthesized from the union of the "corner" unit cis-$Co_6Se_8(PEt_3)_4(CO)_2$ (**2**-CO) with the bidentate phosphine $(Ph_2P)_2X$ (X = CH_2, NH, C≡C) in a 1:1 molar ratio. Figure 4.2 shows the synthetic route of superatomic macrocycles and detail information for the preparation can be found in the Experimental Section. Briefly speaking, we first prepare the cis-$Co_6Se_8(PEt_3)_4[(Ph_2P)_2X]_2$ (**2**-$(Ph_2P)_2X$) clusters by irradiating a solution of **2**-CO (1 equiv) and $(Ph_2P)_2X$ (2 equiv) in THF (X = CH_2, C≡C) or toluene (X = NH) with a broadband UV lamp. Each of the dimers **1**-$(Ph_2P)_2X$ form after addition of another equivalent of **2**-CO to the as-synthesized crude reaction mixture and following further irradiation.

Figure 4.3 displays the unusual, macrocyclic structures of these as-synthesized dimers (**1**-

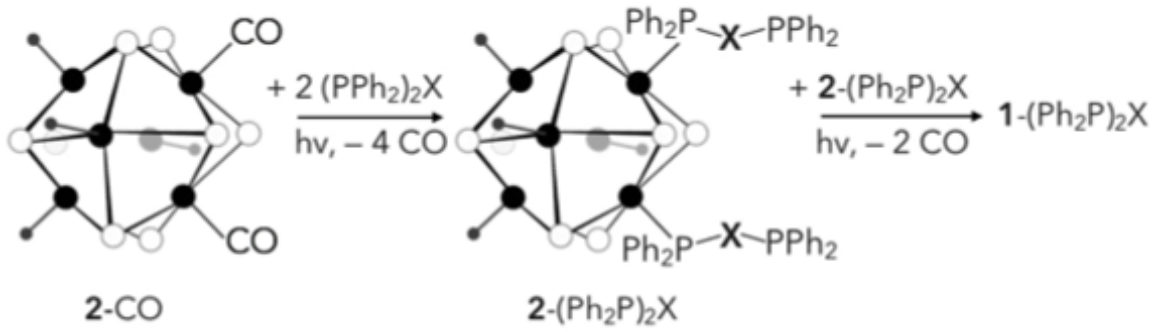

Figure 4.2: Synthetic route of the **1**-$(Ph_2P)_2X$ (X = CH_2, NH, C≡C) macrocycles from cis-$Co_6Se_8(PEt_3)_4(CO)_2$ (**2**-CO) and bidentate phosphine $(Ph_2P)_2X$.

$(Ph_2P)_2NH$, **1**-$(Ph_2P)_2CH_2$ and **1**-$(Ph_2P)_2C{\equiv}C$) by using the single crystal X-ray diffraction (SCXRD) analysis of their crystals, which were grown by vapor diffusion from toluene/n-pentane solutions. The bond lengths and angles within each superatom in the **1**-$(Ph_2P)_2X$ dimers are similar to those of monomeric $Co_6Se_8(PR_3)_6$ structures. Within the macrocycle, the two superatoms are brought very close to each other, with inter-superatom center-to-center distance values increasing in the series **1**-$(Ph_2P)_2NH$ (9.00 Å) < **1**-$(Ph_2P)_2CH_2$ (9.29 Å) < **1**-$(Ph_2P)_2C{\equiv}C$(10.20 Å). For comparison, the inter-superatom center-to-center separation in crystals of monomeric Co_6Se_8 clusters has a minimum value of 11.89 Å in $Co_6Se_8(PEt_3)_6$, and 14.23 Å in $Co_6Se_8(PPh_3)_6$, respectively.

An important finding for these macrocycle dimers is the transannular distances between the two pairs of selenium atoms that lie inside of the macrocyclic. From the data, we found that the transannular Se to Se distances are as short as 3.9 Å in **1**-$(Ph_2P)_2NH$ and 4.2 Å in **1**-$(Ph_2P)_2CH_2$. As a comparison, the sum of the van der Waals (vdW) radii of two selenium atoms is 4.0 Å. This transition of the transannular Se to Se distance in the macrocycles

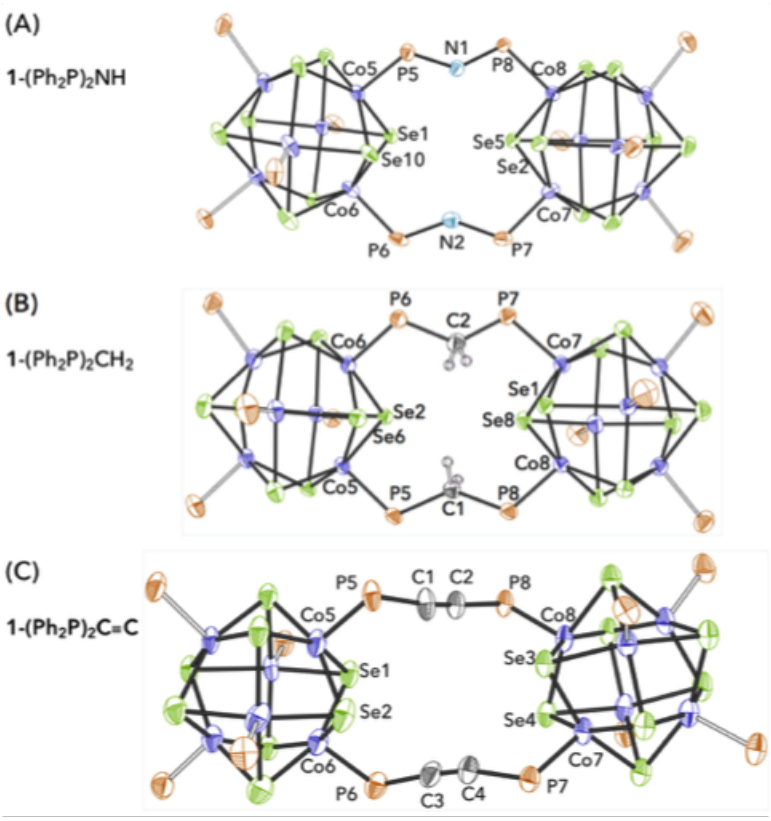

Figure 4.3: Solid-state structures of cis-$Co_6Se_8(PEt_3)_4[\mu$-$(Ph_2P)_2NH]_2$ (A, **1**-$(Ph_2P)_2NH$), cis-$Co_6Se_8(PEt_3)_4$ $[\mu$-$(Ph_2P)_2CH_2]_2$ (B, **1**-$(Ph_2P)_2CH_2$) and cis-$Co_6Se_8(PEt_3)_4[\mu$-$(Ph_2P)_2C_2]_2$ (C, **1**-$(Ph_2P)_2C{\equiv}C$) shown with 50% probability thermal ellipsoids. Ethyl and phenyl groups on the phosphorus atoms and solvent molecules are omitted for clarity; protons on N1 and N2 are also not represented.

being shorter than the vdW radii of two selenium atoms to longer than the vdW radii of two selenium atoms is of great importance. When the transannular Se to Se distance in the macrocycles is shorter than the vdW radii of two selenium atoms, the two superatoms could interact electronically in **1**-$(Ph_2P)_2NH$ due to their proximity. And the closer contact, therefore the stronger interactions between the superatoms in **1**-$(Ph_2P)_2NH$, as compared to **1**-$(Ph_2P)_2CH_2$. The difference in the distance being just inside and outsider the vdW radii raises an important point about how this transannular communication would be felt in charge transfer and self-assembly with electron acceptors.

4.3 Probing electronic interaction in macrocyclic dimers

We then carried out the cyclic voltammetry (CV) to probe the electronic interaction in these three macrocyclic dimers. As shown in Figure 4.4, the obtained results supported the assumption that electron communication between the superatoms in **1**-$(Ph_2P)_2NH$ is stronger than **1**-$(Ph_2P)_2CH_2$, which in turn is stronger than in **1**-$(Ph_2P)_2C{\equiv}C$. As a point of comparison, we also conducted the CV measurement of a "monomer" [approximated by **2**-$(Ph_2P)_2C{\equiv}C$], which displays three reversible, one-electron oxidations. In contrast, all of these three macrocyclic dimers display two pairs of sequential one-electron oxidation processes followed by two broad oxidation events. The splitting in potentials within each pair is the highest when removing the first two electrons from the neutral **1**-$(Ph_2P)_2X$ species (ΔE_1). From the Figure Figure 4.4, the largest splitting in the redox potentials of the two superatoms, which indicates that the clusters are electrically interacting most strongly in **1**-$(Ph_2P)_2NH$.

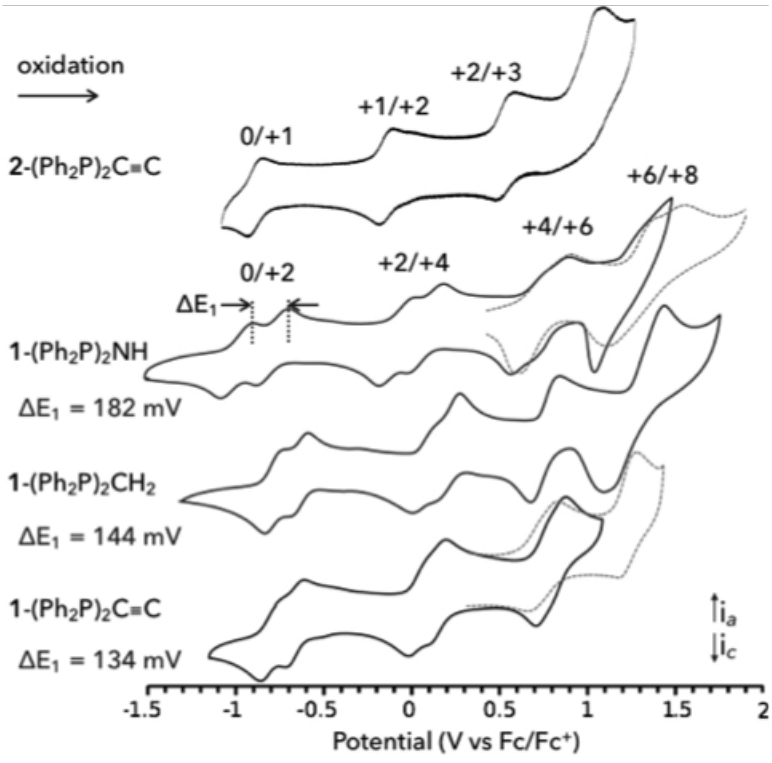

Figure 4.4: Top to bottom: Cyclic voltamograms of **2**-$(Ph_2P)_2C{\equiv}C$, **1**-$(Ph_2P)_2NH$, **1**-$(Ph_2P)_2CH_2$ and **1**-$(Ph_2P)_2C{\equiv}C$, respectively acquired in 0.1 M [TBA][PF6] in DCM solutions and scanned cathodically at 100 mV/s. The dotted grey traces overlaid on the cyclic voltamograms of **1**-$(Ph_2P)_2NH$ and **1**-$(Ph_2P)_2C{\equiv}C$ are scans acquired under identical conditions, but over a different scan window that allows the fourth oxidation event to be better resolved. Defined on the spectrum of **1**-$(Ph_2P)_2NH$ is ΔE_1, the splitting in potentials within the first pair of oxidation events.

4.4 Charge-transfer solid-state materials formed from macrocyclic dimers and TCNE

Having studied the electronic interaction in different macrocyclic dimers, we started to investigate how the difference in transannular communication is going to affect the self-assembly of them with electron acceptors. We selected the TCNE as the electron acceptor and grew co-crystals with the macrocyclic dimers **1**-$(Ph_2P)_2NH$ and **1**-$(Ph_2P)_2CH_2$. All of the growth was conducted under the same conditions with a stoichiometry 1 : 2 (superatom macrocycle: TCNE). We found that the macrocycle dimers are doubly oxidized. From the infrared spectra (see Figure 4.5), we found that both [**1**-$(Ph_2P)_2NH$]·$[TCNE]_2$ and [**1**-$(Ph_2P)_2CH_2$]·$[TCNE]_2$ show two peaks locating at 2183 cm^{-1} and 2144 cm^{-1}, which indicates that each TCNE has accepted one electron. [151, 152] Then we conducted the SCXRD experiment to get the crystal structure of **1**-$(Ph_2P)_2NH$ and **1**-$(Ph_2P)_2CH_2$ with TCNE to see the direct effect of the coupling between superatoms.

Figure 4.6 and 4.7 presented the structures of [**1**-$(Ph_2P)_2CH_2$]·$[TCNE]_2$ and [**1**-$(Ph_2P)_2NH$]·$[TCNE]_2$, respectively. For [**1**-$(Ph_2P)_2CH_2$]·$[TCNE]_2$, the structure is comprised of stacked, diamagnetic TCNE dimers and the superatom macrocycles in a two-dimensional rectangular arrangement that measures 2.4 nm × 1.3 nm (Figure 4.6). The TCNE radical anion, diamagnetic dimers are interacting with each other very strongly (they are 3.2 Å apart), but they are rotationally disordered. These two-dimensional sheets then stack into a layered material with the TCNE dimers eclipsing the opening in macrocycles of the next layer. There are no close interactions between the TCNE and superatom macrocycles

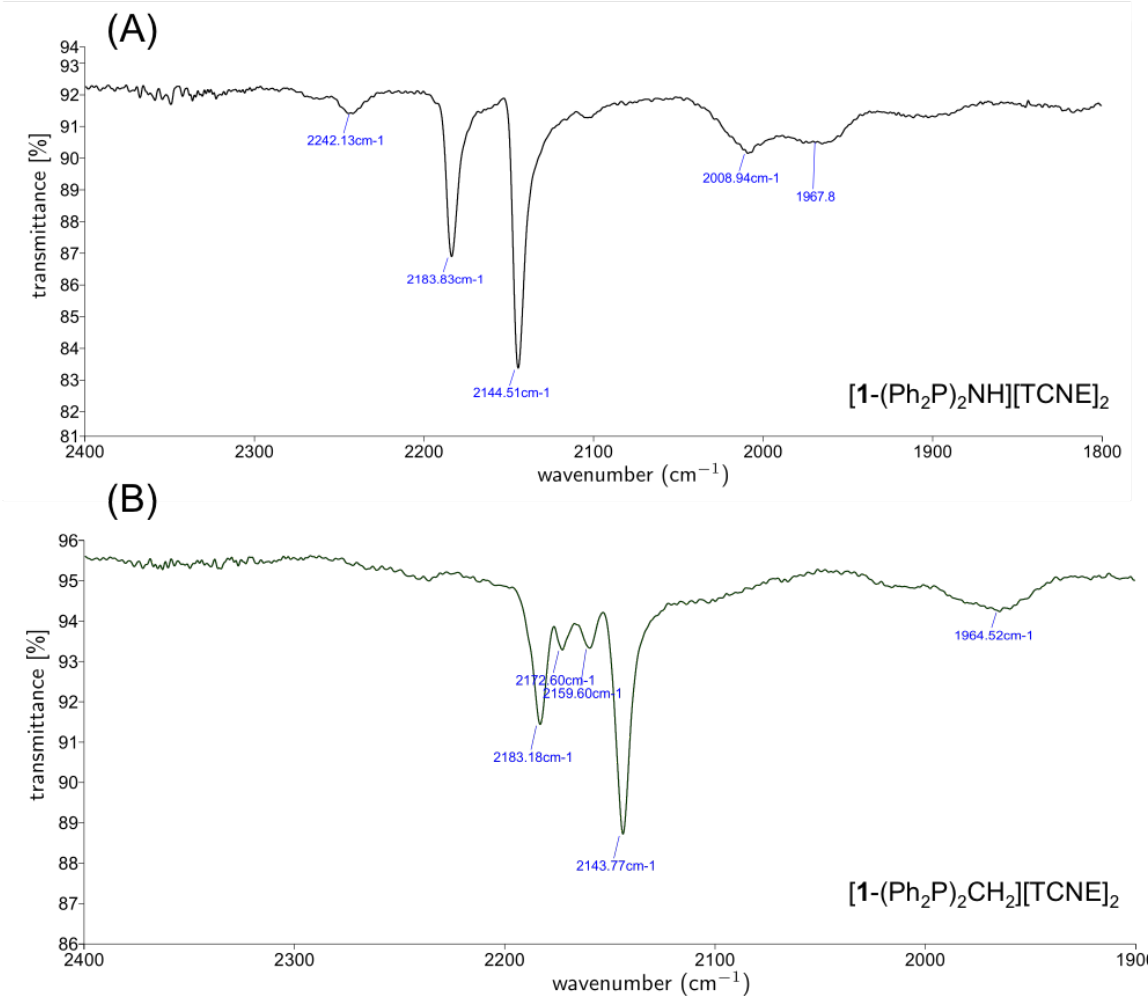

Figure 4.5: (A) IR spectrum of crystalline [**1**-$(Ph_2P)_2NH$]·$[TCNE]_2$ (B)[**1**-$(Ph_2P)_2CH_2$]·$[TCNE]_2$. Two peaks locating at 2183 cm^{-1} and 2144 cm^{-1} in both spectra indicates that each TCNE has accepted one electron.

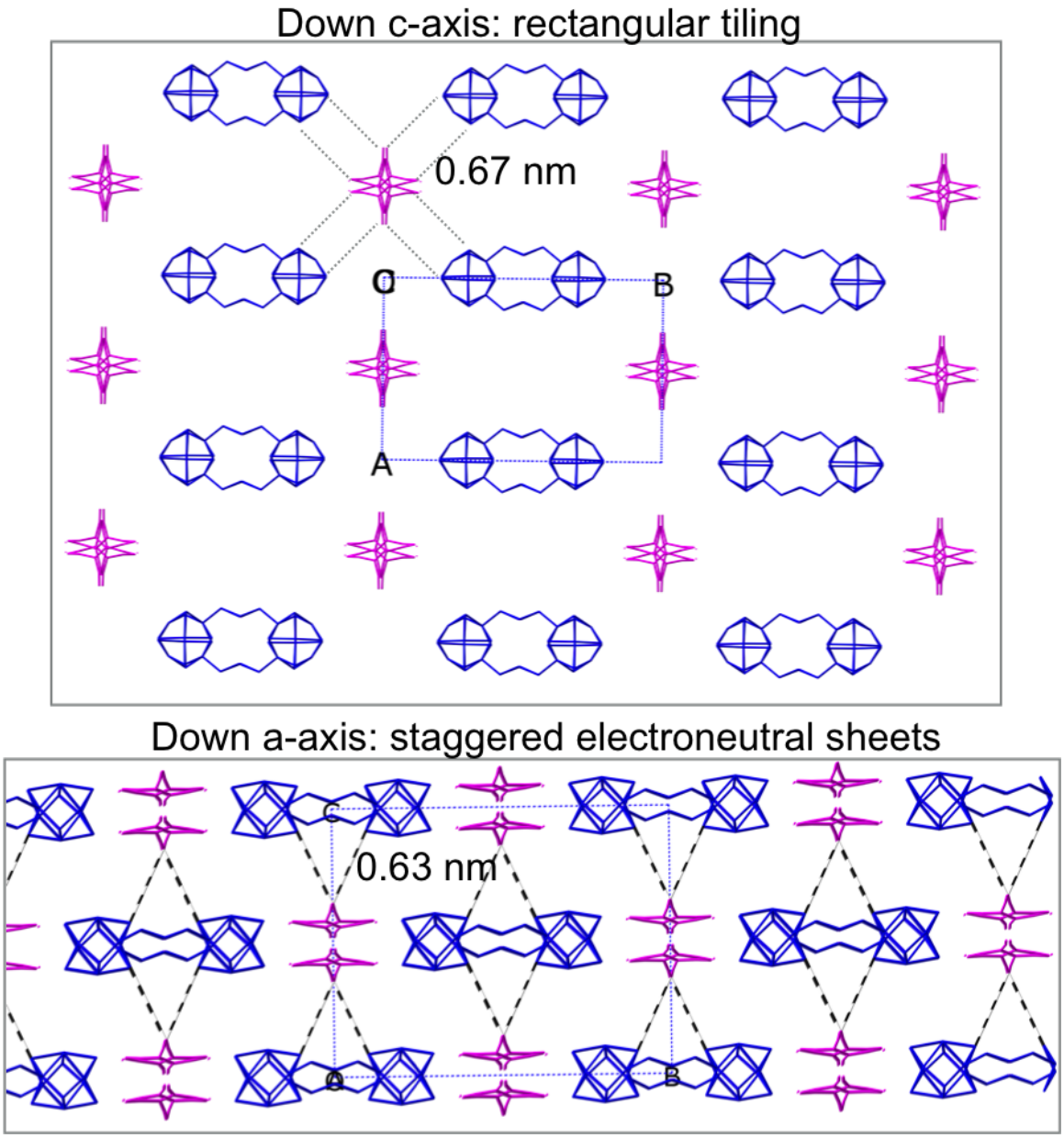

Figure 4.6: Crystal structure of [**1**-$(Ph_2P)_2CH_2$]·$[TCNE]_2$ in different views: down c-axis (top) and down a-axis (bottom). Solid-state materials assembled through stacking of two-dimensional sheets forms when **1**-$(Ph_2P)_2CH_2$ and 2 × TCNE were mixed to prepare the co-crystals.

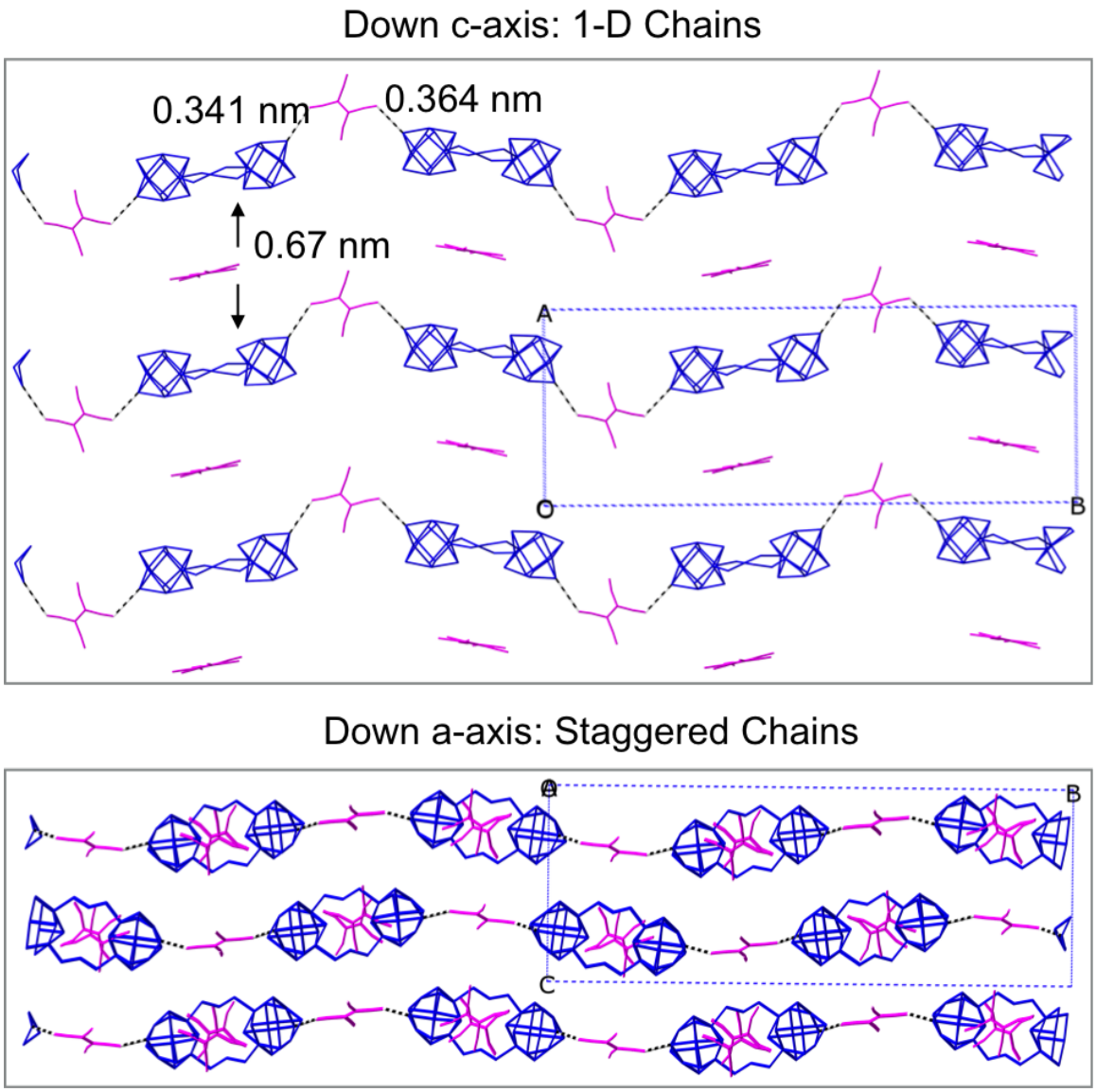

Figure 4.7: Crystal structure of [**1**-$(Ph_2P)_2NH$]·$[TCNE]_2$ in different views: down c-axis (top) and down a-axis (bottom). Layered materials assembled from one-dimensional chain forms when **1**-$(Ph_2P)_2NH$ and 2 × TCNE were mixed to prepare the co-crystals.

and thus the communication between the components is non-specific electrostatic attraction between the charged components. [**1**-$(Ph_2P)_2CH_2$]·$[TCNE]_2$ can be thought out as a rectangular reservoir of electrons that facilitates the charge transfer and its shape then dictates the symmetry of the resulting assembly.

The assembly changes when the macrocyclic dimer **1**-$(Ph_2P)_2NH$ is used in the assembly. Again, a two-dimensional arrangement of two TCNE radial anions and the macrocycles forms (Figure 4.7). However, now there is no TCNE dimer present and two crystallographically distinct TCNEs exist in the unit cell. One of them is disordered and is in the same general location as the TCNE dimer in [**1**-$(Ph_2P)_2CH_2$]·$[TCNE]_2$ (Figure 4.7). The other TCNE is crystallographically well-defined and is serving an important function by bridging between superatom macrocycles. There are close contracts ($\sim$ 3.6 Å) between the nitrogen atoms of the TCNE and the terminal selenium atoms of **1**-$(Ph_2P)_2NH$. The two TCNE molecules in the solid state are orthogonal to each other and therefore the material should have a magnetic moment. We hypothesize that the stronger coupling between the superatoms in **1**-$(Ph_2P)_2NH$ allows it to express itself as a one-dimensional electronic object with delocalization along its long axis. Besides, the 1-D chains should have significant electron mobility along this axis.

4.5 Conductivity of self-assembled solid salts

From the above discussion, we knew that **1**-$(Ph_2P)_2CH_2$ and **1**-$(Ph_2P)_2NH$ macrocyclic dimer self-assembled into different solid-state materials with TCNE. Now we turns to the conductivity study of these two solid-state materials. We first prepared thin films from

spin-coating the mixture of macrocyclic dimers and TCNE and then conducted the two-probe electric measurement on the thin films after depositing the electrodes. As shown in Figure 4.8A, the film made from [**1**-$(Ph_2P)_2NH$]·$[TCNE]_2$ showed higher conductance than that of [**1**-$(Ph_2P)_2CH_2$]·$[TCNE]_2$. The close interaction between the donor and the acceptors observed in the 1D chains correlates well with the increase in electron transport observed in the thin film measurements. We also studied the annealing effect on resistivity of the film. As shown in Figure 4.8B, annealing reduced the resistivity of both thin film devices due to higher crystalline degree with higher annealing temperature. In order to verify that the difference in the resistivity comes from the intrinsic properties of the solid-state materials not from the contact resistance difference between the materials and the metal contacts, we measured the dependence of conductivity on channel length. From the Figure 4.8 C and D, we can see that both of them showed negligible contact resistance compared with the film resistivity. As a consequence, we have demonstrated that the conductivity difference results from the channel materials, which in turn is due to the difference in their crystal structures.

4.6 Conclusion

This chapter describes a new series of macrocyclic dimers made from the $Co_6Se_8(PEt_3)_4(CO)_2$ clusters. They could be further used to assemble solid-state materials with electron acceptor TCNE. We find that when the macrocyclic dimers used have the superatoms within their vdW radius, they form one-dimensional chains that assemble into layered materials. When the superatoms are separated so that the superatoms are now held outside of the vdW radius, two-dimensional sheet formed and they are held

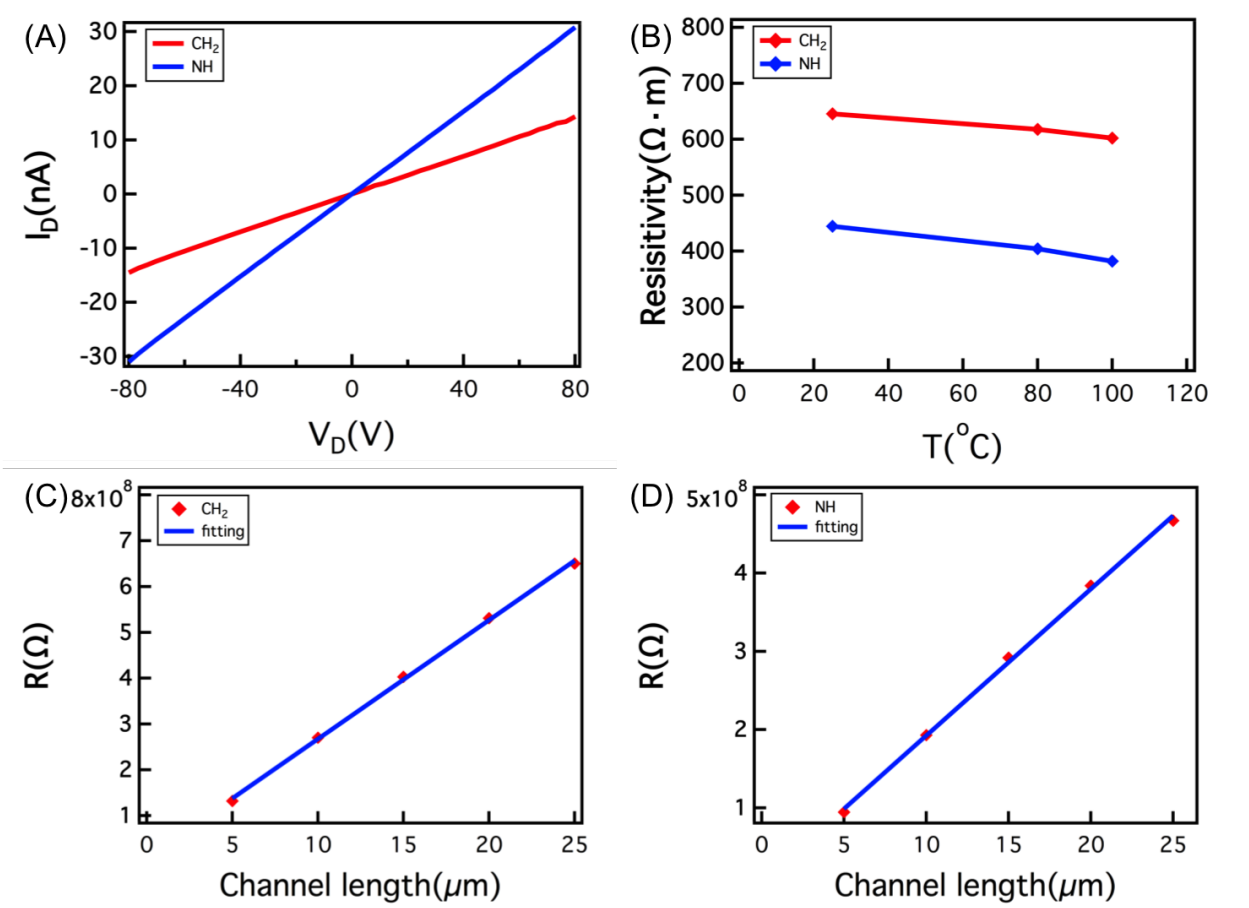

Figure 4.8: (A) Current versus bias voltage measurement of the thin film devices made from [**1**-$(Ph_2P)_2CH_2$]·$[TCNE]_2$ and [**1**-$(Ph_2P)_2NH$]·$[TCNE]_2$. (B) Resistivity of the thin film devices annealed at different temperature. (C) Dependence of the resistance of [**1**-$(Ph_2P)_2CH_2$]·$[TCNE]_2$ thin film devices on the channel length. (D)Dependence of the resistance of [**1**-$(Ph_2P)_2NH$]·$[TCNE]_2$ thin film devices on the channel length.

together by non-specific electrostatic attraction to form layered materials. The remarking finding is due to the subtle differences in the interaction between the superatoms conferred by the nature of the bridging group and the coupling between the subunits.

4.7 Experimental section

4.7.1 General experiment information

Unless otherwise noted, all reactions were performed in a nitrogen atmosphere using standard Schlenk techniques or in a nitrogen-filled glovebox. Anhydrous and anaerobic solvents were obtained from a Glass Contour solvent system consisting of a Schlenk manifold with purification columns packed with activated alumina and supported copper catalyst. cis-$Co_6Se_8(PEt_3)_4(CO)_2$ (**2**-CO) was prepared according to the literature procedure. [94] $Co_2(CO)_8$ (stabilized with 1-5% hexanes) and $(Ph_2P)_2NH$ (N, N-bis(diphenylphosphino) amine, 98%) were acquired from Strem Chemicals, PEt_3 (Et = ethyl, 99%), $(Ph_2P)_2CH_2$ (bis(diphenylphosphino) methane, 97%) and $(Ph_2P)_2C_2$ (bis(diphenylphosphino) acetylene, 98%) were purchased from Aldrich, and used without further purification.The photochemical reactor lamp was purchased from Hanovia Specialty lighting LLC (Catalog number PC 451.050). The lamp is a medium-pressure mercury lamp emitting 200-400 nm broadband radiation. The lamp was placed inside a quartz jacket, with cooling water circulating throughout to maintain the reactions at ambient temperature. The Quartz reaction flasks were purchased form Aldrich. Electrochemistry was performed in a nitrogen filled glovebox using a CH166 electrochemical workstation using a glassy carbon working electrode, a plat-

inum wire counter electrode, and a silver wire pseudo-reference purchased from BASI. All scans were referenced to ferrocene, which was added at the end of each measurement set.

4.7.2 Synthesis of cis-$Co_6Se_8(PEt_3)_4[\mu$-$(Ph_2P)_2CH_2]_2$ (1-$(Ph_2P)_2CH_2$)

Solid **2**-CO (200 mg, 0.146 mmol, 1 equiv), $(Ph_2P)_2CH_2$ (112 mg, 0.291 mmol, 2 equiv), tetrahydrofuran (THF, 40 mL) and a magnetic stirbar were charged in a 100 mL Quartz round-bottom flask. The flask was capped with a vacuum adapter, degassed and the green-brown solution was irradiated with a broadband UV-vis lamp for 8 h. The volatile materials were removed under reduced pressure from the reaction mixture, and the flask was brought inside the glovebox where the residue was triturated with n-pentane (2 × 5 mL). The volatile materials were removed under reduced pressure from the mixture, and the residue was identified as **2**-$(Ph_2P)_2CH_2$ by spectroscopic methods (90% pure by spectroscopic analysis). **2**-$(Ph_2P)_2CH_2$ can be crystallized from neat n-pentane, at room temperature.

Crude **2**-$(Ph_2P)_2CH_2$ (all the material obtained as described above; ca. 295 mg), **2**-CO (200 mg, 0.146 mmol, 1 equiv), THF (60 mL) and a magnetic stirbar were charged in a 100 mL Quartz round-bottom flask. The flask was capped with a vacuum adapter, degassed and the green-brown solution was irradiated with a broadband UV-vis lamp for 15 to 24 h. The volatile materials were removed under reduced pressure from the reaction mixture, and the flask was brought inside the glovebox where the residue was triturated with n-pentane (3 × 5 mL) until it became powdery. The solids were then extracted with n-pentane (3 × 5 mL) and diethyl ether (3 × 5 mL) to remove any soluble intermediate

products [the diethyl ether fraction can be collected and reset for photolysis to produce the desired product]. The brick-red residue was dissolved in dichloromethane, then it was passed through a Celite plug to remove any insoluble materials. The filtrate was brought to constant mass and identified as spectroscopically clean **1**-$(Ph_2P)_2CH_2$ (200 mg, 0.054 mmol, 37%). **1**-$(Ph_2P)_2CH_2$ crystallizes from toluene/n-pentane mixtures at -35 ^oC, in the glovebox fridge.

4.7.3 Synthesis of cis-$Co_6Se_8(PEt_3)_4[\mu$-$(Ph_2P)_2NH]_2$ (1-$(Ph_2P)_2NH$)

Solid **2**-CO (200 mg, 0.146 mmol, 1 equiv), $(Ph_2P)_2NH$ (112 mg, 0.292 mmol, 2 equiv), toluene (50 mL) and a magnetic stirbar were charged in a 100 mL Quartz round-bottom flask. The flask was capped with a vacuum adapter, degassed and the green-brown solution was irradiated with a broadband UV-vis lamp for 8 h during which time the reaction color changed from the initial green-brown to deep red. The reaction mixture was then degassed and brought inside the glovebox where **2**-CO (200 mg, 0.146 mmol, 1 equiv) was added with the aid of toluene (10 mL). The flask was capped with a vacuum adapter, degassed and the green-brown solution was irradiated with a broadband UV-vis lamp for 15 to 24 h, until the reaction was completed. The volatile materials were removed under reduced pressure from the reaction mixture, and the flask was brought inside the glovebox where the residue was triturated with n-pentane (3 $\times$ 10 mL) until it became powdery. The brick-red solid was then extracted with n-pentane (3 $\times$ 5 mL) and diethyl ether (4 $\times$ 5 mL) to remove any soluble intermediate products [the diethyl ether fraction can be collected and

reset for photolysis to produce the desired product]. The resulting powder was dissolved in dichloromethane, passed through a Celite plug to remove any insoluble materials, brought to constant mass and identified as spectroscopically pure **1**-$(Ph_2P)_2NH$ (205 mg, 0.054 mmol, 38%). The diethyl ether fraction was cooled to -35 ^oC, and a second crop of **1**-$(Ph_2P)_2NH$ was collected (60 mg, 0.017 mmol; combined yield 49%). **1**-$(Ph_2P)_2NH$ crystallizes from toluene/n-pentane mixtures at -35 ^oC, in the glovebox fridge.

4.7.4 Synthesis of cis-$Co_6Se_8(PEt_3)_4[\mu$-$(Ph_2P)_2C_2]_2$ (**1**-$(Ph_2P)_2C{\equiv}C$)

Solid **2**-CO (200 mg, 0.146 mmol, 1 equiv), $(Ph_2P)_2C_2$ (115 mg, 0.292 mmol, 2 equiv), THF (40 mL) and a magnetic stirbar were charged in a 100 mL Quartz round-bottom flask. The flask was capped with a vacuum adapter, degassed and the green-brown solution was irradiated with a broadband UV-vis lamp for 8 h during which time the reaction color changed from the initial green-brown to deep red. From this crude solution, **2**-$(Ph_2P)_2C{\equiv}C$ can be purified by removing the volatile materials and crystallization from a saturated solution in n-pentane, at room temperature. To synthesize the dimer **2**-CO, the crude reaction mixture obtained after the photolysis of **2**-CO with $(Ph_2P)_2C_2$ was degassed and brought inside the glovebox where **2**-CO (200 mg, 0.146 mmol, 1 equiv) was added with the aid of THF (20 mL). The flask was capped with a vacuum adapter, degassed and the green-brown solution was irradiated with a broadband UV-vis lamp for 15 to 20 h. The volatile materials were removed under reduced pressure from the reaction mixture, and the flask was brought inside the glovebox. The residue was triturated with with n-pentane (3 $\times$ 10 mL) until it became

like a powder upon removing the volatile materials. Next, this material was extracted with n-pentane (15 mL), then with diethyl ether (3 × 5 mL). The resulting brick-red powder was dissolved in dichloromethane, passed through a Celite plug to remove any insoluble materials and identified as spectroscopically clean **2**-CO (185 mg, 0.050 mmol, 34%). **2**-CO can be crystallized from toluene/n-pentane mixture at -35 ^{o}C, inside the glovebox fridge.

4.7.5 Synthesis of cis-$Co_6Se_8(PEt_3)_4[\mu$-$(Ph_2P)_2X]_2[TCNE]_2$ ($[$**1**-$(Ph_2P)_2X][TCNE]_2$)

To a dark red solution of **1**-$(Ph_2P)_2X$ (0.027 mmol, 1 equiv) in toluene (5 mL) was added a solution of TCNE (0.054 mmol, 2 equiv) in toluene (2 mL) effecting the immediate formation of a precipitate. The resulting mixture was stirred at room temperature and after 3 h the precipitate was collected on a sintered frit, and then set to crystallize from dichloromethane/diethyl ether (ca. 4 mL/15mL) at room temperature. Dark block (for X = CH_2) or needle (for X = NH or C≡C) crystals of $[$**1**-$(Ph_2P)_2X][TCNE]_2$ (isolated yields avg. 95%) were collected on a frit by vacuum filtration after 20 h.

4.7.6 Electrical Measurement

The thin film of $[$**1**-$(Ph_2P)_2NH]\cdot[TCNE]_2$ and $[$**1**-$(Ph_2P)_2CH_2]\cdot[TCNE]_2$ were prepared by spin-coating their chloroform solution on a Si/SiO_2 wafer with a spin speed of 3000 rmp for 1min in the glovebox. Then TEM grids were transferred to the substrates, which were transferred into the deposition chamber for silver deposition. Annealing at different temperatures was carried out by placing the substrate on the hot plate for 15min.To calculate

the conductivity, we used the atomic force microscope to obtain the thickness of the film. For the channel length dependence experiment, we first used the standard e-beam lithography technique to deposit the electrode pattern on the Si/SiO_2 substrate. Then we use the pentafluorobenzenethiol to modify the gold electrodes. Finally, we spin-coated the solution containing **1**-$(Ph_2P)_2NH{\cdot}TCNE_2$ and [**1**-$(Ph_2P)_2CH_2$]$\cdot$[TCNE]$_2$ onto pre-patterned substrates.

Bibliography

[1] G Moore, Electronics **38**, 114 (1965).

[2] M. M. Waldrop, Nature **530**, 144 (2016).

[3] T Ashley, A. Dean, C. Elliott, A. Johnson, G. Pryce, A. White, and C. Whitehouse, Semiconductor Science and Technology **8**, S386 (1993).

[4] M Radosavljevic, T. Ashley, A Andreev, S. Coomber, G Dewey, M. Emeny, M Fearn, D. Hayes, K. Hilton, M. Hudait, et al., in Electron devices meeting, 2008. iedm 2008. ieee international (IEEE, 2008), pp. 1–4.

[5] P. Chang, X. Liu, L. Zeng, K. Wei, and G. Du, in Computational electronics (iwce), 2014 international workshop on (IEEE, 2014), pp. 1–4.

[6] J. A. Del Alamo, Nature **479**, 317 (2011).

[7] P. M. Levine, P. Gong, R. Levicky, and K. L. Shepard, IEEE Journal of Solid-State Circuits **43**, 1859 (2008).

[8] D. Stoppa, D. Mosconi, L. Pancheri, and L. Gonzo, IEEE Sensors Journal **9**, 1084 (2009).

[9] T. Tokuda, M. Takahashi, K. Uejima, K. Masuda, T. Kawamura, Y. Ohta, M. Motoyama, T. Noda, K. Sasagawa, T. Okitsu, et al., Biomedical optics express **5**, 3859 (2014).

[10] D. B. Hernández, R. K. Mishra, R. Muñoz, and J. L. Marty, Sensors and Actuators B: Chemical **246**, 606 (2017).

[11] Y. Chen, R. C. Jaeger, and J. C. Suhling, IEEE Sensors Journal **13**, 2066 (2013).

[12] S. D. Ha, Y. Zhou, C. J. Fisher, S. Ramanathan, and J. P. Treadway, Journal of Applied Physics **113**, 184501 (2013).

[13] S.-J. Han, A. V. Garcia, S. Oida, K. A. Jenkins, and W. Haensch, Nature communications **5**, 3086 (2014).

[14] T. Bagci, A. Simonsen, S. Schmid, L. G. Villanueva, E. Zeuthen, J. Appel, J. M. Taylor, A. S. Sørensen, K. Usami, A. Schliesser, et al., in Frontiers in optics (Optical Society of America, 2014), FW1C–2.

[15] W Liang, D Eliyahu, V. Ilchenko, A. Savchenkov, A. Matsko, D Seidel, and L Maleki, Nature communications **6** (2015).

[16] G. H. Gelinck, H. E. A. Huitema, E. van Veenendaal, E. Cantatore, L. Schrijnemakers, J. B. van der Putten, T. C. Geuns, M. Beenhakkers, J. B. Giesbers, B.-H. Huisman, et al., Nature materials **3**, 106 (2004).

[17] E. Huitema, G. Gelinck, B. van der Putten, E. Cantatore, E. van Veenendaal, L. Schrijnemakers, B.-H. Huisman, and D. de Leeuw, in Solid-state circuits conference, 2003. digest of technical papers. isscc. 2003 ieee international (IEEE, 2003), pp. 380–381.

[18] B. Geffroy, P. Le Roy, and C. Prat, Polymer International **55**, 572 (2006).

[19] J.-S. Park, H. Chae, H. K. Chung, and S. I. Lee, Semiconductor science and technology **26**, 034001 (2011).

[20] V. C. Bender, T. B. Marchesan, and J. M. Alonso, IEEE Industrial Electronics Magazine **9**, 6 (2015).

[21] I. Lee, W. Jung, H. Ha, S. Jeong, Y. Kim, G. Kim, Z. Foo, J.-Y. Sim, D. Sylvester, and D. Blaauw, in Biomedical circuits and systems conference (biocas), 2015 ieee (IEEE, 2015), pp. 1–4.

[22] E. K. Sackmann, A. L. Fulton, and D. J. Beebe, Nature **507**, 181 (2014).

[23] Z. Göröcs and A. Ozcan, IEEE reviews in biomedical engineering **6**, 29 (2013).

[24] K. S. Krishna, Y. Li, S. Li, and C. S. Kumar, Advanced drug delivery reviews **65**, 1470 (2013).

[25] S. Musah, A. Mammoto, T. C. Ferrante, S. S. Jeanty, M. Hirano-Kobayashi, T. Mammoto, K. Roberts, S. Chung, R. Novak, M. Ingram, et al., Nature Biomedical Engineering **1**, s41551 (2017).

[26] C. P. Collier, J. O. Jeppesen, Y. Luo, J. Perkins, E. W. Wong, J. R. Heath, and J. F. Stoddart, Journal of the American Chemical Society **123**, 12632 (2001).

[27] L Britnell, R. Gorbachev, R Jalil, B. Belle, F Schedin, A Mishchenko, T Georgiou, M. Katsnelson, L Eaves, S. Morozov, et al., Science **335**, 947 (2012).

[28] C Grezes, F Ebrahimi, J. Alzate, X Cai, J. Katine, J Langer, B Ocker, P Khalili Amiri, and K. Wang, Applied Physics Letters **108**, 012403 (2016).

[29] S Fusil, V Garcia, A Barthélémy, and M Bibes, Annual Review of Materials Research **44**, 91 (2014).

[30] W. Han, R. K. Kawakami, M. Gmitra, and J. Fabian, Nature nanotechnology **9**, 794 (2014).

[31] A. Chumak, V. Vasyuchka, A. Serga, and B Hillebrands, Nature Physics **11**, 453 (2015).

[32] J. Devkota, R. Geng, R. C. Subedi, and T. D. Nguyen, Advanced Functional Materials **26**, 3881 (2016).

[33] C. Joachim, J. Gimzewski, and A Aviram, Nature **408**, 541 (2000).

[34] J. R. Heath, Annual Review of Materials Research **39**, 1 (2009).

[35] M. Ratner, Nature nanotechnology **8**, 378 (2013).

[36] J. M. van Ruitenbeek, "Molecular electronics: a brief overview of the status of the field," in *Single-molecule electronics* (Springer, 2016), pp. 1–23.

[37] A. K. Feldman, M. L. Steigerwald, X. Guo, and C. Nuckolls, Accounts of chemical research **41**, 1731 (2008).

[38] J. C. Cuevas and E. Scheer, *Molecular electronics: an introduction to theory and experiment*, Vol. 15 (World Scientific, 2017).

[39] A. Barreiro, H. S. van der Zant, and L. M. Vandersypen, Nano letters **12**, 6096 (2012).

[40] H. W. C. Postma, T. Teepen, Z. Yao, M. Grifoni, and C. Dekker, Science **293**, 76 (2001).

[41] S. Kubatkin, A. Danilov, M. Hjort, J. Cornil, J.-L. Bredas, N. Stuhr-Hansen, P. Hedegård, and T. Bjørnholm, Nature **425**, 698 (2003).

[42] M. L. Perrin, E. Burzurí, and H. S. van der Zant, Chemical Society Reviews **44**, 902 (2015).

[43] T. Kim, P. Darancet, J. R. Widawsky, M. Kotiuga, S. Y. Quek, J. B. Neaton, and L. Venkataraman, Nano letters **14**, 794 (2014).

[44] K. Moth-Poulsen and T. Bjørnholm, Nature nanotechnology **4**, 551 (2009).

[45] E. Osorio, T. Bjørnholm, J. Lehn, M Ruben, and H. Van der Zant, Journal of Physics: Condensed Matter **20**, 374121 (2008).

[46] M. Tsutsui and M. Taniguchi, Sensors **12**, 7259 (2012).

[47] L. Venkataraman, J. E. Klare, C. Nuckolls, M. S. Hybertsen, and M. L. Steigerwald, Nature **442**, 904 (2006).

[48] L. Venkataraman, J. E. Klare, I. W. Tam, C. Nuckolls, M. S. Hybertsen, and M. L. Steigerwald, Nano Letters **6**, 458 (2006).

[49] Y. S. Park, A. C. Whalley, M. Kamenetska, M. L. Steigerwald, M. S. Hybertsen, C. Nuckolls, and L. Venkataraman, Journal of the American Chemical Society **129**, 15768 (2007).

[50] D. J. Wold and C. D. Frisbie, Journal of the American Chemical Society **123**, 5549 (2001).

[51] J. M. Beebe, B. Kim, J. Gadzuk, C. D. Frisbie, and J. G. Kushmerick, Physical review letters **97**, 026801 (2006).

[52] M. L. Perrin, C. J. Verzijl, C. A. Martin, A. J. Shaikh, R. Eelkema, J. H. Van Esch, J. M. Van Ruitenbeek, J. M. Thijssen, H. S. Van Der Zant, and D. Dulić, Nature nanotechnology **8**, 282 (2013).

[53] H. Park, A. K. Lim, A. P. Alivisatos, J. Park, and P. L. McEuen, Applied Physics Letters **75**, 301 (1999).

[54] C. Jia, A. Migliore, N. Xin, S. Huang, J. Wang, Q. Yang, S. Wang, H. Chen, D. Wang, B. Feng, et al., Science **352**, 1443 (2016).

[55] X. Guo, J. P. Small, J. E. Klare, Y. Wang, M. S. Purewal, I. W. Tam, B. H. Hong, R. Caldwell, L. Huang, S. O'brien, et al., Science **311**, 356 (2006).

[56] C. S. Lau, H. Sadeghi, G. Rogers, S. Sangtarash, P. Dallas, K. Porfyrakis, J. Warner, C. J. Lambert, G. A. D. Briggs, and J. A. Mol, Nano letters **16**, 170 (2015).

[57] J. Zhu, J. McMorrow, R. Crespo-Otero, G. Ao, M. Zheng, W. P. Gillin, and M. Palma, Journal of the American Chemical Society **138**, 2905 (2016).

[58] E. Lörtscher, Nature nanotechnology **8**, 381 (2013).

[59] F Prins, T Hayashi, B. De Vos van Steenwijk, B Gao, E. Osorio, K Muraki, and H. Van der Zant, Applied Physics Letters **94**, 123108 (2009).

[60] F. Prins, A. Barreiro, J. W. Ruitenberg, J. S. Seldenthuis, N. Aliaga-Alcalde, L. M. Vandersypen, and H. S. van der Zant, Nano letters **11**, 4607 (2011).

[61] Y. Cao, S. Dong, S. Liu, L. He, L. Gan, X. Yu, M. L. Steigerwald, X. Wu, Z. Liu, and X. Guo, Angewandte Chemie International Edition **51**, 12228 (2012).

[62] J. A. Mol, C. S. Lau, W. J. Lewis, H. Sadeghi, C. Roche, A. Cnossen, J. H. Warner, C. J. Lambert, H. L. Anderson, and G. A. D. Briggs, Nanoscale **7**, 13181 (2015).

[63] C. Lau, J. Mol, J. Warner, and G. Briggs, Physical Chemistry Chemical Physics **16**, 20398 (2014).

[64] J. G. Simmons, Journal of applied physics **34**, 1793 (1963).

[65] K. Hagen, *Organic electronics: materials, manufacturing, and applications*, 2006.

[66] C. Wang, H. Dong, W. Hu, Y. Liu, and D. Zhu, Chemical Reviews **112**, 2208 (2011).

[67] M. Berggren, D. Nilsson, and N. D. Robinson, Nature materials **6**, 3 (2007).

[68] Y. Zhong, M. T. Trinh, R. Chen, W. Wang, P. P. Khlyabich, B. Kumar, Q. Xu, C.-Y. Nam, M. Y. Sfeir, C. Black, et al., Journal of the American Chemical Society **136**, 15215 (2014).

[69] Y. Zhong, M. T. Trinh, R. Chen, G. E. Purdum, P. P. Khlyabich, M. Sezen, S. Oh, H. Zhu, B. Fowler, B. Zhang, et al., Nature communications **6**, 8242 (2015).

[70] R. Rotzoll, S. Mohapatra, V. Olariu, R. Wenz, M. Grigas, K. Dimmler, O. Shchekin, and A. Dodabalapur, Applied Physics Letters **88**, 123502 (2006).

[71] S. Steudel, S. De Vusser, K. Myny, M. Lenes, J. Genoe, and P. Heremans, Journal of applied physics **99**, 114519 (2006).

[72] H. Klauk, U. Zschieschang, J. Pflaum, and M. Halik, nature **445**, 745 (2007).

[73] A. N. Sokolov, M. E. Roberts, and Z. Bao, Materials today **12**, 12 (2009).

[74] B Crone, A Dodabalapur, Y. Lin, R. Filas, et al., Nature **403**, 521 (2000).

[75] Y. Zhong, B. Kumar, S. Oh, M. T. Trinh, Y. Wu, K. Elbert, P. Li, X. Zhu, S. Xiao, F. Ng, et al., Journal of the American Chemical Society **136**, 8122 (2014).

[76] C.-Y. Chiu, B. Kim, A. A. Gorodetsky, W. Sattler, S. Wei, A. Sattler, M. Steigerwald, and C. Nuckolls, Chemical Science **2**, 1480 (2011).

[77] A. M. van de Craats, N. Stutzmann, O. Bunk, M. M. Nielsen, M. Watson, K. Müllen, H. D. Chanzy, H. Sirringhaus, and R. H. Friend, Advanced Materials **15**, 495 (2003).

[78] H. Li, B. C. Tee, J. J. Cha, Y. Cui, J. W. Chung, S. Y. Lee, and Z. Bao, Journal of the American Chemical Society **134**, 2760 (2012).

[79] K.-Y. Wu, T.-Y. Wu, S.-T. Chang, C.-S. Hsu, and C.-L. Wang, Advanced Materials **27**, 4371 (2015).

[80] L. Wang, B. Liu, D. Liu, M. Yao, Y. Hou, S. Yu, T. Cui, D. Li, G. Zou, A. Iwasiewicz, et al., Advanced Materials **18**, 1883 (2006).

[81] T. Schiros, G. Kladnik, D. Prezzi, A. Ferretti, G. Olivieri, A. Cossaro, L. Floreano, A. Verdini, C. Schenck, M. Cox, et al., Advanced Energy Materials **3**, 894 (2013).

[82] L. Chen, Y. Jiang, H. Nie, R. Hu, H. S. Kwok, F. Huang, A. Qin, Z. Zhao, and B. Z. Tang, ACS applied materials & interfaces **6**, 17215 (2014).

[83] R. Furue, T. Nishimoto, I. S. Park, J. Lee, and T. Yasuda, Angewandte Chemie International Edition **55**, 7171 (2016).

[84] Q. H. Cui, L. Jiang, C. Zhang, Y. S. Zhao, W. Hu, and J. Yao, Advanced Materials **24**, 2332 (2012).

[85] S. A. Baudron, P. Batail, C. Coulon, R. Clérac, E. Canadell, V. Laukhin, R. Melzi, P. Wzietek, D. Jérome, P. Auban-Senzier, et al., Journal of the American Chemical Society **127**, 11785 (2005).

[86] D.-L. Long, E. Burkholder, and L. Cronin, Chemical Society Reviews **36**, 105 (2007).

[87] S. A. Claridge, A. Castleman Jr, S. N. Khanna, C. B. Murray, A. Sen, and P. S. Weiss, ACS nano **3**, 244 (2009).

[88] X. Roy, C.-H. Lee, A. C. Crowther, C. L. Schenck, T. Besara, R. A. Lalancette, T. Siegrist, P. W. Stephens, L. E. Brus, P. Kim, et al., Science **341**, 157 (2013).

[89] C.-H. Lee, L. Liu, C. Bejger, A. Turkiewicz, T. Goko, C. J. Arguello, B. A. Frandsen, S. C. Cheung, T. Medina, T. J. Munsie, et al., Journal of the American Chemical Society **136**, 16926 (2014).

[90] A. Turkiewicz, D. W. Paley, T. Besara, G. Elbaz, A. Pinkard, T. Siegrist, and X. Roy, Journal of the American Chemical Society **136**, 15873 (2014).

[91] B. Choi, J. Yu, D. W. Paley, M. T. Trinh, M. V. Paley, J. M. Karch, A. C. Crowther, C.-H. Lee, R. A. Lalancette, X. Zhu, et al., Nano letters **16**, 1445 (2016).

[92] D. A. Tomalia and S. N. Khanna, Chemical reviews **116**, 2705 (2016).

[93] W.-L. Ong, E. S. OâĂŹBrien, P. S. Dougherty, D. W. Paley, C. F. Higgs III, A. J. McGaughey, J. A. Malen, and X. Roy, Nature materials **16**, 83 (2017).

[94] A. M. Champsaur, A. Velian, D. W. Paley, B. Choi, X. Roy, M. L. Steigerwald, and C. Nuckolls, Nano letters **16**, 5273 (2016).

[95] L. Sun, Y. A. Diaz-Fernandez, T. A. Gschneidtner, F. Westerlund, S. Lara-Avila, and K. Moth-Poulsen, Chemical Society Reviews **43**, 7378 (2014).

[96] C. Jia, B. Ma, N. Xin, and X. Guo, Accounts of chemical research **48**, 2565 (2015).

[97] C. W. Marquardt, S. Grunder, A. Baszczyk, S. Dehm, F. Hennrich, H. v. Löhneysen, M. Mayor, and R. Krupke, Nature nanotechnology **5**, 863 (2010).

[98] Y. Cao, S. Dong, S. Liu, Z. Liu, and X. Guo, Angewandte Chemie International Edition **52**, 3906 (2013).

[99] X. Wang, L. Gao, B. Liang, X. Li, and X. Guo, Journal of Materials Chemistry B **3**, 5150 (2015).

[100] M. A. Reed, C Zhou, C. Muller, T. Burgin, and J. Tour, Science **278**, 252 (1997).

[101] M. Koole, J. C. Hummelen, and H. S. van der Zant, Physical Review B **94**, 165414 (2016).

[102] M. Koole, J. M. Thijssen, H. Valkenier, J. C. Hummelen, and H. S.v. d. Zant, Nano letters **15**, 5569 (2015).

[103] E. Burzurí, Y. Yamamoto, M. Warnock, X. Zhong, K. Park, A. Cornia, and H. S. van der Zant, Nano letters **14**, 3191 (2014).

[104] H. Wen, W. Li, J. Chen, G. He, L. Li, M. A. Olson, A. C.-H. Sue, J. F. Stoddart, and X. Guo, Science Advances **2**, e1601113 (2016).

[105] P. Qi, A. Javey, M. Rolandi, Q. Wang, E. Yenilmez, and H. Dai, Journal of the American Chemical Society **126**, 11774 (2004).

[106] N. Xin, J. Wang, C. Jia, Z. Liu, X.-S. Zhang, C. Yu, M. Li, S. Wang, Y. Gong, H. Sun, et al., Nano Letters (2017).

[107] X. Guo, A. Whalley, J. E. Klare, L. Huang, S. O'Brien, M. Steigerwald, and C. Nuckolls, Nano letters **7**, 1119 (2007).

[108] X. Guo, A. A. Gorodetsky, J. Hone, J. K. Barton, and C. Nuckolls, Nature nanotechnology **3**, 163 (2008).

[109] C. Thiele, H. Vieker, A. Beyer, B. S. Flavel, F. Hennrich, D. Muñoz Torres, T. R. Eaton, M. Mayor, M. M. Kappes, A. Gölzhäuser, et al., Applied physics letters **104**, 103102 (2014).

[110] P. Puczkarski, P. Gehring, C. S. Lau, J. Liu, A. Ardavan, J. H. Warner, G. A. D. Briggs, and J. A. Mol, Applied Physics Letters **107**, 133105 (2015).

[111] E. Burzurí, F. Prins, and H. S. van der Zant, (2012).

[112] H. Sadeghi, J. A. Mol, C. S. Lau, G. A. D. Briggs, J. Warner, and C. J. Lambert, Proceedings of the National Academy of Sciences **112**, 2658 (2015).

[113] E. Burzurí, J. O. Island, R. Díaz-Torres, A. Fursina, A. González-Campo, O. Roubeau, S. J. Teat, N. Aliaga-Alcalde, E. Ruiz, and H. S. van der Zant, ACS nano **10**, 2521 (2016).

[114] K. Ullmann, P. B. Coto, S. Leitherer, A. Molina-Ontoria, N. Martín, M. Thoss, and H. B. Weber, Nano letters **15**, 3512 (2015).

[115] S Lumetti, A Candini, C Godfrin, F Balestro, W Wernsdorfer, S Klyatskaya, M Ruben, and M Affronte, Dalton Transactions **45**, 16570 (2016).

[116] A. Barreiro, F Borrnert, M. Rummeli, B Buchner, and L. M. Vandersypen, Nano letters **12**, 1873 (2012).

[117] P. Gehring, H. Sadeghi, S. Sangtarash, C. S. Lau, J. Liu, A. Ardavan, J. H. Warner, C. J. Lambert, G. A. D. Briggs, and J. A. Mol, Nano letters **16**, 4210 (2016).

[118] J. O. Island, A. Holovchenko, M. Koole, P. F. A. Alkemade, M. Menelaou, N. Aliaga-Alcalde, E. Burzurí, and H. S. J. van der Zant, Journal of Physics: Condensed Matter **26**, 474205 (2014).

[119] D. Bischoff, P. Simonet, A. Varlet, H. C. Overweg, M. Eich, T. Ihn, and K. Ensslin, physica status solidi (RRL)-Rapid Research Letters **10**, 68 (2016).

[120] S Agrawal, M. Raghuveer, R Kröger, and G Ramanath, Journal of applied physics **100**, 094314 (2006).

[121] D. Bouilly, J. Hon, N. S. Daly, S. Trocchia, S. Vernick, J. Yu, S. Warren, Y. Wu, R. L. Gonzalez Jr, K. L. Shepard, et al., Nano letters **16**, 4679 (2016).

[122] G. T. Hermanson, *Bioconjugate techniques* (Academic press, 2013).

[123] J. Ulrich, D. Esrail, W. Pontius, L. Venkataraman, D. Millar, and L. H. Doerrer, The Journal of Physical Chemistry B **110**, 2462 (2006).

[124] M. S. Hybertsen, L. Venkataraman, J. E. Klare, A. C. Whalley, M. L. Steigerwald, and C. Nuckolls, Journal of Physics: Condensed Matter **20**, 374115 (2008).

[125] W. Ding, M. Koepf, C. Koenigsmann, A. Batra, L. Venkataraman, C. F. Negre, G. W. Brudvig, R. H. Crabtree, C. A. Schmuttenmaer, and V. S. Batista, Journal of chemical theory and computation **11**, 5888 (2015).

[126] C. Koenigsmann, W. Ding, M. Koepf, A. Batra, L. Venkataraman, C. F. Negre, G. W. Brudvig, R. H. Crabtree, V. S. Batista, and C. A. Schmuttenmaer, New Journal of Chemistry **40**, 7373 (2016).

[127] K. Kaasbjerg and K. Flensberg, Nano letters **8**, 3809 (2008).

[128] E. A. Osorio, K. O'Neill, N. Stuhr-Hansen, O. F. Nielsen, T. Bjørnholm, and H. S. van der Zant, Advanced Materials **19**, 281 (2007).

[129] L. C. Venema, J. W. Wildöer, J. W. Janssen, S. J. Tans, H. L. T. Tuinstra, L. P. Kouwenhoven, and C. Dekker, Science **283**, 52 (1999).

[130] M. Buitelaar, A Bachtold, T Nussbaumer, M Iqbal, and C Schönenberger, Physical Review Letters **88**, 156801 (2002).

[131] P. Facci, V. Erokhin, S. Carrara, and C. Nicolini, Proceedings of the National Academy of Sciences **93**, 10556 (1996).

[132] A. D. Bochevarov, E. Harder, T. F. Hughes, J. R. Greenwood, D. A. Braden, D. M. Philipp, D. Rinaldo, M. D. Halls, J. Zhang, and R. A. Friesner, International Journal of Quantum Chemistry **113**, 2110 (2013).

[133] X. Duan, Y. Huang, Y. Cui, J. Wang, and C. M. Lieber, Nature **409**, 66 (2001).

[134] B. Tian, X. Zheng, T. J. Kempa, Y. Fang, N. Yu, G. Yu, J. Huang, and C. M. Lieber, nature **449**, 885 (2007).

[135] L. E. Greene, M. Law, B. D. Yuhas, and P. Yang, The Journal of Physical Chemistry C **111**, 18451 (2007).

[136] Q. Li, S. Ding, W. Zhu, L. Feng, H. Dong, and W. Hu, Journal of Materials Chemistry C **4**, 9388 (2016).

[137] S.-L. Li, T. Xiao, C. Lin, and L. Wang, Chemical Society Reviews **41**, 5950 (2012).

[138] Y. Zhang, H. Dong, Q. Tang, S. Ferdous, F. Liu, S. C. Mannsfeld, W. Hu, and A. L. Briseno, Journal of the American Chemical Society **132**, 11580 (2010).

[139] C. Fan, A. P. Zoombelt, H. Jiang, W. Fu, J. Wu, W. Yuan, Y. Wang, H. Li, H. Chen, and Z. Bao, Advanced Materials **25**, 5762 (2013).

[140] H. Wang, F. Zhu, J. Yang, Y. Geng, and D. Yan, Advanced Materials **19**, 2168 (2007).

[141] W. Chen, H. Huang, S. Chen, X. Y. Gao, and A. T. S. Wee, The Journal of Physical Chemistry C **112**, 5036 (2008).

[142] W. Chen, H. Huang, S. Chen, Y. L. Huang, X. Y. Gao, and A. T. S. Wee, Chemistry of Materials **20**, 7017 (2008).

[143] A. A. Gorodetsky, C.-Y. Chiu, T. Schiros, M. Palma, M. Cox, Z. Jia, W. Sattler, I. Kymissis, M. Steigerwald, and C. Nuckolls, Angewandte Chemie International Edition **49**, 7909 (2010).

[144] A. Masuhara, Z. Tan, H. Kasai, H. Nakanishi, and H. Oikawa, Japanese Journal of Applied Physics **48**, 050206 (2009).

[145] L. Wang, B. Liu, S. Yu, M. Yao, D. Liu, Y. Hou, T. Cui, G. Zou, B. Sundqvist, H. You, et al., Chemistry of materials **18**, 4190 (2006).

[146] X. Zhang and X.-D. Li, Chinese Chemical Letters **25**, 501 (2014).

[147] M. Tanaka, Bulletin of the Chemical Society of Japan **50**, 2881 (1977).

[148] R. Gross-Lannert, W. Kaim, and B. Olbrich-Deussner, Inorganic chemistry **29**, 5046 (1990).

[149] J. S. Miller, A. J. Epstein, and W. M. Reiff, Chemical Reviews **88**, 201 (1988).

[150] J. S. Miller, D. T. Glatzhofer, D. M. O'Hare, W. M. Reiff, A. Chakraborty, and A. J. Epstein, Inorganic Chemistry **28**, 2930 (1989).

[151] S. Mikami, K.-i. Sugiura, T. Maruta, Y. Maeda, M. Ohba, N. Usuki, H. Ōkawa, T. Akutagawa, S. Nisihara, T. Nakamura, et al., Journal of the Chemical Society, Dalton Transactions, 448 (2001).

[152] R. J. Gale, *Spectroelectrochemistry: theory and practice* (Springer Science & Business Media, 2012).